Study of heavy-ion reactions with large solid angle magnetic spectrometers

Mijatović, Tea

University of Zagreb

FACULTY OD SCIENCE

Tea Mijatović

Study of heavy-ion reactions with large solid angle magnetic spectrometers

DOCTORAL DISSERTATION

Zagreb, 2015.

University of Zagreb

FACULTY OF SCIENCE

Tea Mijatović

Study of heavy-ion reactions with large solid angle magnetic spectrometers

DOCTORAL DISSERTATION

Supervisor: Dr. sc. Suzana Szilner

Zagreb, 2015

Sveučilište u Zagrebu

PRIRODOSLOVNO-MATEMATIČKI FAKULTET

Tea Mijatović

Proučavanje teškoionskih reakcija magnetskim spektrometrom velikoga prostornoga kuta

DOKTORSKI RAD

Mentor: Dr. sc. Suzana Szilner

Zagreb, 2015.

University of Zagreb
Faculty of Science
Department of Physics

Doctoral Thesis

Study of heavy-ion reactions with large solid angle magnetic spectrometers

Tea Mijatović
Ruđer Bošković Institute, Zagreb

Nucleon transfer reactions at energies close to the Coulomb barrier always played an important role in nuclear structure and reaction dynamics studies. It has been shown that heavy-ion reactions are an ideal tool for the study of the residual interaction in nuclei, in particular the components responsible for the couplings and correlations.

The main subject of the present thesis is the study of the properties of the nuclear force which are not accounted for by the mean field description, especially the role played by neutron-proton correlations. This has been addressed by measurements of multinucleon transfer reactions performed with the new generation magnetic spectrometer PRISMA and its ancillary detectors. The experimental differential and total cross sections and total kinetic energy loss distributions for the final reaction products have been extracted and compared with the predictions of the GRAZING model for heavy-ion transfer reactions, based on semi-classical theory.

The main objective was to search for an experimental signature of transfer of correlated neutron-proton pairs in the region near the $Z = 20$ and $N = 20$ shell closures. Through the simultaneous study of the absolute cross sections for all channels populated via transfer of nucleon pairs $(\pm nn)$, $(\pm pp)$ and $(\pm np)$, and their comparison with the theoretical predictions, we explored the possible effect of (np) correlation. The findings have been also corroborated with results obtained at energies below the Coulomb barrier, where the excitation energies of the final reaction products are expected to be small.

The comparison of the experimental results with the semi-classical calculations that include only the transfer of independent particles shows that the experimental cross section of $(+1p+1n)$ channel is enhanced, indicating the possibility of a presence of a (np) pair degree of freedom. The analysis of these inclusive data was corroborated by a complementary analysis of γ-particle coincidences, where PRISMA has been used in coupled

operation with the CLARA γ array. From the analysis of these coincidences, the population strength of excited states has been extracted for different transfer channels. In particular, for ^{42}K, reached via the $(+1p+1n)$ channel, a strong population of the 7^+ state has been evidenced. Since this can happen when a neutron and a proton occupy the same $f_{7/2}$ orbital, the finding may give a further support to the presence of a neutron-proton correlation.

(160 pages, 109 references, 97 figures, 12 tables, original in English)

Keywords: multinucleon transfer reactions, magnetic spectrometers, nucleon-nucleon correlations, differential and total cross sections

Supervisor: Dr. sc. Suzana Szilner, Ruđer Bošković Institute, Zagreb

Reviewers:
1. Assoc. prof. dr. sc. Matko Milin, University of Zagreb
2. Dr. sc. Lorenzo Corradi, Laboratori Nazionali di Lengaro, Lengaro, Italy
3. Assoc. prof. dr. sc. Tamara Nikšić, University of Zagreb
4. Dr. sc. Suzana Szilner, Ruđer Bošković Institute, Zagreb
5. Prof. dr. sc. Dario Vretenar, F.C.A., University of Zagreb

Thesis accepted: 2015

Sveučilište u Zagrebu
Prirodoslovno-matematički fakultet
Fizički odsjek

Doktorski rad

Proučavanje teškoionskih reakcija magnetskim spektrometrom velikoga prostornoga kuta

Tea Mijatović
Institut Ruđer Bošković, Zagreb

Reakcije prijenosa nukleona na energijama blizu kulonske barijere važne su i u proučvanju strukture jezgara i mehanizma reakcije. Pokazalo se da su teškoionske reakcije odličan način proučavanja rezidualne interakcije u jezgrama, naročito dijelova odgovornih za vezanje i korelacije.

Glavna tema ovog doktorskog rada je proučavanje svojstava nuklearne sile koja nisu uključena u opis pomoću srednjeg polja, posebno uloga korelacija između neutrona i protona. To se proučavalo mjerenjem reakcije prijenosa mnogo nukleona s magnetskim spektrometrom velikoga prostornoga kuta PRISMA i njegovim pomoćnim detektorima. Dobiveni su diferencijalni i ukupni udarni presjek, raspodjela gubitka kinetičke energije za sve produkte reakcije, te su uspoređeni s teorijskim predviđanjima modela GRAZING.

Glavna ideja je potraga za eksperimentalnim potpisom prijenosa koreliranog para neutron-proton u području blizu $Z = 20$ i $N = 20$ zatvorenih ljusaka. Istodobnom usporedbom apsolutnog udarnog presjeka za sve kanale koje su pobuđeni prijenosom para nukleona, $(\pm nn)$, $(\pm pp)$ i $(\pm np)$, te njihovom usporedbom s teorijskim predviđanjima, traženi su mogući efekti (np) korelacija. Rezultati su potvrđeni s rezultatima dobivenim na energijama ispod kulonske barijere, gdje se očekuju male energije pobuđenja produkata reakcije.

Usporedba mjerenih rezultata s polu-klasičnim računima koji uključuju samo prijenos neovisnih čestica pokazuje da je $(+1p+1n)$ kanal pojačan, što može ukazivati na moguć doprinos (np) korelacija. Analiza inkluzivnih podataka je nadopunjena dodatnom analizom γ-fragment koincidencija, kada je PRISMA korištena s CLARA γ detektorom. Ove koincidencije omogućuju proučavanje snage pobuđenja različitih stanja. ^{42}K kanal, pobuđen putem prijenosa jednog protona i neutrona, pokazuje jako pobuđenje 7^+ stanja.

Taj rezultat se može shvatiti kao dodatna potvrda prisutnosti korelacije neutron-proton, jer se 7^+ stanje može opisati kao stanje u kojem su neutron i proton u istoj $f_{7/2}$ orbitali.

(160 stranica, 109 literaturnih navoda, 97 slika, 12 tablica, izvornik na engleskom jeziku)

Ključne riječi: reakcije prijenosa mnogo nukleona, nukleon-nukleon korelacije, kutna raspodjela, ukupni udarni presjek

Mentor: Dr. sc. Suzana Szilner, Ruđer Bošković Institute, Zagreb

Povjerenstvo za obranu:
1. Izv. prof. dr. sc. Matko Milin, Sveučilište u Zagrebu
2. Dr. sc. Lorenzo Corradi, Laboratori Nazionali di Lengaro, Lengaro, Italija
3. Izv. prof. dr. sc. Tamara Nikšić, Sveučilište u Zagrebu
4. Dr. sc. Suzana Szilner, Institut Ruđer Bošković, Zagreb
5. Akademik Dario Vretenar, Sveučilište u Zagrebu

Rad prihvaćen: 2015

I would like to thank my advisor dr. sc. Suzana Szilner for the support, guidance and all the opportunities that I had during my doctorate. I would also like to thank dr. sc. Matko Milin for his help, advice and for answering my every question, and members of Laboratory of nuclear physics, Ruđer Bošković Institute for providing warm and stimulating work environment.

Furthermore, I would like to thank everyone included in the PRISMA collaboration (dr. L. Corradi, dr. G. Montagnoli, dr. A. Stefanini, dr. E. Fioretto...) for making this work possible, and particularly Daniele and Alain for the help and fun during long night shifts. PRISMA team's work was instrumental to the completion of my thesis. Also, I would like to thank Caterina and Enrico for making my first days in Legnaro pleasant and enjoyable. Finally, I would like to thank all my friends for their encouragement and understanding and specially my family, my sister Mia and Lovro, for everything, for their presence, love and support.

Prošireni sažetak

Nuklearne reakcije prijenosa na energijama bliskim kulonskoj barijeri oduvijek su važne u proučavanju nuklearne strukture i dinamike reakcija. Pokazano je da su teškoionske reakcije odličan način za proučavanje rezidualne interakcije u jezgrama, posebno za proučavanje komponenata odgovornih za vezanje i korelacije. Glavna tema ovog doktorskog rada je istraživanje svojstava nuklearne sile koja nisu uključena u opis pomoću srednjeg polja, posebno uloga korelacija neutron-proton. To će se proučavati mjerenjima reakcija prijenosa mnogo nukleona na magnetskom spektrometru nove generacije PRISMA i vezanim detektorima.

Teškoionske reakcije i korelacije

Nuklearne reakcije inducirane različitim probama jedan su od osnovnih alata za proučavanje atomske jezgre od njenog otkrića do danas. Većina dosadašnjeg znanja rezultat je proučavanja reakcija i strukture jezgara blizu doline stabilnosti. Zadnjih desetljeća, zbog razvoja novih instrumenata i radioaktivnih snopova, interes se proširio prema neutronski i protonski bogatim jezgrama.

U sudaru teških iona jezgre mogu izmijeniti nekoliko kvanata energije i momenta impulsa ili mase i naboja, ili mogu proizvesti složenu jezgru u procesu fuzije. Na energijama bliskim kulonskoj barijeri reakcije prijenosa čine velik dio ukupnog udarnog presjeka reakcije, te upravo zbog toga imaju veliku ulogu u istraživanjima strukture jezgara. Reakcije prijenosa izazvane lakim ionima su dale važne podatke za konstrukciju modela ljusaka i shvaćanje svojstava korelacija među nukleonima u nuklearnom mediju. Prijenos više nukleona je moguć u reakcijama s teškim jezgrama što daje mogućnost proučavanja relativne uloge prijenosa jedne čestice ili para. Prijenosom više nukleona dobije se i mogućnost istraživanja mehanizma reakcije, pogotovo prijelaz prema duboko neelastičnim sudarima.

U teškoionskim mjerenjima blizu kulonske barijere mogu se identificirati produkti reakcije gdje je projektil izgubio samo umjerenu količinu energije i razmijenio samo nekoliko nukleona s metom. Takve reakcije se nazivaju kvazielastične. Karakterizira ih kutna raspodjela koja obično ima dobro definiran vrh na kutu okrznuća. Pobuđuju dobro definirana stanja, koja su obično niskoležeća u energiji s relativno visokim spinovima. Ovisno o

broju prenešenih nukleona i gubitku energije u odnosu na ulazni kanal, ove reakcije postepeno prelaze u duboko neelastične sudare u kojima dolazi do velikog gubitka energija, uz zadržavanje informacije o ulaznom kanalu. Karakterizira ih kutna raspodjela koja raste prema prednjim kutevima.

Kao što je već spomenuto, prijenosi parova u reakcijama prijenosa mnogo nukleona (MNT) omogućuju istraživanje korelacija među nukleonima. Prijenos para nukleona se može dogoditi na dva načina: sekvencijalno gdje se nukleoni prenose jedan po jedan, ili simultano gdje se prenose u jednom koraku, kao par. Do sada je u teškoionskim reakcijama pokazano da sekvencijalni prijenos dominira, iako su u oba procesa važne korelacije.

Mogući efekti korelacija neutron-neutron (nn) i proton-proton (pp) već su raspravljani u revijalnom članku [1] i tamo navedenim referencama. Dva su moguća načina istraživanja korelacija putem reakcija prijenosa, te su prikazana u ovom radu. Prvi način je mjerenje kutne raspodjele na fiksnoj energiji projektila, blizu kulonske barijere, a drugi je mjerenje funkcije pobuđenja na fiksnim kutevima, do duboko ispod barijere.

Prvim načinom je pokazano da vjerojatnost za pobiranje neutrona opada u jednakim koracima za svaki prenešeni neutron, kao što se i očekuje kod prijenosa neovisnih čestica. Udarni presjek za protone se ponaša drugačije i udarni presjek ($-2p$) kanala je gotovo jednak udarnom presjeku ($-1p$). To naznačuje doprinos procesa koji uključuju prijenos koreliranog para protona, a ne samo uzastopan prijenos jednog po jednog protona. Ova asimetrija u ponašanju protona i neutrona, koja je uočena u svim do sad proučavanim reakcijama, javlja se zbog udarnog presjeka koji je gotovo red veličine veći za kanal prijenosa neutrona u odnosu na kanale prijenosa protona, pa je tako doprinos prijenosa para neutrona prikriven.

Drugi način je primjenjen na jezgrama zatvorenih ili poluzatvorenih ljusaka ^{96}Zr+^{40}Ca i supervodljivom sustavu ^{116}Sn+^{60}Ni gdje je glavni cilj bilo proučavanje korelacije među neutronima. Mjerena je ukupna funkcija pobuđenja od energije kulonske barijere do oko 25% ispod nje. Korištenje inverzne kinematike i detektiranje iona na prednjim kutevima osigurava dostatnu kinetičku energiju lakšem partneru što je bitno za masenu razlučivost, dok fokusiranost u prednje kuteve u laboratorijskom sustavu rezultira većom efikasnošću. Na enerijama ispod kulonske barijere proizvedene jezgre imaju malu energiju pobuđenja, svega nekoliko MeV-a, što bitno umanjuje složenost računa vezanih kanala i olakšava kvantitativno određivanje efekta korelacija nukleon-nukleon. Mikroskopska

teorija, koja uključuje korelacije nukleon-nukleon, je po prvi put dobro opisala vjerojatnost prijenosa dva nukleona, i u obliku funkcije pobuđenja i u apsolutnoj veličini, u teškoionskom ^{116}Sn+^{60}Ni sustavu.

Također je važno proučavanje uloge korelacija neutron-proton (np). Nuklearni modeli ukazuju da bi takve korelacije trebale biti najjače za $N \sim Z$ jezgre gdje protoni i neutroni popunjavaju iste orbitale. Isprobano je nekoliko tehnika za proučavanje (np) korelacija: mjerenja energija vezanja i usporedba s teorijom, gama spektroskopija, reakcije izbijanja (np) para. Dodavanje ili uklanjanje para nukleona iz parno-parne jezgre putem reakcija prijenosa trebala bi biti važna dodatna metoda. Kako je raspodjela udarnog presjeka po različitim izlaznim kanalima određena optimalnom Q-vrijednosti upotrebom stabilnih snopova najjače se pobuđuju kanali pobiranja neutrona i ogoljavanja protona. Kako bi se proučila (np) korelacija potrebno je pažljivo izabrati sistem gdje mehanizam reakcije omogućuje pobuđenje i kanala pobiranja i ogoljavanja i protona i neutrona. Razlog leži u tome što je interpretacija $(-1p-1n)$ kanala uglavnom kompliciran zbog sudjelovanja sekundarnih procesa, poput evaporacije neutrona, dok bi $(+1p+1n)$ kanal trebao biti pobuđen direktnim mehanizmom i efekti evaporacije bi trebali biti manji.

Usporedba eksperimentalnih udarnih presjeka za $(+1p+1n)$ kanal s onima individualnih, $(+1n)$ i $(+1p)$, kanala trebala bi dati informaciju o (np) korelacijama. Dodatna usporedba ($\pm nn$), ($\pm pp$) i ($\pm np$) kanala s teorijskim modelima je važna kako bi se vidjelo koji su stupnjevi slobode bitni u opisu mjerenih diferencijalnih i ukupnih udarnih presjeka, te utjecaj korelacija. U tu svrhu napravljena su dva mjerenja: mjerenje diferencijalnih i ukupnih udarnih presjeka, te raspodjele energija u ^{40}Ar+^{208}Pb s PRISMA-CLARA postavom iznad kulonske barijere, te mjerenje funkcije pobuđenja u ^{92}Mo+^{54}Fe do $\sim$20% ispod barijere.

Eksperimentalni postav

Magnetski spektrometar je idealan za mjerenja reakcija prijenosa jer je moguće u isto vrijeme odrediti masu i naboj, diferencijalni i ukupni udarni presjek, te raspodjelu ukupnog gubitka kinetičke energije različitih izlaznih kanala, a kada je vezan s gama detektorima i koincidentne elektromagnetske prijelaze za svaki proizvedeni izotop. PRISMA je magnetski spektrometar velikog prostornog kuta nove generacije koji radi na principu rekonstrukcije putanja iona unutar magnetskih elemenata. Optički elementi PRISME su dipol

i kvadrupol, a korekcija optičkih aberacija dobiva se upravo rekonstrukcijom putanja događaj po događaj na osnovi mjerenja položaja na ulazu i izlazu iz spektrometra, te vremena proleta. Detektorski sustav se sastoji se od ulaznog detektora, ploče s mikrokanalićima velike površine (MCP) te detektora u fokalnoj ravnini, višežičanog lavinskog brojača s paralelnim pločama (MWPPAC) i ionizacijske komore (IC). MCP i MWPPAC detektor daju informacije u položaju na ulazu i fokalnoj ravnini, u X i Y smjeru, te služe i za mjerenja vremena proleta. IC detektorom se mjeri gubitak energije i ukupna kinetička energija. Glavna karakteristika ovog spektrometra je upravo veliki prostorni kut od 80 msr, te velika prihvatljivost momenta $\pm 10\%$. Raspon masa za koji PRISMA najbolje funkcionira je između $A = 20 - 200$ što je u skladu sa snopovima i energijama karakterističnim za Tandem akceleratorski sustav laboratorija u Legnaru.

Detektor je radio u koincidenciji s CLARA sustavom germanijskih detektora velike čistoće koji je bio postavljen blizu mete, te nasuprot PRISME. Sustav se sastoji od 25 četverodijelnih detektora, od kojih je svaki smješten u štit od Comptonovog zračenja. Karakterizira ga odlična energijska razlučivost (0.6% za $E_\gamma = 1.33$ MeV) i efikasnost fotovrha (3% za $E_\gamma = 1.33$ MeV). Koincidencija PRISMA i CLARA omogućuje da se svakom produktu reakcije pridruži odgovarajući γ spektar.

Eksperiment i analiza mjerenja

U mjerenju diferencijalnog i ukupnog udarnog presjeka u ^{40}Ar+^{208}Pb reakciji korišten je snop ^{40}Ar energije 260 MeV, što je otprilike 30% iznad kulonske barijere. Lakši fragmenti su identificirani u PRISMI koja je bila smještena na tri različita kuta, pokrivši više od 20 stupnjeva kutne raspodjele. Osim diferencijalnog i ukupnog udarnog presjeka, mjerena je i raspodjela gubitka kinetičke energije.

Prvi korak u analizi je kalibracija svih detektora, kako bi se dobile fizikalne veličine. Identifikacija svih događaja se dobiva rekonstrukcijom putanja, koja koristi jednadžbe gibanja iona u magnetskim elementima i mjerene parametre (ulazni i položaji na fokalnoj ravnini, vrijeme proleta, gubitak energije i ukupna kinetička energija). Parametri koji su povezani sa spektrometrom, kut na koji je spektrometar položen i magnetska polja, su poznati i namješteni prije početka analize. U prvoj aproksimaciji se pretpostavi da su putanje planarne u PRISMA ravnini i da su magnetski elementi idealni. Gibanje iona unutar kvadrupola je hiperbolično defokusirajuće u horizontalnoj ravnini, te sinusoidalno

fokusirajuće u vertikalnoj ravnini. Nakon toga ioni ulaze u dipol, gdje zbog Lorentzove sile putanje prate kružno gibanje. Nakon dipola pretpostavlja se da putanje prate ravne linije. Rezultati rekonstrukcije putanja su polumjer zakrivljenosti unutar dipola, ukupna duljina puta, ukupna energija oslobođena u ionizacijskoj komori putem vremena proleta, te domet iona u ionizacijskoj komori.

Nuklearni naboj Z se dobiva mjerenjem gubitka energije, ili dometa iona u ionizacijskog komori, i ukupne energije u ionizacijskoj komori smještenoj u fokalnoj ravnini. Najintenzivnija raspodjela događaja pripada izotopima argona, od kojih je najprisutniji ^{40}Ar koji je elastično i neelastično raspršen, a ostale linije se mogu identificirati uz pomoć Bethe-Bloch formule. Nakon toga se za svaki pojedini element trebaju identificirati nabojna stanja, što se radi uz pomoć $\rho\beta$ - E matrice (taj izbor proizlazi iz izraza $E \sim qB\rho v$) gdje najintenzivnija raspodjela odgovara najvjerojatnijem nabojnom stanju izračunatom pomoću formule 3.12. Nakon toga, maseni brojevi se dobiju množenjem A/q vrijednosti s identificiranim q ($A = qB\rho/v$). Identificirani su prijelazi od $(+4p)$ do $(-5p)$, te su prikazani na slici 3.13.

Analiza CLARA podataka počinje s kalibracijom svih energijskih spektara za što se koristi ^{152}Eu radioaktivni izvor. Uz pomoć ^{152}Eu izvora određena je i efikasnost CLARA detektora. Koristi se tanka meta, te su γ zrake emitirane u letu, zbog čega je potrebna Doppler korekcija koja se radi na osnovi mjerenja brzine PRISMA spektrometrom. Ako se pretpostavi binarna reakcija, može se odrediti i brzina i smjer teškog partnera te se može napraviti i Doppler korekcija njegovog γ spektra.

Funkcija odziva spektrometra

Shvaćanje mehanizma reakcija jako ovisi o određivanju apsolutnog udarnog presjeka te je u tu svrhu potrebno precizno odrediti karakterističnu funkciju odziva spektrometra. Pronalaženje te funkcije zasniva se na simulaciji putanje iona, uzimajući u obzir kinematiku reakcije, geometriju magnetskih elemenata i detektora. Kako se rekonstrukcija putanja oslanja na preciznom određivanju magnetskih i rubnih polja, namještanje magnetskih polja, koje se radi kako bi simulacija u potpunosti odgovarala mjerenju, je ključna točka u proučavanju funkcije odziva. U tu svrhu se koristi pretpostavka da za iste fizikalne uvjete otklon nabojnih stanja mora biti isti u mjerenju i simulaciji. Procedura se radi korak po korak, prvo za dipol za koji se uzimaju putanje duž optičke osi spektrometra, a

zatim se gleda kvadrupol. Nakon toga se stvara velik broj događaja koje slijede uniformnu raspodjelu u energiji i izotropnu u kutevima, te se prenose kroz spektrometar. Funkcija odziva se tada može definirati kao omjer izlazne, odnosno raspodjele na fokalnoj ravnini, i ulazne raspodjele događaja. Pokazalo se da odziv spektrometra ovisi na složen način o ulaznim kutevima i impulsu iona. Tako dobivena funkcija odziva spektrometra koristi se za korekciju diferencijalnog i ukupnog udarnog presjeka zasebno za svaki reakcijski kanal. Glavna korekcija za sve kanale koji su proučavani je, kao što se i očekivalo, na rubu kutnog prihvata s velikim razlikama u apsolutnim vrijednostima koje ovise o izlaznom ionu i kinetičkoj energiji.

Funkcija odziva, prije nego što se primijeni na mjerenja, je testirana ulaznom raspodjelom izračunatom poluklasičnim modelom GRAZING. Kao što je pokazano [1] ovaj model dobro reproducira, u apsolutnim vrijednostima, oblik kutne raspodjele jednonukleonskih kanala $(+1n)$ i $(-1p)$. Izvrsno slaganje između izvornih ulaznih raspodjela i korigiranih raspodjela događaja pokazuje valjanost tako izračunate funkcije odziva.

Eksperimentalni rezultati

Mjerena reakcija ^{40}Ar+^{208}Pb pokazuje vrlo simetričnu raspodjelu oko ^{40}Ar, pobuđeni su i kanali pobiranja i ogoljavanja i protona i neutrona. Prvo je za te kanale pogledana raspodjela gubitka kinetičke energije (TKEL) koja direktno predstavlja energije pobuđenja dvije jezgre. Može se primjetiti da TKEL raspodjela za neutronske prijenose ima najveći doprinos blizu optimalne Q-vrijednosti. Što se prenosi više nukleona, posebno protona, raspodjela se sve više odmiče od te vrijednosti prema većim gubitcima energije.

Mogu se definirati dvije vrste događaja, jedan s izraženim vrhom na maloj TKEL, koji će biti označen kao kvazielastično raspršenje (QE). Drugi karakterizira veliki gubitak energije, vidi se formiranje dugog repa u distribuciji, te će biti označen kao duboko neelastično raspršenje (DIC). QE se dobro vidi u kanalima za prijenos neutrona. Duboko neelastični sudari, koje karakterizira veliki prijenos energije, se obično prepoznaju po širokim kutnim raspodjelama. Čak i ako postoji razlika u vrijednostima gubitka energije za ova dva slučaja, teško ih je razdvojiti, jer je njihovo preklapanje prilično veliko. Međutim, očekuje se da će doprinos DIC biti sve veći na prednjim kutevima. Osim toga, veliki gubitak energije postaje izraženiji kako se više čestica prenosi.

Dvije komponente prisutne u TKEL spektru su odijeljene za svaki kut u TKEL-masa

matrici. Dio s nižim vrijednostima TKEL, do ∼20 MeV, je označen kao QE, a dio iznad kao DIC. U ovom odjeljivanju uzete su u obzir Q-vrijednosti osnovnog stanja.

Vezanje magnetskog spektrometra PRISMA s gama detektorom CLARA iskorišteno je za dobivanje udarnog presjeka za elastični kanal. Na prednjim kutevima elastično raspršenje je dobro aproksimirano Rutherfordovim udarnim presjekom, te se tako dobiva apsolutni faktor normalizacije (u mb/sr) za sve ostale kanale reakcije. Faktor normalizacije se dobije za svaku od kutnih postavki PRISME zasebno. Vrijednost tog faktora normalizacije odražava i trajanje mjerenja na svakoj od postavki spektrometra.

Opisana procedura određivanja funkcije odziva omogućuje spajanje kutnih raspodjela mjerenih različitim postavkama PRISME u jedinstvenu kutnu raspodjelu, a primijenjena je na svaki eksperimentalni diferencijalni udarni presjek odvojeno. Ova procedura primjenjena je po prvi puta za magnetski spektrometar velikog prostornog kuta. Diferencijalni i ukupni udarni presjeci za svaki kanal prijenosa prikazani su u Poglavlju 5. Eksperimentalni diferencijalni udarni presjeci korigirani za funkciju odziva PRISMA spektrometra za $(+1n)$ i $(-1p)$ kanale pokazuju oblik gaussijana u uskom rasponu kuteva s maksimumom blizu kuta raspršenja. Svi jednonukleonski kanali pokazuju takvu kutnu raspodjelu tipičnu za kvazielastični proces. Kako se prenosi više protona raspodjela postaje sve ravnija i počinje gubiti QE svojstva. Uz povećanje prijenosa protona distribucija postaje šira na prednjim kutovima, što je pogotovo vidljivo za pobiranje protona. Zato su i napravljene kutne raspodjele za QE i DIC dio. QE kutne raspodjele imaju oblik gaussijana s maksimum na kutu okrznuća kao što se i očekuje, dok je DIC raspodjela puno ravnija i raste prema prednjim kutevima.

Ukupni udarni presjeci su dobiveni integracijom kutnih raspodjela, a integrirani su i preko ukupnog TKEL raspona i preko QE dijela. Pobiranje neutrona slijedi trend uočen u prijašnjim mjerenjima, gdje ukupni udarni presjek konstantno pada sa svakim prenesenim neutronom. S druge strane ogoljavanje protona ne slijedi taj trend, i $(-2p)$ kanal je po jakosti sličan $(-1p)$ kanalu.

Vezanje magnetskog spektrometra PRISMA i gama detektora CLARA

Kako bi proučili individualna pobuđena stanja, elektromagnetski prijelazi za svaki detektirani izotop u PRISMI izmjereni su gama detektorima CLARA. Ta mjerenja pružaju

komplementarne podatke relevante za korelacije, jer informacije o korelacijama mogu biti skrivene u inkluzivnom karakteru udarnih presjeka. Reakcije ovog tipa, kvazielastične, favoriziraju određenu selektivnost u pobuđenim stanjima, odnosno pobuđuju se stanja na određenim energijama pobuđenja, momentima impulsa ili stanja određene strukture. Kratkodosežna interakcija sparivanja razdjeljuje jakost prijenosa oko različitih konačnih stanja, te γ spektar može dati važne dodatne informacije.

Rezultati koji govore o strukturi izotopskih lanaca argona i klora su publicirani u referencama [2] i [3]. U ovom radu ćemo se koncentrirati na izotope kalija. Spektar ^{42}K pokazuje jaku pobuđenost niskoležećih stanja negativnih pariteta, koji se mogu gledati kao multiplet nastao vezanjem nesparenog protona u $d_{3/2}$ i nesparenog neutrona u $f_{7/2}$. Osim toga vide se jaka stanja pozitivnog pariteta na višim energijama. Njih se može opisati pobuđenjem protona u $f_{7/2}$ orbitalu i njegovo vezanje s nesparenim neutronom u istoj orbitali. Spektar pokazuje dobro slaganje s modelom slabog vezanja (engl. weak-coupling model). Posebno je jako pobuđeno stanje 7^+. To isto stanje je bilo daleko najjače pobuđeno stanje u reakciji prijenosa deuterona u ^{4}He+^{40}Ar sustavu.

Rasprava

Rezultati za različite kanale su uspoređeni s rezultatima teorijskih modela kako bi se ustanovilo koji su stupnjevi slobode bitni u opisu mjerenog diferencijalnog udarnog presjeka. Na taj način procijenjeni su efekti mogućih (nn), (pp) i (np) korelacija. Usporedba je napravljena s poluklasičnim GRAZING modelom [1, 4–6]. Model se koristi kako bi se izračunalo na koji način se dijeli ukupni udarni presjek reakcije na različite izlazne kanale, ali ne uključuje korelacije među nukleonima. Tretira reakcije prijenosa mnogo nukleona i u kvazielastičnom i duboko neelastičnom režimu (do određene energije). Jezgre su opisane kao ansambl nezavisnih čestica, koje vibriraju oko svog sferičnog položaja, a glavni stupnjevi slobode su površinske vibracije i jednočestični prijenosi. Do sada je uspješno primjenjen u opisu niza teškoionskih sustava.

GRAZING dobro opisuje sve jednočestične prijelaze. Čisti neutronski kanali su također jako dobro opisani, naročito u ukupnom udarnom presjeku, te se slažu s prijenosom neovisnih nukleona. $(\pm 2n)$ kanali su, kao i u prijašnjim reakcijama, dobro opisani GRAZING modelom. S druge strane, $(\pm 2p)$ kanali su, i kada se gleda samo kvazielastični dio udarnog presjeka, pojačani u odnosu na model, što sugerira prijenos koreliranog para protona uz

prijenose nezavisnih protona. Ponovno opažena asimetrija u neutronskom i protonskom kanalu se može objasniti udarnim presjekom koji je za oko red veličine veći u neutronskom sektoru.

Usporedbom s GRAZINGom vidi se da su jednonukleonski prijenosi, i $(+1p)$ i $(+1n)$, vrlo dobro opisani, dok je eksperimentalni kvazielastični udarni presjek za $(+1p+1n)$ kanal pojačan ~ 2.5 puta u odnosu na račun (vidi sliku 7.11). Ta činjenica ponovno sugerira doprinos koreliranog prijenosa neutrona i protona uz njihov nezavisni prijenos. Razdvajanje kvazielastičnog i duboko neelastičnog dijela udarnog presjeka napravljeno je pomoću već spomenute raspodjele gubitka kinetičke energije nakon što je uočeno da je kutna raspodjela šira od teorijske, posebno za mjerenje na prednjim kutevima i proteže se na puno veće gubitke energije od teorijskog predviđanja. Nakon razdvajanja, kvazielastični diferencijalni udarni presjek ima oblik gausijana s maksimumom na kutu okrznuća kao što se i očekuje, te se daleko bolje slaže u svom obliku s teorijskim predviđanjima, ali je i dalje pojačan u odnosu na model.

Važnost prijenosa koreliranog para neutrona i protona odražava se i u najjače pobuđenim stanjima u jezgri ^{42}K. Njegov gama spektar pokazuje da pored očekivanih niskoležećih stanja negativnih pariteta, čija struktura se može promatrati kao multiplet koji proizlazi iz spajanja nesparenog protona u $d_{3/2}$ i nesparenog neutrona u $f_{7/2}$ orbitalama, pobuđenje stanja pozitivnih pariteta na višim energijama značajno doprinosi. To se može objasniti kao pobuđivanje protona u $f_{7/2}$ orbitalu i njegovo spajanje s nesparenim neutronom u istoj orbitali. Ovo snažno pobuđenje stanja opisane strukture može odražavati prijenos koreliranog para.

Kako bi detaljnije proučili efekt (np) korelacija mjerena je funkcija pobuđenja za ^{92}Mo + ^{54}Fe sustav do energije duboko ispod kulonske barijere PRISMA spektrometrom. Mjerenje slijedi uspješan niz već napravljenih mjerenja na jezgrama zatvorenih i poluzatvorenih ljusaka ^{96}Zr+^{40}Ca i supervodljivom sustavu ^{116}Sn+^{60}Ni gdje je glavni cilj bilo proučavanje korelacija među neutronima. Preliminarni rezultati pokazuju jako pojačanje $(+1p+1n)$ kanala u odnosu na prijenos nezavisnih nukleona.

Zaključak

Diferencijalni i ukupni udarni presjek, te raspodjele energije mjerene su PRISMA spektrometrom u ^{40}Ar+^{208}Pb sustavu na energiji blizu kulonske barijere. Mjerenje je napravl-

jeno na tri različite kutne postavke kako bi se pokrio najznačajniji dio kutne raspodjele i omogućilo dobivanje ukupnog udarnog presjeka. Analiza je napravljena za svaki (Z, A) kanal odvojeno. Određivanje funkcije odziva omogućilo je po prvi puta spajanje tri različite kutne raspodjele mjerene spektrometrom velikog prostornog kuta u jedinstvenu raspodjelu, te određivanje apsolutnog udarnog presjeka za sve kanale prijenosa. Analiza elastičnog raspršenja je iskorištena za određivanje apsolutne normalizacije mjerenih podataka.

Disertacija predstavlja detaljnu studiju mnogih kanala otvorenih u reakciji prijenosa mnogo nukleona i fokusira se na proučavanje svojstava reakcije, poput diferencijalnog i ukupnog udarnog presjeka, te raspodjele ukupnog gubitka kinetičke energije. Prijenos nekoliko nukleona omogućuje i proučavanje relativne uloge prijenosa jednog ili para nukleona. Istodobnim proučavanjem udarnih presjeka različitih kanala, $(\pm nn)$, $(\pm pp)$ i $(\pm np)$, i njihovom usporedbom s teorijskim modelima koji uključuju samo prijenos nezavisnih nukleona, gledao se doprinos korelacija nukleon-nukleon. Također je proučavan doprinos drugih mehanizama reakcije, odnosno doprinos duboko neelastičnog raspršenja u ukupnom udarnom presjeku, što je omogućeno velikim prihvatom PRISME ili doprinos sekundarnih procesa poput evaporacije neutrona što je omogućeno PRISMA-CLARA koincidencijama.

Kao prvi korak, udarni presjek je uspoređen s teorijskim računima koji prijenos nukleona tretiraju pomoću nezavisnog mehanizma, dakle korelacije nisu uključene. Opaženo pojačanje trebalo bi biti potpis doprinosa prijenosa koreliranog para. Rezultati su uspoređeni s GRAZING računom koji dobro opisuje podatke, posebno kvazielastični udarni presjek, za $(\pm xn)$ i $(\pm 1p)$ kanale. Činjenica da su jednonukleonski kanali dobro opisani govori da su stukturalna svojstva i dinamika reakcije dobro opisani modelom. Kanali prijenosa dva protona su pojačani u odnosu na račun, a isto vrijedi i za $(+1p+1n)$ kanal. Utjecaj (np) korelacija je dalje istraživan pomoću γ spektra ^{42}K, koji može pružiti važne dodatne informacije. Osim očekivanih niskoležećih stanja, vidi se jako pobuđenje 7^+ stanja koje se može objasniti vezanjem protona i neutrona u $f_{7/2}$ orbitalama.

Reakcije prijenosa dva nukleona vrlo su važne u proučavanju sparivanja u jezgrama. Nažalost, u teškoionskim reakcijama sam mehanizam reakcije je vrlo kompleksan. Takva mjerenja mogla bi biti komplementarna mjerenjima reakcija prijenosa induciranih lakim ionima, ili mjerenjima ispod kulonske barijere s manjim brojem otvorenih reakcijskih

kanala. Pojačanje $(+1p+1n)$ kanala u odnosu na model koji ne uključuje korelacije, te jakost opaženog stanja gdje su neutron i proton u istoj orbitali i izduženoj konfiguraciji, trebalo bi biti uspoređeno s mikroskopskom teorijom, gdje su uključeni svi bitni stupnjevi slobode i u stukturi i dinamici reakcije. Važno je razviti mikroskopski račun tako da uključuje prijenose parova velikog angularnog momenta. Sparivanje u jezgrama, korelacije među nukleonima, te kako takve korelacije djeluju u reakcijama prijenosa vrlo su važna istraživanja i za buduća mjerenja s radioaktivnim snopovima.

Contents

Introduction

Since the discovery of atomic nucleus, a variety of nuclear reactions with different probes were used to study its properties. Most of the knowledge so far is coming from reactions and studies of structure of nuclei close to the valley of stability. In the last decades, due also to the development of new instrumentations and exotic beams, the interest has enlarged towards the neutron and proton drip lines.

The acceleration of ions at energies above the Coulomb barrier offered the possibility of bringing together two complex systems. In the collision process they might exchange several quanta, of energy and angular momentum and of mass and charge, or they could fuse giving rise to a compound system. At energies close to the Coulomb barrier, transfer reactions represent an important part of the total reaction cross section. They play an essential role in the study of the structure of nuclei. With light ions they provided important inputs for the construction of the shell model and they helped to establish the properties of nucleon-nucleon correlation in nuclear medium. With heavy ions multiple transfer of nucleons becomes available in the reaction giving the possibility to study the relative role of single particle and pair transfer modes.

As mentioned above, the pair transfers in multinucleon transfer reactions (MNT) are a suitable probe for the study of correlations. Possible effects of neutron-neutron (nn) and proton-proton (pp) correlation have been recently discussed in topical review article [1] and references therein. It has been reported that the neutron pick-up channels drop by almost a constant factor for each transferred neutron, as an independent particle mechanism would suggest. The pure proton cross sections behave differently, with the population of the $(-2p)$ channel as strong as the $(-1p)$. This suggests the contribution of processes involving the transfer of proton pairs in addition to the successive transfer of single protons. This apparent proton and neutron asymmetric behaviour, present in all reactions studied so far, is attributed to the almost order of magnitude larger cross

section of the one neutron transfer channel compared with the proton transfer channels. In this way the contribution of the pair transfer mode is masked in the neutron sector.

In this context, it is also important to investigate the role played by neutron-proton (np) correlations. Nuclear models point out that such correlation is expected to be strongest in the $N \sim Z$ nuclei, where protons and neutrons occupy the same shell model orbitals. Since transfer process is governed by optimum Q-value consideration and nuclear structure properties, with stable beams only neutron pick-up and proton stripping channels are dominantly populated. It is particularly important to study the ($+np$) channel since it can be populated via a direct mechanism, while the ($-np$) channel is of complex nature and can be strongly affected by the neutron evaporation mechanism. To reach this goal one can use neutron-rich beams that populate ($\pm nn$), ($\pm pp$) and ($\pm np$) channels with similar strength and give a possibility of their direct comparison.

For multinucleon transfer reaction studies magnetic spectrometer is an ideal tool because it is possible to measure at the same time mass and charge yields, differential and total cross sections, and total kinetic energy loss distribution of different channels produced in the reaction and when coupled with gamma array, coincident gamma transitions for each isotope. PRISMA is a large solid angle magnetic spectrometer of new generation based on the event-by-event reconstruction of ion trajectories inside the magnetic elements. It offers charge and mass identification of reaction products. Its main characteristic is the large solid angle of ∼80 msr. Mass range of accepted ions is between A=20-200, well suited for the beams and energies of Legnaro National Laboratories Tandem accelerator complex.

The understanding of the reaction mechanism depends strongly on the determination of the absolute cross sections and for this reason the response function of the spectrometer has to be carefully evaluated. This study is based on a Monte Carlo simulation of the ion trajectories, on the basis of a ray-tracing method, where the kinematics of the reactions and the geometry of the magnetic elements and detectors are taken into account. The response of the spectrometer depends in a complex way on the entrance angles and the momenta of the reaction products. The major corrections for the channels studied so far are found, as expected, at the edge of the angular acceptance with large differences in absolute values depending on the kinetic energy of the ion.

In this thesis the main focus will be on the ^{40}Ar+^{208}Pb reaction. The ^{40}Ar beam at

260 MeV energy has been accelerated on ^{208}Pb target. Projectile-like fragments have been identified with PRISMA positioned at three different angles covering more than 20 degrees of angular range (most of the transfer flux). The described procedure of correction for the ion transport allowed us to match angular distributions measured with different PRISMA angular settings, which is obtained for the first time with large solid angle magnetic spectrometers. Coincident gamma rays were detected with the CLARA array. Results concerning the structure of the Ar and Cl isotopic chains were published in Refs. [2] and [3]. In this thesis we concentrate on the differential and total cross sections of the strongest transfer channels. The results for different channels will be important for theoretical models to see which degrees of freedom play role in the description of the measured cross sections and that the effect of possible (nn), (pp) and (np) correlations can be evaluated. The comparison was made with the GRAZING code that is relevant for heavy-ion reactions and contains structure informations, so possible influence of nucleon-nucleon correlations may be deduced. These inclusive data are corroborated by complementary analysis of γ spectra.

This thesis discusses main aspects of the ^{40}Ar+^{208}Pb multinucleon transfer reaction and new experimental informations on the (np) correlations will be presented. Through the direct comparison of the extracted differential and total cross sections an additional information on the (nn) and (pp) correlations can be obtained. These correlations may play an important role in ongoing research with radioactive beams.

1 Heavy-ion reactions and nuclear correlations

In this Chapter we will concentrate on the main findings of the collisions of heavy ions ($A \geqslant 20$) at energies close to the Coulomb barrier (around 5 MeV/A).

1.1 Heavy-ion reactions

Nuclear reaction is a very complex quantum mechanical process which depends on both nuclear structure and mechanism of reaction. Although the boundaries between various processes are not sharp, one can still distinguish them, depending on the reaction impact parameter, transferred angular momentum, energy and so on [7–9]. It is generally accepted that with increasing impact parameter the interaction evolves from fusion reactions, which require a substantial overlap of the two nuclei, through deep inelastic processes, to quasi-elastic reactions, which are associated with the most grazing-type collisions [10]. At even larger impact parameter nuclei feel only Coulomb force, and only Coulomb excitation is observed.

1.1.1 Multinucleon transfer reactions

Processes in which nucleons are transferred between the target and projectile play considerable role in heavy-ion collisions, and both pick-up and stripping reactions occur. In particular, for energies close to the Coulomb barrier transfer reactions play important role in the loss of flux from the elastic channel.

The experimental study of transfer reactions have always been of great importance in the understanding of nuclear structure and nuclear reaction mechanism. The nuclear shell model and the studies of particle-particle correlations in the nuclear medium have in fact

received a great benefit from transfer reactions using light ions. With heavy ions, transfer reactions played a very important role for the definition of the reaction mechanism that describes the evolution of the reaction from the quasi-elastic regime to the more complex deep inelastic and fusion [1]. In a single collision it is possible to transfer several nucleons from one nucleus to the other. This gives the possibility to study the relative role of single particle and pair transfer modes. In this way one can investigate the component responsible for the nucleon correlations, pairing in particular, but it is only when several nucleons get transferred that one has a better view on how the mechanism evolves.

In the last decade, the renewed interest in transfer reactions has been mainly due to the realization that multinucleon transfer reactions could be used to populate nuclei moderately rich in neutrons with cross sections large enough to study their structure [11, 12]. This renewed interest benefited from the construction of the new generation large solid angle spectrometers based on trajectory reconstruction, with which one could gain more than an order of magnitude in overall efficiency still keeping a good identification of reaction products [1].

In heavy-ion experiments near the Coulomb barrier one has been able to identify a characteristic type of reaction products where the projectile has lost only a moderate amount of energy and has exchanged only few nucleons with the target nucleus. These reactions are called **quasi-elastic reactions** and are assumed to correspond to collisions in which the surfaces of the two ions have just been in grazing contact, and they essentially keep their identity [8]. This is a type of direct reactions that includes the true elastic scattering. The term direct implies that the reaction is completed in the time required for the incident particle to transverse the target nucleus, so that it interacts only with the surface or with some individual constituents of the nuclei. Quasi-elastic reactions populate well defined quantum states, usually of rather low excitation energy and of the (relatively) high spins with a high degree of selectivity. Angular distributions often exhibit a single peak at the grazing angle. Domination of quasi-elastic reactions is especially emphasized at energies close to the Coulomb barrier, and it makes dominant reaction mode in the low energy region.

When we examine the distribution of masses and kinetic energies of the products of a heavy-ion collision, we may see a broad distribution of outgoing nuclei, in which an appreciable fraction of the incident kinetic energy has been converted into internal excitation

energy. These are called **deep inelastic reactions** or strongly damped collisions. The primary products are also found to be essentially binary. They result from the two heavy nuclei sticking together for a longer time than one would associate with direct reactions, but not long enough for the two systems to fuse into a compound nucleus [7]. Short collision time and large energy losses suggest that in the evolution of the reaction the excitation of surface modes plays an important role being the low-lying modes the main source for the formation of the large deformations [1]. This surface dynamics, governed by the low-lying modes, allows the two ions to stay in close contact for longer time, i.e. to build up the "neck" between the two colliding partners. There tends to be a large loss of kinetic energy in such collisions, but the system still retains memory of how it was formed by showing, for example, a forward-peaked angular distribution. They are characterized by a massive exchange of nucleons, towards the charge equilibration (i.e. N/Z ratio of compound nucleus).

The contribution of quasi-elastic or deep inelastic component in a reaction depends mainly (given a certain mass asymmetry in the entrance channel) on the projectile energy. The height of the Coulomb barrier, by using the two point charges expression, can be written as:

$$E_B = \frac{Z_a Z_A e^2}{r_C} \tag{1.1}$$

where Z_i are nuclear charges and r_C is the interaction distance. For the nuclear part of the nucleus-nucleus potential one can use the Akyüz-Winther parametrization that describes quite well elastic scattering data for several projectile and target combinations:

$$U^N = \frac{-V_0}{1 + e^{(r - R_a - R_A)/a}} \tag{1.2}$$

with the potential depth V_0, the diffusion parameter a and nuclear radii $R_i = (1.2A_i^{1/3} - 0.09)$ fm [1].

1.1.2 Form factors and optimum Q-value

The transfer processes are mainly governed by form factors (spectroscopic informations of colliding nuclei and dynamics) and optimum Q-value considerations (balance of the internal and binding energy in the phase space of colliding nuclei). Due to the characteristic behaviour of the binding energy in the nuclear chart, the process is essentially governed

by the lighter partner of the reaction. In general, the use of lighter stable projectiles on heavy targets results in population of only proton stripping and neutron pick-up channels [13].

The form factor is a matrix element between initial and final states in the transfer process and reflects nuclear structure properties of the donor and acceptor. It weights the relative importance of different channels. The form factor is equal to:

$$f_{\beta\gamma}(\vec{\kappa},\vec{r}) = \langle\omega_\beta|(V_\gamma - U_\gamma)|\psi_\gamma\rangle \tag{1.3}$$

where $\vec{\kappa}$ is the momentum transfer and $\vec{r} = \frac{1}{2}(\vec{r}_\beta + \vec{r}_\gamma)$ represents the centre of mass distances, $|\omega_\gamma\rangle$ constitute a dual base obtained from the overlap matrix, U is the nuclear potential and V is the coupling interaction. At large distances, for the particle transfer form factor one can write:

$$f_{\beta\gamma}(0,r) \sim \frac{1}{\kappa_{a_1'} r} e^{-\kappa_{a_1'} r}. \tag{1.4}$$

The asymptotic behaviour of the form factor is governed by the coefficient $\kappa_{a_1'}$ that contains the binding energy of the single particle state a_1' entering in the transition. For single particle states close to the Fermi energy the decay length of the one particle transfer form factor is of the order of 1.2 fm, thus at large distances the transfer form factor prevails over the nuclear component of the inelastic form factor [1]. In analogy with the macroscopic description of the inelastic scattering, the form factor for transfer can be formulated as the r-derivative of the potential:

$$f_\lambda = \beta_\lambda \frac{\partial U(r)}{\partial r} \tag{1.5}$$

where β_λ is the deformation parameter related to the collectivity of the state and $U(r)$ is the average potential of the entrance and exit channels. This macroscopic form factor has been used for example in the recent analysis of ^{40}Ca,^{58}Ni+^{208}Pb that will be discussed in Chapter 7.

The probability for the transition from the entrance channel α to the channel β in a direct process where the two nuclei barely overlap, and only the tail of the form factor is

relevant, may be written [1]:

$$P_{\beta\alpha} = \sqrt{\frac{1}{16\pi\hbar^2|\ddot{r_0}|\kappa_{a'_1}}}|f_{\beta\alpha}(0,r_0)|^2 g(Q_{\beta\alpha}) \tag{1.6}$$

where $\ddot{r_0}$ is the radial acceleration at the distance of closest approach for the grazing partial wave. Thus the probability for a given transfer is proportional to the square of the form factor times the adiabatic cut-off function that depends on the optimum Q-value of the reaction. The adiabatic cut-off function $g(Q)$ is defined as:

$$g(Q) = e^{\left(-\frac{(Q-Q_{opt})^2}{\hbar^2\ddot{r_0}\kappa_{a'_1}}\right)}. \tag{1.7}$$

The optimum Q-value is:

$$Q_{opt} = \left(\frac{Z_d}{Z_A} - \frac{Z_d}{Z_b}\right)E_B + \left(\frac{m_d}{m_b} - \frac{m_d}{m_A}\right)(E - E_B) + \frac{m_d\ddot{r_0}}{m_a + m_A}(R_A m_b - R_a M_B) \tag{1.8}$$

with E_B Coulomb barrier, Z_d and m_d charge and mass of the transferred particle. Optimum Q-value for charge particle transfer is both system and energy dependant. The adiabatic cut-off function $g(Q)$ defines the actual value of the transition probability whose maximum is at the optimum Q-value. This derives from the requirement that the trajectory of entrance and exit channels matches smoothly close to the turning point where the contribution of the form factor peaks [14]. The bombarding energy dependence of the cut-off function is contained in the $\ddot{r_0}$ term that defines its width (inversely proportional to the collision time).

Figure 1.1 shows the adiabatic cut-off function $g(Q)$ for all one- and two-nucleon transfer channels for the ^{58}Ni+^{208}Pb reaction. Horizontal lines represent, for all channels, the location of all possible transitions (the ground-to-ground state Q-value). Since only the channels whose Q-values lie below the bell-shaped curve can actually occur, it is clear that the only allowed transfers are neutron pick-up and proton stripping. All the other channels are hindered by optimum Q-value consideration. One can also notice that for some channels, in particular the two proton stripping and two neutron pick-up, the reaction mechanism favours transitions leading to high excitation energies. Q-matching conditions constrain the population to states located in a certain Q-value window.

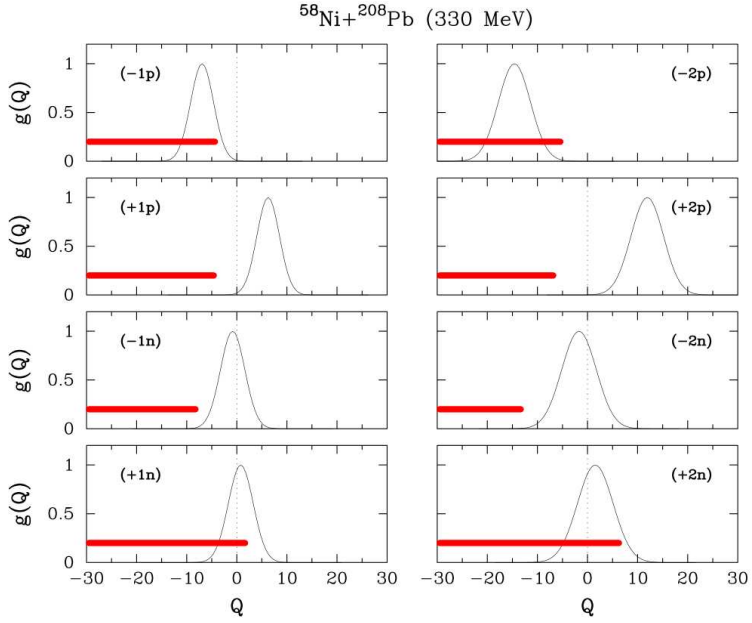

Figure 1.1: Adiabatic cut-off functions for one- and two-neutron and proton transfer channels. Q-value is in MeV. The horizontal line represents the location of all possible transitions [1].

This situation holds for most of the projectile-target combinations available with stable beams, it is only by employing unstable beams that all four kinds of basic transitions become available. Reason for this lies in characteristics of reaction Q-value. In a collision process involving light projectile and a heavy target, the balance of Q-values for the transition to $Z \pm \Delta Z$, $N \pm \Delta N$ is mostly controlled by the lighter partner. Since the contours of binding energy in the NZ plane in the vicinity of the light stable nuclei are roughly symmetric around $N = Z$, a cut for a given element (Z=const.) yields a steeper energy gain toward the lighter isotopes than toward heavier, thus favouring the acquisition of neutrons. If one takes heavier isotopes of a given projectile a transition toward the opposite situation should happen [12]. With neutron-rich projectiles, proton pick-up and neutron stripping channels also open up, leading to the population of the neutron-rich heavy fragments.

Lowering the bombarding energy increases collision time and squeezes Q-value window thus reducing average number of transferred neutrons. On the other side, by increasing the bombarding energy the grazing distance is decreased, thus leading to more intimate collision in the grazing region.

1.1.3 The GRAZING model

The large mass of heavy ions means the associated wavelength is shorter than the one for light ones with the same energy. In many cases the wavelength is short enough to use classical concepts to describe a collision, so one can speak of the ion following a classical trajectory. From the theoretical point of view, a semi-classical approximation has been developed giving the possibility of treating multinucleon transfer reactions both in the quasi-elastic and in the deep inelastic regimes. These calculations are able to predict how the total reaction cross section is shared among the different reaction channels.

The semi-classical model GRAZING was developed by A. Winther and Copenhagen group [1, 4–6] and was proven to reproduce accurately variety of experimental data. The two nuclei are described as an ensemble of independent nucleons that can vibrate around their spherical equilibrium shapes, the basic degrees of freedom being surface vibrations and single particle transfer. The two ions interact via a Coulomb plus nuclear interaction. The Coulomb potential is described by a two point charge expression, while for the nuclear potential a Wood-Saxon parametrisation is used. The exchange of many nucleons proceeds via a multi-step mechanism of single nucleons. In particular, the basic degrees of freedom consist of single particle and surface vibrations around the spherical equilibrium shape, including the lowest 2^+ and 3^- states and the associated giant resonances. For the excitation of the surface modes the model employs the macroscopic approximation whose form factors are proportional to the r-derivative of the ion-ion potential and whose strength are given by the experimental B(Eλ). The exchange of nucleons is governed by microscopic form factors that take into account the single particle properties of the projectile and target and an average single particle level density. Thus, the approximations in the treatment of particle transfer are the use of representative form factors for the transfer and the substitution of the actual distribution of single particle states with a density function.

The predictions from the GRAZING model have been successfully compared to a number of experimental data, including the ^{58}Ni+^{124}Sn reaction (Fig. 1.2) which has been studied in great detail both experimentally and theoretically by the Argonne group [1, 15, 16]. This reaction is one of rare examples where for different bombarding energies, most of the channels have been measured in great detail, from elastic scattering, transfer reactions to evaporation residue, deep inelastic and fission products.

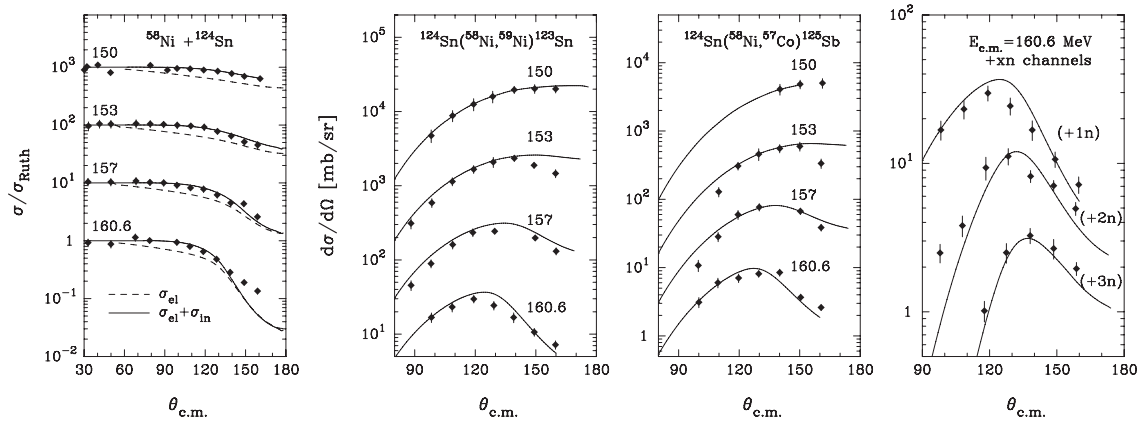

Figure 1.2: Center-of-mass angular distributions for elastic plus inelastic, one-neutron pick-up, one-proton stripping and some multineutron transfer channels calculated with GRAZING for the ^{58}Ni+^{124}Sn reaction. The label in each frame indicates the center-of-mass bombarding energy in MeV [1].

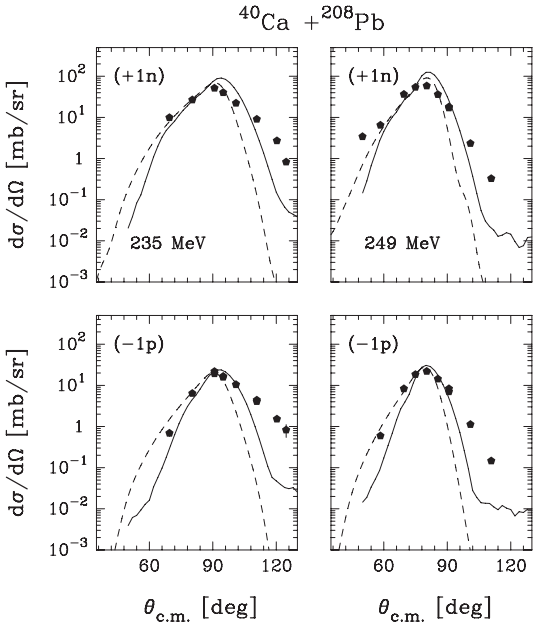

Figure 1.3: For the indicated reactions and bombarding energies the angular distribution of inclusive one-particle transfer reactions calculated with GRAZING (dash) are shown in comparison with those calculated in the CWKB approximation (full line) [1].

The comparison of the GRAZING and CWKB for the ^{40}Ca+^{208}Pb reaction is on Fig. 1.3. The DWBA calculations were done by employing all bound single particle states above the Fermi energy and a full shell below. These calculations have been done by using one-particle transfer form factors constructed from the single particle wave functions of the states involved in the transition and by using the WKB approximation for the distorted waves describing the relative motion. Since the WKB approximation has to be employed

in a complex potential, this calculation was named CWKB.

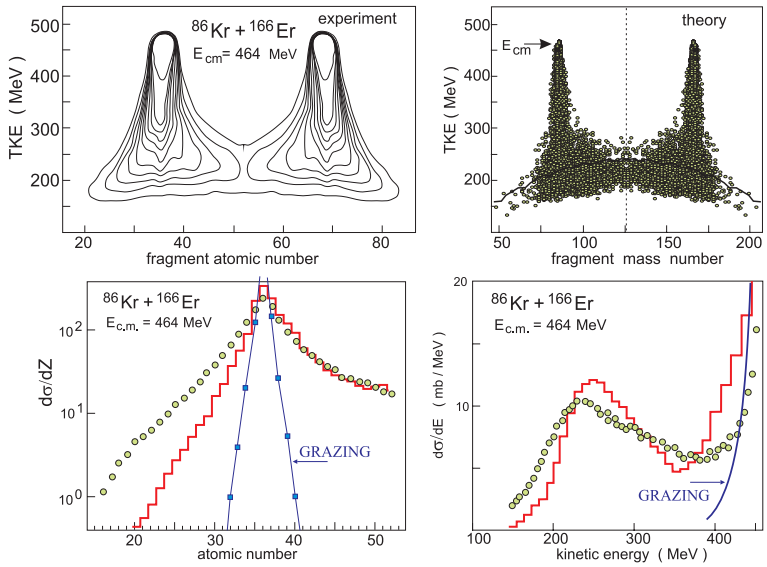

Figure 1.4: Charge, mass and energy distribution of reaction fragments in collisions of ^{86}Kr with ^{166}Er at $E_{cm} = 464$ MeV. The histograms indicate the calculations performed within the model based on the Langevin-type dynamical equations of motion and curves show the GRAZING calculations [17].

The total cross sections of the multinucleon transfer reactions have been recently also studied within the model based on the Langevin-type dynamical equations of motion [18] and time-dependent Hartree-Fock theory [19–21]. The results of the Langevin based model (that includes deep inelastic components) for ^{86}Kr+^{166}Er are plotted in Fig. 1.4 together with results from the GRAZING model (that includes informations about structure of nuclei) [17].

1.2 Nucleon-nucleon correlations

The importance of nucleon pairing in nuclear structure has been established in the early stages of nuclear physics by the determination of the binding energies of nuclei, and the observation of their characteristic odd–even staggering. A. Bohr, B.R. Mottelson and D. Pines recognized the analogy between the excitation spectra of nuclei and of the superconducting metallic state [22]. They noticed, that in addition to the average shell model potential, also acts relatively short-range residual nucleon-nucleon force. For nuclei one may distinguish superconductivity in connection with dynamical aspects (as experienced in transfer of nucleon pairs), and superfluidity for the static properties of nuclei. The

pairing energy, although small compared to the total binding energy, is comparable to the typical energy of the lowest nuclear excitations, and thus controls almost every feature of nuclei close to the ground state. The pairing in nuclei is connected, as in solids, to the correlation of nucleons on time reversed orbits in well defined configurations [23, 24].

The transfer of pair of nucleons can happen in two ways, sequentially where nucleons are transferred one after the other, or simultaneously, in one-step, where a correlated pair of nucleons is exchanged. So far, with heavy ions, it has been found that the sequential transfer dominates over the simultaneous ones, and that in both processes the transferred nucleons display equivalent pairing correlation which is a consequence of the fact that correlated pairs are weakly bound and highly extended objects [25].

Nucleon-nucleon correlation have been studied with several methods. Most important experimental techniques that have been used are radiochemical methods, magnetic spectrometers and particle-γ coincidences giving the possibility to study two-neutron transfer between well selected states [23]. We will concentrate on correlation studies with magnetic spectrometers.

Light ion induced one and two-particle transfer reactions were exploited for decades to study correlations. They are highly selective in energy and angular momentum transfer. Very good energy resolution was obtained which offered the possibility to study specific exited states and to probe single particle properties like spectroscopic factors and shell structure [26–28].

Heavy-ion transfer reactions allow simultaneous comparisons of observables for (nn), (pp) and (np) pairs and hence are an ideal tool for the study of the residual interaction in nuclei. Difficult theoretical interpretation and limited energy resolution of available instrumentation slowed the progress in the past. Interpretation is more complex due to absorption, since inelastic excitation causes the directness to be obscured by multi-step process [29].

Today, large solid angle spectrometers allow detection of large number of transferred nucleons at the same time. Good A and Z identification is usually obtained, however energy resolution is limited to around 1 MeV which is mostly not sufficient to separate low-lying excitations. To disentangle the correlation from other processes present, the knowledge of dynamics and the evolution from quasi-elastic to deep inelastic processes becomes important.

Two possible approaches were used to study correlation with transfer reactions: angular distribution at fixed bombarding energy (near the Coulomb barrier) and excitation function at fixed angles (from near to deep below the Coulomb barrier). So far this approach was used to gain knowledge about (nn) and (pp) correlation.

Reactions around the barrier

The correlations and their role in the transfer process have been studied in collisions of nuclei with closed or near-closed shells at energies near the Coulomb barrier in several systems, for instance ^{40}Ca+^{208}Pb and ^{58}Ni+^{208}Pb [30–32]. It was observed that the cross sections for the neutron pick-up channels drop by almost a constant factor for each transferred neutron, as an independent particle mechanism would suggest. The population of the $(-2p)$ channel is as strong as the $(-1p)$, which suggests the contribution of processes involving the transfer of proton pairs in addition to the successive transfer of single protons. The fact that the same behaviour was not observed in the neutron channels was attributed to much larger cross section, thus the contribution of a pair-transfer mode is masked by the successive mechanism.

Reactions below the barrier

Measurements of inclusive cross sections at and above Coulomb barrier have very complex reaction mechanism and hence difficult theoretical interpretation due to the presence of many competing processes. Below the barrier number of open channels is smaller and hence mechanism is less complex, but measurement itself is very difficult. The cross sections are small, and this demands detectors with high efficiency. Significant progress was made by using reactions in inverse kinematics, where ions are forward focused (which means high detection efficiency) and with high kinetic energy (for energy and therefore mass resolution). The closed shell ^{96}Zr+^{40}Ca system [33] and "superfluid" ^{116}Sn+^{60}Ni system [34] were recently measured. The microscopic theory, that incorporated nucleon-nucleon correlations, essential for the population pattern of the single particle levels around the Fermi energy, for the first time very well reproduced the experimental data, and in particular the transfer probability in slope and absolute value for two neutrons, in all energy range, in the ^{116}Sn+^{60}Ni system [34] with very well Q-value matched transition for $(+2n)$ channel.

1.2.1 Neutron-proton correlations

The role played by (np) correlations is still a very challenging issue. The enhancement of deuteron transfer reactions by (np) pairing was for example addressed by P. Fröbrich who predicted an increase of 2.44 in the cross section over the single particle estimate for light ion induced reaction [35]. Nuclear models point out that such correlation is expected to be strongest in $N \sim Z$ nuclei where neutrons and protons occupy the same orbitals. As one moves out of the $N \sim Z$ nuclei, (nn) and (pp) pairs are favoured.

Whether strong deuteron-like isoscalar $(T = 0)$ correlations exist remains an open question. The reason is that in order for a nucleon pair to exploit the short-range nuclear force and form a correlated pair, the constituent nucleons must occupy orbits within the same valence shell. Such "normal" pairing couples the nucleons in pairs with opposite spins and occupying orbits which are symmetric with respect to time inversion. This is called isovector pairing $(T = 1)$ with zero total angular momentum for each pair of nucleons $(S = 0)$ [36].

Several methods have been adopted to probe (np) correlations:

- very precise measurements of binding energies and comparison with theory, which showed a strong evidence for the presence of isovector (np) pairing [37]
- gamma spectroscopy was used to identify spin-aligned, isoscalar neutron-proton pair; for example in ^{92}Pd three new γ-ray transitions have been ordered into a ground-state band and shell model calculations were made predicting the appearance of ground-state and low-lying yrast structures based on spin-aligned systems of (np) pairs [38]
- knock-out reactions where a spatially correlated (np) pair is knocked-out; for example in the ^{12}C projectile at high energy (np) pair was knocked-out by the ^{12}C target and comparison of yields corresponding to (np), (pp) and (nn) channels was made [39].

The addition or removal of a (np) pair from even-even nuclei should be an important additional tool to study these correlations. In this thesis we will present results from heavy-ion multinucleon transfer reactions and the study of nucleon-nucleon correlations, in particular neutron-proton correlations. As this method was not used for (np) correlation study in the past, available informations are scarce. Thus, results should provide new valuable informations for future experiments. The population of $(-np)$ channel is often

marred by complex secondary processes, therefore one should look at the $(+np)$ channel, which can be populated via a direct mechanism. On the other hand this channel is quite difficult to reach and one must deal with reactions that, besides proton stripping and neutron pick-up channels, also populate proton pick-up channels. The comparison of the experimental cross section for the $(+np)$ channel with those of the individual $(+1n)$ and $(+1p)$ channels may provide information on the (np) correlation. The comparison with theoretical models for $(\pm nn)$, $(\pm pp)$ and $(\pm np)$ channels will be important to see which degrees of freedom play role in the description of the measured differential cross sections and that the effect of possible correlations can be evaluated. In this context, similarly to previous studies, two measurements were performed.

The ^{40}Ar+^{208}Pb experiment

The ^{40}Ar+^{208}Pb system was measured at $E_{lab} = 260$ MeV with the PRISMA spectrometer, coupled to the CLARA array. Angular distributions were measured for the first time with large solid angle spectrometer by taking into account response function in order to study correlations. The use of magnetic spectrometer in combination with γ arrays allows to study the population strength of the excited states. In this way important complementary information can be obtained. This is particularly important in the view of the population of states where protons and neutrons occupy similar orbitals, in this case in $N > Z$ nuclei.

The ^{92}Mo+^{54}Fe experiment

These results can be compared, as a second step, with sub-barrier measurement of the excitation function for the ^{92}Mo+^{54}Fe reaction. System was measured with PRISMA from the Coulomb barrier to $\sim$20% below where good ion identification was obtained. In this system one gets as close as possible to $N = Z = 27$ region. The comparison of enhancement factors in light and heavy-ion induced reactions in that region may strongly help in the understanding of the pair transfer degrees of freedom.

1.3 Recent advances in reaction mechanism

Significant advances have been achieved in the last years in the field of multinucleon transfer reactions at energies from near to below the Coulomb barrier. Traditionally, with

multinucleon transfer reactions at Coulomb barrier energies one can investigate which degrees of freedom are relevant for reaction dynamics. Multinucleon reactions allow transfer of several nuclei at the same time and valuable information on nucleon-nucleon correlations were derived, especially from measurements performed below the Coulomb barrier. Also, other aspects of reaction mechanism, like heavy-ion fusion with electrostatic deflector, are currently investigated [40–44].

The coupling of PRISMA [45] with large γ arrays, CLARA [46] and AGATA demonstrator [47], allowed to perform γ-particle coincidences, thus studying not only reaction mechanism, but also nuclear structure of populated transfer products [11, 48–51]. In this way one can detect the transfer strength to the lowest excited levels of binary products and perform γ spectroscopy for nuclei moderately far from stability, especially in the neutron-rich region, for masses from Ne to Xe. In many cases, the new γ transitions have been uniquely attributed to the specific isotopes identified by the spectrometer. It was also possible to investigate at once chains of isotopes populated in the same reaction [2, 3]. Thus, poorly known (neutron-rich) isotopes could be more easily compared with better known ones, making the attribution of level properties more reliable. Here, in the recognition of the character of the lowest populated states the main characteristic of the multinucleon transfer reaction mechanism helps in the attribution of the spins of the new transitions [52]. These nuclear structure studies will continue with planned large γ-array GALILEO [53].

The transfer mechanism provides a tool to build-up a high degree of alignment. On this basis, exploiting the granularity of the γ arrays, measurements of γ-ray angular distributions and linear polarizations have been shown to be a powerful tool to determine the multipolarity and electromagnetic character of the transitions [54, 55].

A novel powerful technique has been successfully developed to measure lifetimes of excited states populated in binary reactions, by exploiting the different intensities of the Doppler shifted γ rays emitted before and after a degrader placed close to the target and has been used for a variety of nuclei [56–59].

Besides the "light" partner products, the "heavy" partners are presently also studied. The direct detection of the heavy products ($A \sim 150 - 200$) is notoriously very difficult. Significant progress can be made by using reactions in inverse kinematics, where ions are forward focused and with high kinetic energy [52]. The second time-of-flight system

has been constructed and detected (with low Z and A resolution) the coincident heavy fragments produced in binary reactions in kinematic coincidence with PRISMA. In this way transfer induced fission and evaporative processes, which may strongly affect the final yield distribution, can be studied. These processes are essential for understanding the population pattern in the heavy regions (like those around Pb), where emphasis is presently on measuring nuclear properties for astrophysical interest, like r-process [60]. High resolution kinematic coincidence measurement would be very welcomed and would bring important new information on these processes.

Ongoing studies are of primary importance for future reactions with radioactive ion beams where multinucleon transfer is a competitive tool for the study of neutron-rich nuclei, at least for certain regions of the nuclear chart, that can be hardly accessed by fragmentation or fission reactions [52].

1.4 Reactions with radioactive beams

The history of extending the nuclear chart is closely connected to the technical advances of radioactive beams. However, most of the present-day knowledge of the structure of the atomic nucleus is still based on the properties of nuclei close to the line of β-stability where the proton-to-neutron ratio is similar to that of stable nuclei. Extrapolating this to the region far from stability is quite dangerous and already it is now clear that some of the "basic truths" of nuclear physics have to be revisited [61]. For instance, theoretical predictions and experimental results have indicated that well-known magic numbers for Z and N seem to be dependent on the N/Z ratio, thus implying a more local applicability, and significant changes of the shell structure are predicted for neutron-rich nuclei. The exact location of the next spherical shell closures beyond $Z = 82$, $N = 126$ is still an open question (they are predicted at $Z \sim 114$ and $N \sim 184$). Due to the bending of the stability line toward the neutron axis, traditionally used fusion reactions of stable nuclei may produce only proton-rich isotopes of heavy elements [17].

One of the promising tool for the production of the new neutron-rich heavy (and superheavy) nuclei is the use of the multinucleon transfer reactions at energies close to the Coulomb barrier. These reactions can be used for the production of new neutron-rich nuclei located along the closed neutron shell $N = 126$ which is an area of the nuclear map

that has the largest impact on the r-process [62]. The origin of heavy elements from iron to uranium remains one of the great unanswered questions of modern physics. Informations about neutron-rich nuclei are crucial to advance current understanding of nuclear interaction, and will have an important effect on the understanding of astrophysical phenomena [13]. Furthermore, nucleon correlations and clustering seem to play a much more important role in nuclear binding than anticipated. The dependence of the nuclear interaction on this specific degree of freedom, the N/Z ratio, is believed to shed a new and elucidating light on a number of aspects of the nuclear interaction and dynamics [61].

The creation and study of unstable nuclei has been pursued for many years using stable beams on stable or long-lived targets. To enlarge the scientific scope and test existing knowledge far from the line of stability, the radioactive ion beam facilities become crucial. Reactions induced by radioactive beams have attracted a great deal of interest, because of particular phenomena observed in reactions with these weakly bound projectiles. Major facilities proposing a large variety of beams exist in the world today. New big upgrades and new major large scientific facilities include FAIR at the GSI, Germany, SPIRAL2 at GANIL, France, HIE-ISOLDE at CERN, Switzerland, and SPES at LNL-INFN, Italy. The two main RIB facilities in North America, the FRIB at MSU and TRIUMF in Vancouver, Canada are also going through major upgrades [63]. Thus, radioactive beams will be important tool for future studies.

The understanding of nucleon-nucleon correlations is becoming more important in research with radioactive beams, with both neutron-rich and proton-rich nuclei. The pairing force is expected to be significantly modified with the change of the N/Z ratio [60]. On the proton-rich side, mainly along the heavy $N \sim Z$ line, the neutron-proton pairing will be the main issue, as compared to the very neutron-rich region (but still not at the drip-line), characterized by the occurrence of a pure neutron skin [23]. Interesting question also is whether and to what extent the form factors and matrix elements used with stable beams need to be modified in nuclei with large neutron/proton excess. The comparison of data with microscopic calculations and cross comparison between reactions performed with stable and radioactive beams should then evidence new peculiar effects of the pairing interaction and address new ideas on how it should be modified.

2 Experimental apparatus

F. W. Aston built in 1919. the first functional mass spectrometer based on focusing of charged particles with electric and magnetic fields [64]. With that spectrometer he showed the first evidence for existence of naturally occurring isotopes and subsequently identified around 210 of them. Ever since then magnetic spectrometers have been one of the most versatile and powerful tools for measurements in nuclear physics.

Magnetic spectrometers have always played an important role in the study of transfer reactions, as they not only provide a complete identification of the reaction products, but also allow the extraction of differential and total cross sections. A significant improvement has been achieved in the last decade with the advent of a new generation of large acceptance magnetic spectrometers (PRISMA [45], VAMOS [65] and MAGNEX [66]), with solid angle as large as ∼100 msr. Unlike conventional spectrometers, here the identification of the reaction products depends on software reconstruction of the ion trajectories. When they are coupled to modern γ arrays it is possible to investigate structure properties of nuclei relatively far from stability that are weakly populated in nuclear reaction. This is the case of the PRISMA-CLARA/AGATA setup, at INFN Legnaro National Laboratories (Italy) and of the VAMOS-EXOGAM/AGATA setup, at GANIL Laboratory (France).

The PRISMA-CLARA/AGATA experimental set-up, combining a large acceptance magnetic spectrometer with a γ-detector array, allows to fully identify a particular reaction product and to investigate its excitation energy spectrum and the associated γ-ray spectra. Mass distribution is obtained from position measurements together with time of flight information, that are measured with refined high-resolution detectors [1]. The spectrometer's characteristics make it suitable for experiments in the field of reaction dynamics at low energies as well as for nuclear structure studies, when coupled with a modern array of γ detectors. Description of set-up follows in next sections.

2.1 Development of magnetic spectrometers

The development of magnetic spectrographs emerged in the past from the need to distinguish excited states populated in light ion transfer reactions. This was achieved by combining magnetic elements of different complexity to focus momenta at definite positions on the focal plane. Q3D or split pole devices have been extensively used for studies of one and two nucleon transfer reactions and Q3D with an improved energy resolution (10 keV) are still employed for detailed spectroscopic studies [Ref. 1, and references therein]. Q3D as name says consists of one quadrupole that is focusing ions to focal plane and three dipoles that separate ions with different p/q ratios. In this way aberrations of second and higher order could be corrected and solid angle could reach 5-10 msr.

Time-of-flight (TOF) spectrometers have been designed with magnetic quadrupole elements which focus ions of different atomic charge states to a relatively small focal plane. A good A and Z resolution for medium mass ions could be preserved, although with lower energy resolution that is of the order of a few MeV. Measurement of TOF and energy allows good resolution of mass thanks to the large path of the ions (several meters). The example is PISOLO time-of-flight spectrometer in INFN-LNL, Italy with solid angle of $\sim$3 msr.

Due to large energy dynamic range of transfer products in heavy-ion reaction, it is difficult to attain a good resolution and sufficient detection efficiency at the same time. Early magnetic spectrometers have been designed with good resolving power explicitly for heavier ions, but with the drawback of having a very small entrance solid angle. A reasonably large solid angle could be obtained by adding focusing quadrupole elements in the ion optical system. New magnetic spectrometers that are based on simple magnetic elements need to use ray-tracking methods for complete ion identification in nuclear charge and mass due to the ion optical aberrations [67, 68].

2.2 The PRISMA spectrometer

The large solid angle spectrometer PRISMA [1, 45] has been designed for the identification of nuclei produced in heavy-ion binary reactions at energies E_{lab}=5-20 MeV/A that are produced with ALPI-TANDEM accelerator complex in Legnaro National Laboratories,

Italy. Main design characteristics of PRISMA are:

- large solid angle of 80 msr, which corresponds to acceptance of $\Delta\theta = 12°$ in the dispersion (horizontal) plane and $\Delta\phi = 22°$ in the vertical plane
- wide momentum ($\pm$10%) and energy ($\pm$20%) acceptance
- maximum Bρ=1.2 Tm
- dispersion $\Delta p/p \approx$ 4cm/%
- resolving power $p/\Delta p \approx 2000$
- energy resolution up to 1/1000 (via TOF)
- nuclear charge (Z) resolution $\approx$1/60
- mass (A) resolution $\approx$1/300 obtained with TOF measurement
- capability of rotation around the target in a wide angular range from -30° to +130°
- rate capability up to 100 kHz.

The spectrometer has following components:

- two optical elements:
  - a quadrupole singlet
  - a dipole magnet
- the entrance and focal-plane detectors:
  - a Micro-Channel Plate (MCP) entrance detector that provides bi-dimensional position and the time of flight (TOF) information [69]
  - a Multi-Wire Parallel Plate Avalanche Counter (MWPPAC) focal plane detector for bi-dimensional position and the time of flight (TOF) information [70]
  - an Ionization Chamber (IC) for energy loss and total energy measurements.

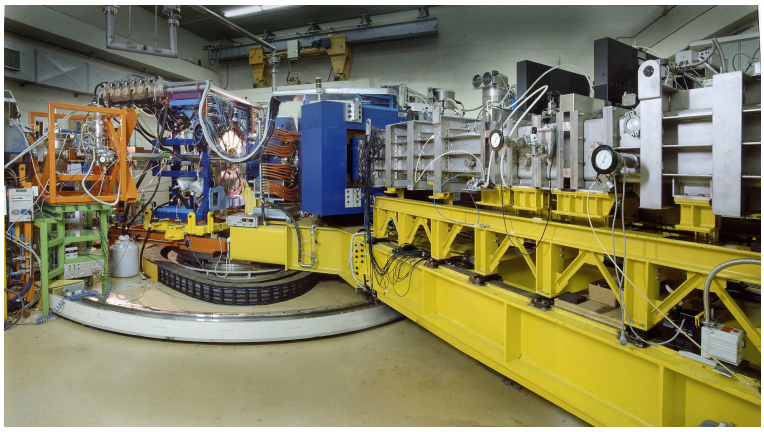

Figure 2.1: Photograph of the PRISMA spectrometer coupled to the CLARA array [71].

The time of flight information comes from the timing signals of the MCP and the MWPPAC detectors. Since the focal plane detector is at a large distance (∼6 m) from the entrance detector, the time of flight is typically quite large (200 - 400 ns). A photograph of the magnetic spectrometer PRISMA is shown in Fig. 2.1, while schematic view is given in Fig. 2.2.

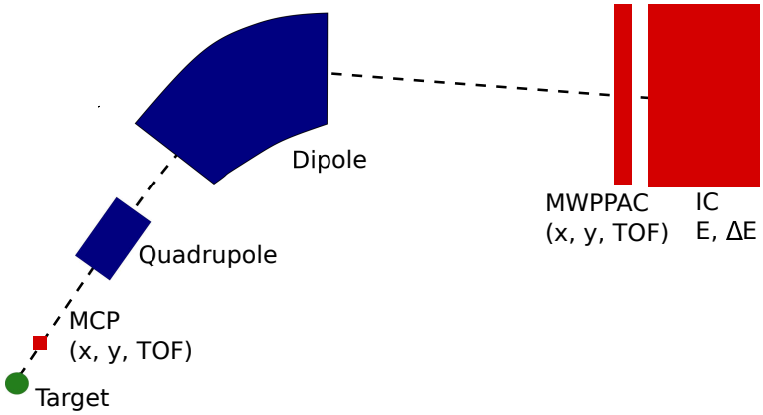

Figure 2.2: Schematic layout of the magnetic spectrometer PRISMA.

Trajectories are different for various products with different p/q ratio and by choosing appropriate magnetic fields it is possible to adjust the system to record a specific range of nuclear products. We will now present the detection system of PRISMA in more details.

2.2.1 Micro Channel Plate (MCP)

Micro Channel Plate (MCP), the entrance detector for the PRISMA spectrometer, provides time and position information in both X (along the dispersion plane) and Y direction. The detecting surface is based on a large area Micro-Channel Plates (MCP) that are basically a network of electron multipliers. The active area of the MCP is 80×100 mm^2 and covers the whole solid angle of PRISMA at a distance of 25 cm from the target. A photograph of the detector is shown in Fig. 2.3A, while schematic layout is given in Fig. 2.3B.

A 20 $\mu g/cm^2$ thin Carbon foil is passed by the particles at an angle of 135° (with respect to the optical axis of the spectrometer) generating secondary electrons. These backward emitted secondary electrons are accelerated towards the MCP by an electrostatic field and guided by a parallel magnetic field produced by an external coil (120 Gauss). This limits the spread of the electron cloud, preserving the particle position information. The accelerated electrons reach the MCP pair surface and undergo multiplication. The

(A) Photograph of the MCP detector.

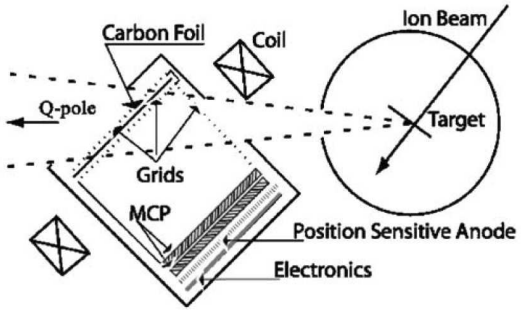

(B) Schematic view from above of the MCP detector.

Figure 2.3: The MCP detector [69].

produced charge is collected by the position-sensitive anode. Position resolution is about 1 mm which corresponds to angular resolution smaller than 0.5°.

The intrinsic time resolution of the MCP detector was measured to be 250-350 ps, and its efficiency with the heavy ions is near 100%. The detector can withstand high counting rate (100 kHz) which allowed it to be installed so close to the target.

2.2.2 Ion optical elements

The optical system of the spectrometer consists of a quadrupole singlet, used to focus the ions on the vertical axis down to the dispersion plane, and a dipole magnet, used to bend the trajectories of the ions travelling to the focal plane detectors depending on their p/q ratio.

The quadrupole singlet is mounted 50 cm away from the target, and its main purpose is collection efficiency. This magnet focuses in the vertical (Y) direction and defocuses in the horizontal (X) direction.

The dipole magnet is placed 60 cm from the exit window of the quadrupole. It is of the uniform field type and has a bending angle of 60° for the central trajectory. The bending radius (i.e. radius of curvature) corresponding to a trajectory laying on the optical axis is 1.2 m and the maximum magnetic field is 1 T, which corresponds to a maximum rigidity of Bρ = 1.2 Tm.

The fringing fields are small enough compared to the inner field of magnets since the ratio length over diameter is slightly below the limit for the fringing field domination. After dipole, ions follow straight trajectory and ∼6 meters after MCP enter into

MWPPAC.

2.2.3 Multiwire Parallel-Plate Avalanche Counters (MWPPAC)

The focal plane detector consists of an array of Multiwire Parallel-Plate Avalanche Counters (MWPPAC) providing X, Y and timing signals, followed by a multi-parametric transverse field Ionization Chamber array (IC) providing multiple ΔE signals. The focal plane detectors fulfil the following requirements:

- good nuclear charge resolution for ions up to Z$\sim$60 and at energies 2-10 MeV/A
- energy resolution $\leq 2\%$
- fast timing ($\sim$300-400 ps)
- position resolution around 1 and 2 mm for X and Y position, respectively
- very large area to fully exploit the acceptance and dispersion of PRISMA
- counting rates as high as 100 kHz.

(A) Photograph of the MWPPAC detector.

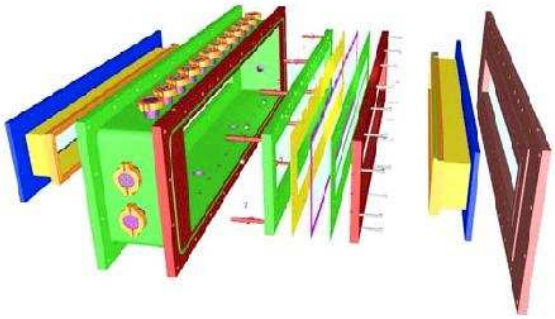

(B) Schematic layout of the MPWPPAC detector.

Figure 2.4: The MWPPAC detector [70].

A photograph of the detector is shown in Fig. 2.4A, while schematic layout is given in Fig. 2.4B. The MWPPAC array consists of 10 equal sections on the horizontal axis for a total active focal plane surface of 100×13 cm^2. The detector has a three electrode structure: a central cathode (polarized at high voltage) for timing, and X and Y wire planes for the position, symmetrically placed, at ground potential, with respect to the cathode and at a distance of 2.4 mm. On the horizontal axis each section has 100 wires distributed on 100 mm with a step of 1 mm. The vertical axis is made of one section over entire length (1 m) with a 1 mm wire step, to preserve the electric field symmetry. As the Y direction is not so crucial in the trajectory reconstruction, the wires are connected

in groups of two with a 2 mm position resolution. The position signals are derived with the delay-line method, hence one has two signals from each section, one on each side, whose relative delay is proportional to the position of the incoming ion. Each wire is an independent counter. The avalanche produced by the impinging particle is well localized in space; due to the narrow spacing between the detector planes the charge is induced mainly on a single wire and therefore the x_{PPAC} and y_{PPAC} resolutions are determined by their steps.

The TOF signal in PRISMA is determined by the time difference between the cathodes of the MWPPAC (start) and the MCP time signal (delayed timing signal stop) with analog TAC units. As a consequence, horizontal position, cathode number events and TOF are registered for each of 10 sections, while vertical position is common for all sections. The OR of the cathode signals is used as a master trigger for the data acquisition system.

2.2.4 Ionization Chamber (IC)

The focal plane MWPPAC detector is followed by an Ionization Chamber, IC, which is used to measure the kinetic energy of the ions as well as their energy loss in the gas. The array of IC is 72 cm downstream of the MWPPAC with an active full size volume of 120×13×100 cm^3 (width×height×depth, respectively). It is divided in ten equal sections on the horizontal axis (as is MWPPAC) and in four equal sections (of 10×25 cm^2) in depth. Figure 2.5 shows an expanded view of the IC. It consists of 40 anode pads, a common Frisch grid and a common cathode.

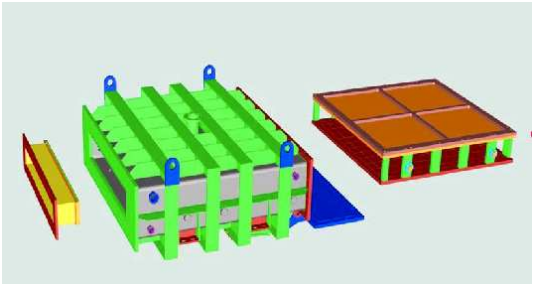

Figure 2.5: Schematic layout of the IC detector [72].

The IC is operated with methane CH_4 or freon CF_4. The best results have been obtained with methane (99.99% purity) which is a relatively fast gas (has a high electron drift velocity), thus allowing to preserve good energy resolution even with the high counting rates needed in the experiments. CF_4, with a higher stopping power, is used for

more energetic heavy ions. Number of electron-ion pairs created in the gas is separated by electric field, and is proportional to the particle's energy.

The segmentation in depth allows different combinations of $\Delta E - E$, being ΔE the energy loss in the first section, or first two sections, and E the sum of the energy loss in all four sections. Additional sections are placed on both sides of the chamber (side sections) and they act as veto to eliminate from the data the ions with highly bent trajectories that are going partially outside the IC active volume and for which the E_{tot} is not correctly measured.

The large dimension of the IC, possibility to differently combine subsections, selection of gas and gas pressure adjustment allow identification of ions that differ by more than 20% in kinetic energy. Through the optimization of all these parameters, beside a good Z resolution, an energy resolution of $\sim$1-2 MeV has been achieved.

2.3 The CLARA array

The obtained energy resolution of magnetic spectrometers cannot yet compete with the excellent energy resolution achieved by the use of high purity germanium (HPGe) gamma detectors. Excited state discrimination can be performed only in suitable nuclei where levels are sufficiently separated [73]. On the other hand, large γ arrays are known to be very powerful tools for nuclear spectroscopy studies of nuclei produced in transfer reactions, especially for very heavy nuclei. For heavy-ion collisions at energies near or slightly above the Coulomb barrier reaction dynamics and nuclear structure influence each other to a large extent and informations obtained with γ arrays give important complementary informations also for reaction studies.

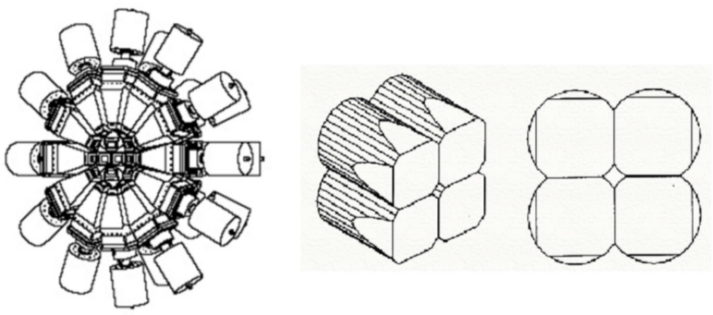

Figure 2.6: Scheme of the CLARA array is on the left panel. Scheme of the clover detector is on the right panel [72].

The CLARA array [46], shown in Fig. 2.6, is a γ-detector array with 25 HPGe clover-type detectors [74] that was associated to PRISMA in numerous experiments performed at LNL. Each clover detector is composed of four HPGe crystals, each with a diameter of $\approx$50 mm, mounted in a single cryostat. The detector is surrounded by BGO scintillators acting as anti-Compton shields, namely rejecting events which have triggered both the Ge and the BGO detectors as a consequence of a Compton scattering interaction. In this way a large reduction of the Compton background can be achieved resulting in a peak to total ratio of 50%. The total photopeak efficiency of CLARA is of the order of 3% for E_γ=1.33 MeV. As a thin target ($\leq$1 mg/cm^2) is used and γ rays are emitted in flight, it is mandatory to perform Doppler correction. This is done from the knowledge of the reconstructed velocity vector in PRISMA. Typical γ-ray energy resolution obtained after Doppler correction is 0.6% to 0.9% over the whole velocity distribution of the projectile-like products detected in PRISMA.

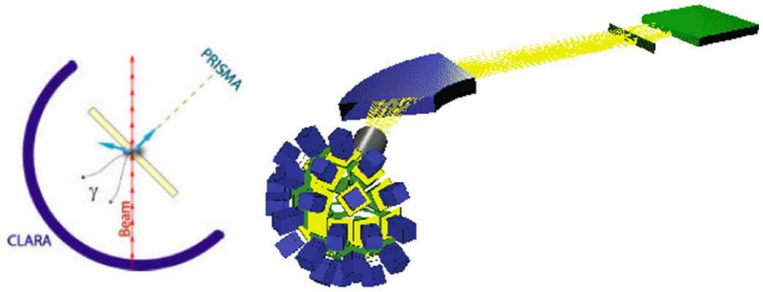

Figure 2.7: Coupling of the PRISMA spectrometer and the CLARA array [72].

The CLARA array was positioned in a hemisphere near the target position and opposite to PRISMA, with most of the Ge crystals placed at large azimuthal angles, between 100° and 180°, with respect to the entrance direction of the spectrometer. This configuration can be seen in Fig. 2.7. More details about the CLARA configuration are given in Appendix B.

3 The experiment and data analysis

This Chapter will present general procedure for PRISMA and CLARA data analysis, with the ^{40}Ar+^{208}Pb reaction as an example.

3.1 The ^{40}Ar+^{208}Pb experiment

Multinucleon transfer reaction ^{40}Ar+^{208}Pb was studied by using the most neutron-rich stable argon isotope, ^{40}Ar, to populate both proton and neutron stripping and pick-up channels. Projectile-like fragments have been identified with the PRISMA spectrometer, while the coincident γ rays were detected with the CLARA array. In this way mass and charge yields, differential and total cross sections, and total kinetic energy loss distributions of different multinucleon transfer channels produced in the ^{40}Ar+^{208}Pb reaction were measured together with coincident electromagnetic transitions that can be assigned to specific isotopes. Characteristics of reaction are summarized in Table 3.1.

Table 3.1: Characteristics of the ^{40}Ar+^{208}Pb multinucleon transfer reaction.

Reaction	**^{40}Ar+^{208}Pb**
Projectile	^{40}Ar at E_{lab}= 260 MeV
PRISMA angles	46°, 54° ($\approx$ grazing angle) and 59°
Beam current	$\approx$7 pnA
Target	^{208}Pb (99.9 % isotopically enriched, 2 mm strip)
Target thickness	300 μg/cm^2 with 15 μg/cm^2 carbon backing

The ^{40}Ar beam has been extracted from the ECR ion source of PIAVE, pre-accelerated and injected into the superconductive Linac ALPI with final energy of E_{lab}= 260 MeV

(6.5 MeV/A), which is ≈30% above the nominal Bass barrier (193 MeV) [9].

The ^{40}Ar+^{208}Pb reaction has been measured at three different PRISMA angles θ_{lab}=46°, 54° and 59° to cover most of the transfer flux. The coincident γ rays were measured for a longer time at the grazing angle, 54°, to achieve sufficient statistics for detailed studies of the transfer strength distribution over the final excited states.

3.2 Data Analysis

A magnetic spectrometer provides the momentum over the atomic charge state ratio (p/q). An additional parameter is needed to obtain mass, and a commonly used one is the time of flight. The mass identification of the reaction products with PRISMA can only be obtained with an event-by-event reconstruction of the ion trajectories inside the magnetic elements. For the reconstruction a fast algorithm has been employed using measured parameters:

- entrance detector positions x_{MCP}, y_{MCP}
- focal plane positions x_{PPAC}, y_{PPAC}
- time of flight TOF
- energy loss ΔE and total energy E.

Results of trajectory reconstruction are:

- the curvature radius inside the dipole magnet ρ
- path length L
- total energy E (via TOF)
- mean path of ions R in IC (range).

The analysis requires several important steps [72]:

- the atomic number Z is selected by plotting the range or the energy loss in the IC versus the total energy
- the ratio A/q is obtained from the position of the ion at the focal plane
- the absolute value of the velocity is equal to the ratio of the length of the trajectory of the ion and TOF
- the direction of the velocity is obtained from the position of the ion on the MCP start detector.

In following section data analysis will be discussed in more details.

3.2.1 The PRISMA data analysis

First step in the analysis is calibration of the raw data in order to obtain physical informations event-by-event. General procedure for analysis of PRISMA data, valid for all experiments, will be presented. Detail explanation of calibration procedure for PRISMA detectors is given in Appendix A and only main characteristics will be given in this subsection.

MCP position calibration

Figure 3.1A shows the raw data of the x_{MCP} and y_{MCP} signals without and Fig. 3.1B the same spectra with coincidence with the focal plane detector MWPPAC. The large difference in statistics and event distributions is clearly visible. Due to the proximity of the MCP to the target, the MCP surface may be triggered not only by reaction products, but also by many undesired events, such as electrons, scattered beam and so on. These undesired events are rejected by requiring the coincidence of the MCP and MWPPAC.

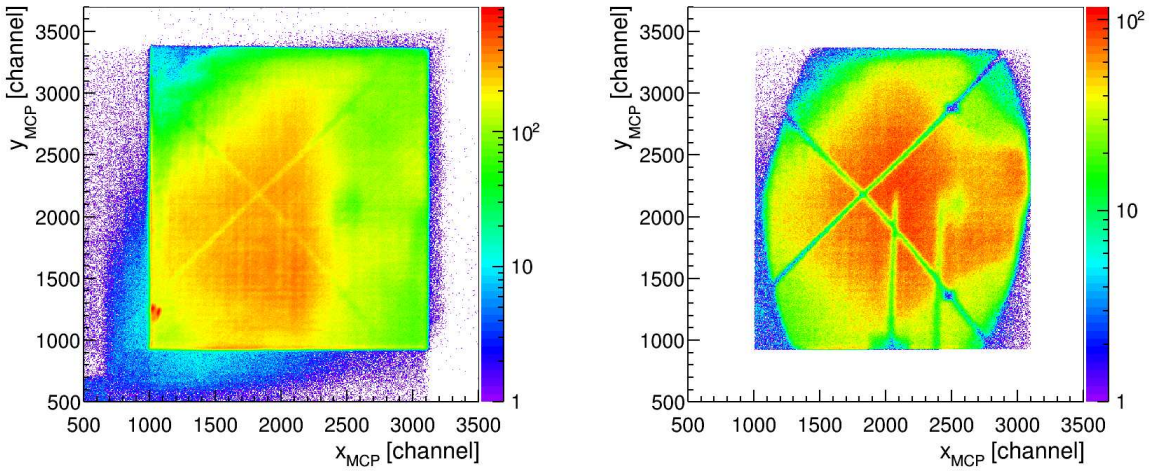

(A) Raw data. (B) Data in coincidence with the MWPPAC.

Figure 3.1: The x_{MCP} and y_{MCP} entrance positions measured with the MCP.

The cross visible in Fig. 3.1B is the projection of a mask placed about 1 cm downstream of the Carbon foil that is used for calibration of x_{MCP} and y_{MCP} positions. The metallic cross stops the ions and creates a shadow when the coincidence with the focal plane is required, and becomes very clear.

Figure 3.2A shows the MCP surface after the calibration of channels to millimetres. Spatial coordinates after calibration are used to find the exact direction of ions entering the

spectrometer. Conversion from spatial coordinates to angular ones can be easily calculated since the center of the cross matches the angle on which PRISMA was placed. All these informations allow to calculate the entrance angles (θ_{lab}, ϕ_{lab}) of the ions, shown in Fig. 3.2B, in the laboratory system. Angular acceptance is $\Delta\theta_{lab} = \pm 6°$ and $\Delta\phi_{lab} = \pm 11°$. The exact procedure of the transformation from the (x_{MCP}, y_{MCP}) to (θ_{lab}, ϕ_{lab}) is given in Ref. [72], Appendix A.1.2.

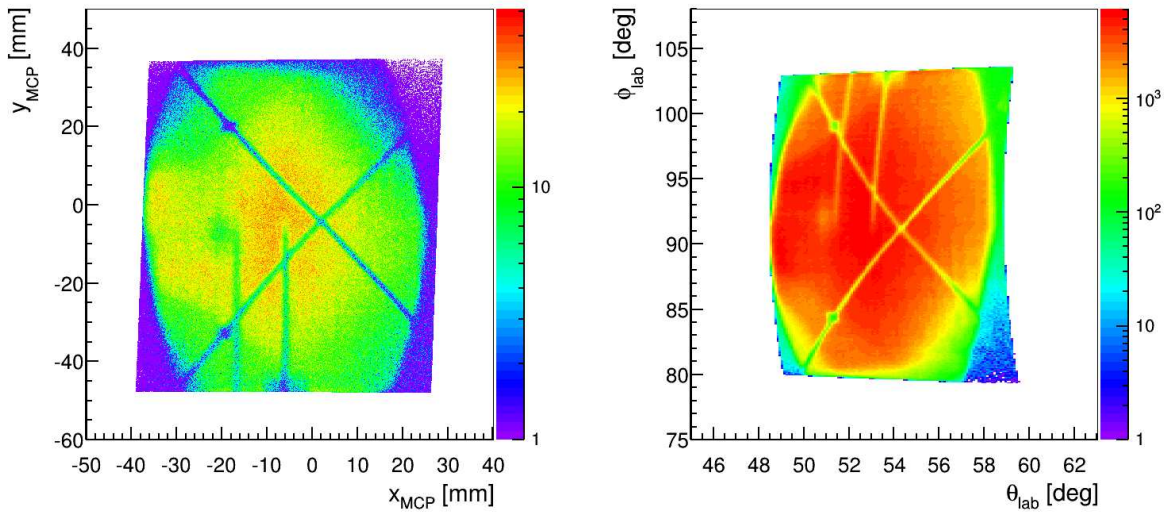

(A) The x_{MCP} and y_{MCP} position. (B) The θ_{lab} and ϕ_{lab} angles.

Figure 3.2: The calibrated position in millimetres and the entrance angles in cylindrical coordinates of the ions in the MCP.

MWPPAC position calibration

As already discussed, MWPPAC consist of 10 sections and each of them gives six raw signals:

- two signals for the horizontal position (*left* and *right*)
- two signals for the vertical position, common to all sections (*up* and *down*)
- one signal from the cathode
- one timing signal for the time of flight (TOF) construction.

For each section, position information is obtained from the difference between signals from the left and right side of the delay lines:

$$x_{PPAC} = right - left. \tag{3.1}$$

The position on the focal plane, x_{PPAC}, is then calibrated to millimetres and result is shown in Fig. 3.3. Peaks correspond to different atomic charge states of ^{40}Ar. To maximise the transport in the magnetic spectrometer, the magnetic fields have been set in order to have the most intense atomic charge state in the central position of the focal plane detector.

Vertical position is used to check the planarity of the ion trajectories, to assure the proper working of the quadrupole magnet and to check the quality of beam focusing on the target.

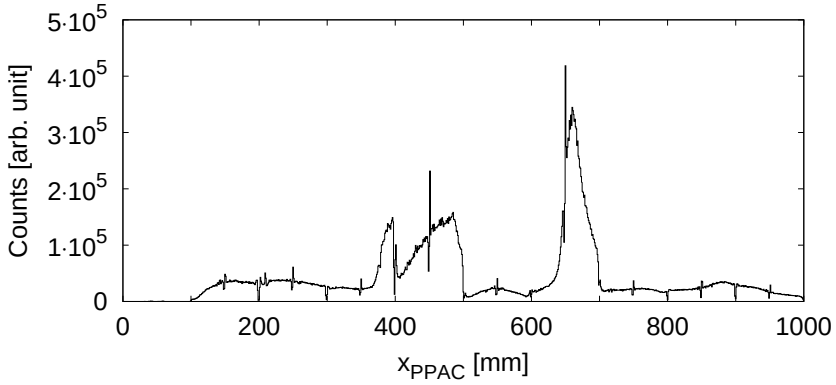

Figure 3.3: The calibrated focal plane position x_{PPAC}. Distributions correspond to different atomic charge states of ^{40}Ar, most intense ones are 16^+ and 17^+.

TOF calibration and alignment

TOF is measured between the MWPPAC cathode signals and the entrance detector time signal that is suitably delayed. First step is to calibrate TOF signals in nanoseconds and for this one applies off-line calibration coefficients. All ten sections then have to be aligned with respect to each other.

The crucial step is to define absolute (global) offset. This can be adjusted as a first step on the basis of TOF estimates and can be checked with the energy of the strong electromagnetic transitions, whose Doppler correction can be well tuned. By applying Doppler correction to the γ spectra one can check whether main lines have correct energy and width. This is an iterative procedure that ends when the proper offset of the TOF is found, i.e. when the main peaks have both the correct position in energy and width as small as possible. Final calibrated and projected (for all 10 sections) TOF spectrum is shown in Fig. 3.4B.

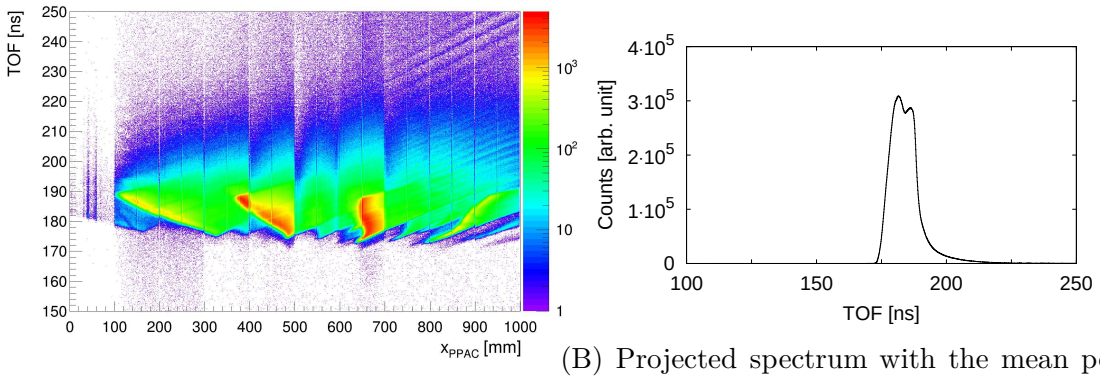

(A) Position on the focal plane versus calibrated and aligned TOF.

(B) Projected spectrum with the mean peak value at 184 ns.

Figure 3.4: Calibrated TOF spectrum.

The structures that are visible on Fig. 3.4A are related to different A/q ratios that are reaching the focal plane. Ions with higher magnetic rigidity $B\rho$ (higher momentum) will deflect less than ions with lower magnetic rigidity. This leads to the relation between $B\rho$ and the position on the focal plane: $B\rho \sim x_{PPAC}$. It is also related to the atomic charge states q. Different q will be deflected by magnetic fields to different positions on the focal plane, according to the inverse of q ($x_{PPAC} \sim 1/q$). That means that higher q are more deflected and they will appear on the right side of focal plane. Usually, in most experiments performed with PRISMA, intensity of magnetic fields is adjusted in such a way that most intense q is placed in the central part of the focal plane.

IC energy alignment

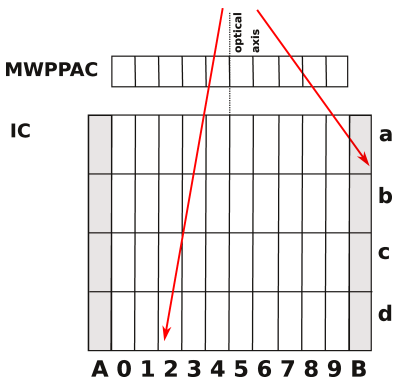

Figure 3.5: Trajectories in the IC, the ones ending in sections A and B are discarded.

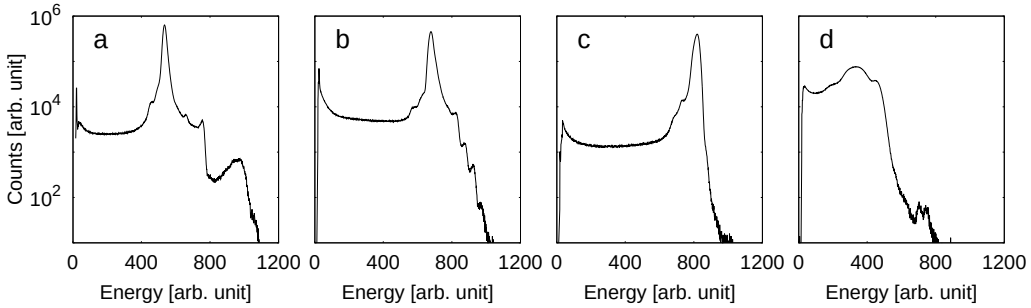

Figure 3.6: Energy deposited in all 4 sections in depth, a is the nearest one to the MWPPAC (see Fig. 3.5).

Anode in the IC is divided in 40 pads, 10 in the X axis correspond to the ones in the MWPPAC and each of them is divided in 4 sections in depth, as shown in Fig. 3.5. Each pad behaves as independent ΔE section. Figure 3.6 shows energy deposited in all 4 sections in depth for the ^{40}Ar+^{208}Pb reaction measured at 54°. The gas pressure is adjusted not only to stop ions, but to optimize the Z resolution. This is seen from the energy released in different sections where "c" is the location of the Bragg peak.

The alignment of the signals in each IC section is done through the off-line calibration by using a charge integration device and thus gain matching of different sections is obtained. In order to use total IC, resolution has to be preserved even after summation of different sections.

Gas pressure is adjusted in such a way that reaction products are fully stopped. The highly bent trajectories which cross the side sections (A and B columns in Fig. 3.5) are discarded since the total energy of these ions is not correctly measured.

3.2.2 Trajectory reconstruction

Identification of ions in atomic charge and mass is based on trajectory reconstruction which uses equations of motion in magnetic elements and informations measured with PRISMA (calibrated like presented in subsection 3.2.1). Trajectories are in the first approximation planar in the PRISMA plane (the xy plane in the PRISMA frame of reference in Fig. 3.7) and magnetic elements are considered to be ideal. In the Chapter 4 study of the PRISMA response function will be presented and this subject will be further discussed.

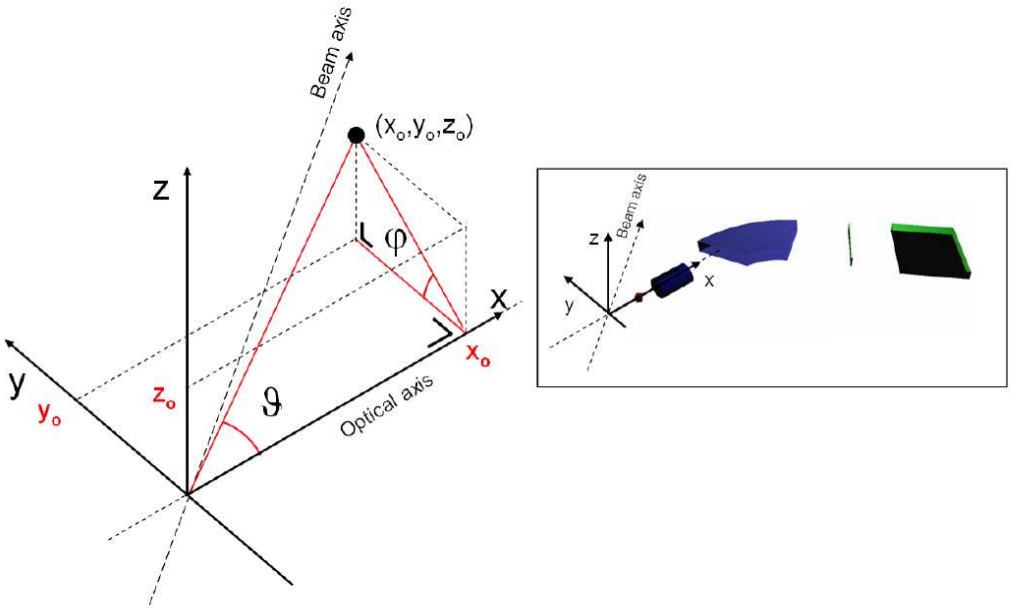

Figure 3.7: Frame of reference in the PRISMA system [72].

Motion of ions in magnetic fields

From the distances between different elements of the spectrometer and the knowledge of forces acting on ions inside magnets, equation of motion of ions can be found.

Motion in the quadrupole magnetic field. The entrance position in the quadrupole is completely determined by the coordinates of the nuclei given by the start detector. The quadrupole magnetic field is given by $\vec{B} = \vec{\nabla} U_m$, with $U_m = \frac{B_{max}}{\rho} yz$, and the force acting on a charged particle is obtained from the Lorentz equation $\vec{F} = q\vec{v} \times \vec{B}$. Resulting magnetic force on an ion moving in the quadrupole has two components: $F_x \simeq qv_z bx$ and $F_y \simeq -qv_z by$. The ion motion inside the quadrupole is a hyperbolic defocusing motion on the horizontal plane and sinusoidal focusing on the vertical plane whose main purpose is collection efficiency. Since the length of the quadrupole is known, it is possible to calculate the coordinates of the reaction products leaving the quadrupole. From the quadrupole to the dipole, as the magnetic fields are considered to be ideal, the trajectories follow a straight line [72].

Motion in the dipole magnetic field. Following the previous equation of motion in the quadrupole field, the entrance coordinates of the ions in the dipole can be found. The dipole magnetic field bends the trajectories because of the Lorentz force acting on a charged particle and motion becomes circular with a radius ρ. Since the radial velocity

of the ions is negligible, it's possible to consider v as the total velocity of the reaction products inside the dipole. An important quantity is the bending radius ρ, which can be written:

$$\rho = \frac{mv}{qB}. \tag{3.2}$$

A more usual quantity used to describe the motion of a charged particle in a dipole magnetic field is the magnetic rigidity:

$$B\rho = \frac{mv}{q}. \tag{3.3}$$

At the exit of the dipole, the ions are no more subjected to the magnetic force and their trajectories are considered to be straight lines up to the MWPPAC detector.

Ion trajectory reconstruction

Ion trajectory reconstruction takes input experimental parameters, then, event-by-event, calculates the trajectory of the ions up to the focal plane. Input parameters are entrance and focal plane positions, time of flight and energy losses in different sections of the IC. The parameters related to the spectrometer, such as its central angle and the magnetic field intensities, are set before starting the analysis.

By taking advantage of the very large longitudinal dimension of PRISMA (∼6 m) with respect to the transversal one (0.2 m) and considering that the fringing fields can be neglected because of the large dimensions of the magnetic elements, it may be assumed that the trajectories are planar after the quadrupole, i. e. all trajectories are in horizontal plane. The trajectories are uniquely determined by two parameters: the bending radius in the dipole and the ratio of the quadrupole and dipole magnetic fields. Because the magnetic fields are known, the bending radius ρ remains the only parameter to be searched for [73].

The procedure starts with the guess value $\rho = 120$ cm which corresponds to the central trajectory. If the calculated point in the focal plane lies within a millimetre from the experimentally measured point, the iteration ends, otherwise it continues with slightly different ρ. The tracking algorithm searches for parameters that match the experimental data, among all possible trajectories reaching the focal plane, in the position x_{PPAC}, y_{PPAC} with time of flight TOF. Results of trajectory reconstructions are the length of

the trajectories of the ions L and curvature radius ρ. In addition, by taking into account the energy loss in different sections of the IC, the range of ions in the IC, R, and the total energy, E via TOF, can be compared with the total energy measured.

Total path length L of ions in the magnetic spectrometer is obtained by summing different paths:

$$L = L_{MCP} + L_Q + L_{Q-D} + L_D + L_{PPAC} \tag{3.4}$$

where:

- L_{MCP} is a straight line from the target to the quadrupole entrance
- L_Q is a hyperbolic path inside the quadrupole magnet
- L_{Q-D} is a straight line between the quadrupole and the dipole entrance
- L_D is a circular trajectory in the dipole magnet in the horizontal dispersion plane
- L_{PPAC} is a straight line in the dispersion plane from the exit of the dipole up to the focal plane.

The reconstruction of the range of ions R in the IC is performed only after the reconstruction of the trajectory in PRISMA is completed. Since the IC is segmented, the treatment is the following:

- all the events with the path in the IC not compatible with the reconstructed trajectory in PRISMA are rejected by looking at the sections that fired
- the total energy E is obtained by summing energy losses ΔE_i of each of the sections $E = \sum_{i=0}^{9} \Delta E_i$
- a weighted distance L_w between MWPPAC and each IC section is constructed by using the ΔE_i as weight. An estimate of the range R of the ions is obtained from the weighted distance by subtracting the MWPPAC-IC distance, $L_{PPAC-IC}$:

$$R = L_w - L_{PPAC-IC} = \frac{\sum_i L_i \Delta E_i}{E} - L_{PPAC-IC}. \tag{3.5}$$

3.2.3 Ion identification

Identification of nuclear charge Z

The identification of nuclear charge Z is obtained through the measurement of energy loss ΔE in the IC, which also provides the total energy E. IC operates in proportional regime where the integrated charge is proportional to energy loss. The rate of energy loss

of a charged particle passing through a medium is described by the Bethe-Bloch formula:

$$-\frac{dE}{dx} = 2\pi N_a r_e^2 m_e c^2 \rho \frac{Z}{A}\frac{z^2}{\beta^2}\left[ln(\frac{2m_e\gamma^2 v^2 W_{max}}{I^2} - 2\beta^2)\right] \tag{3.6}$$

with r_e classical electron radius ($2.817 \cdot 10^{-13}$ cm), m_e electron mass ($9.11 \cdot 10^{-31}$ kg), N_a Avogadro's number ($6.022 \cdot 10^{23}$ 1/mol), I mean excitation potential, Z nuclear charge of absorbing material, A relative atomic mass of absorbing material, ρ density of absorbing material, z charge of incident particle in units of e, $\beta = v/c$ velocity of the incident particle, $\gamma = 1/\sqrt{1-\beta^2}$ and W_{max} maximum energy transfer in a single collision. Formula can be approximated for the non-relativistic particles and for the same absorbing material:

$$\frac{dE}{dx} \sim \frac{MZ_{eff}^2}{E} \tag{3.7}$$

where M is atomic mass, Z_{eff} effective nuclear charge of an ion and E energy. ΔE, E and R obtained with PRISMA correspond to dE, E and dx in Bethe-Bloch equations.

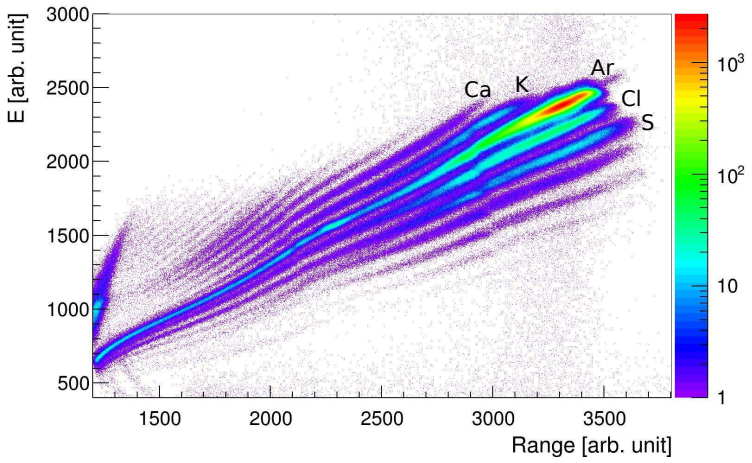

Figure 3.8: The matrix of range versus energy which is used for the Z identification. Figure shows this matrix for ^{40}Ar+^{208}Pb reaction at E_{lab} = 260 MeV at 54°. The most intense line corresponds to the Ar ions scattered by the target. Proton pick-up and stripping channels are seen above and below, respectively, from $(+4p)$ Ti to $(-6p)$ Mg.

Ions reach the IC with a broad range of kinetic energies and directions. To get the desired Z resolution for all reaction products reaching the IC, one has to properly take into account the direction followed by the different ions. One can estimate the path (range) from the signal of each subsection and the position information as explained in the subsection 3.2.2. Since range is result of trajectory reconstruction obtained by taking

into account the direction of ions, we decided to present range versus energy matrix in Fig. 3.8. Generally with this matrix the bent ("tilted") trajectories are better recovered. Separation between different Z is clearly visible. The most intense line corresponds to the Ar ions (with the highest cross section of the ^{40}Ar elastically scattered). The other isotopic chains are identified according to the Bethe-Bloch equation. For a fixed total energy E, the atomic number increases with ΔE, while it decreases with R, thus proton pick-up and stripping channels appear above and below the Ar line, respectively.

Identification of atomic charge states q

The individual atomic charge states can be separated in the two dimensional matrix $\rho\beta$ versus energy E. By combining different relations one can identify atomic charge states. By taking into account influence of Lorenz force on the ion trajectory, that is, magnetic rigidity $B\rho$:

$$\frac{Av^2}{\rho} = qvB \tag{3.8}$$

$$B\rho = \frac{p}{q} = \frac{Av}{q} \tag{3.9}$$

and expression for kinetic energy of ion:

$$E = \frac{1}{2}Av^2 \tag{3.10}$$

one gets:

$$q = \frac{2}{B}\frac{E}{v\rho}. \tag{3.11}$$

In fact, by taking into account Eq. 3.11, the different distributions seen in Fig. 3.9 are associated to different charge states, which can then be selected by specific gates. Value of charge states increases with E for a fixed $\rho\beta$. Both, curvature radius and velocity (obtained from the ratio of length and TOF), are reconstructed event-by-event to account for optical aberrations.

The atomic charge states are identified by comparison with the calculated charge state distribution. The average equilibrium charge state distribution of heavy ions for a beam of ions of nuclear charge Z and energy E expressed in MeV and atomic mass A according

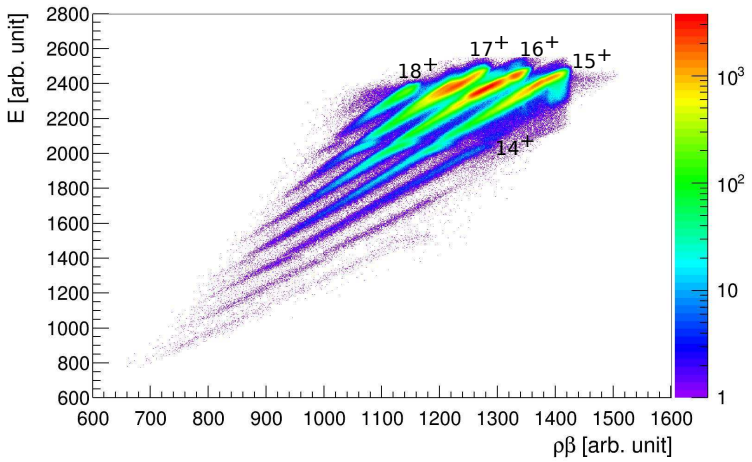

Figure 3.9: $\rho\beta$ versus energy matrix used to identify different atomic charge states for the Ar ions. In the studied reaction most intense charge state was 16^+.

to Shima [75] is following empirical formula:

$$q/Z_1 = \left[1 - e^{-1.25X + 0.32X^2 - 0.11X^3}\right]\left[1 - 0.0019(Z_2 - 6)\sqrt{X} + 0.00001(Z_2 - 6)^2 X\right] \quad (3.12)$$

where Z_1 and Z_2 are the ion and target foil atomic numbers, while X is the reduced ion velocity equal to $X = v/(v' \cdot Z_1^n) = v/[3.6 \times 10^8 (\mathrm{cm/s}) \mathrm{Z}_1^{0.45}]$. The distribution of charge states is given in Table 3.2. The good agreement between calculated and theoretical distribution for the ^{40}Ar ions is represented in Fig. 3.10.

Table 3.2: Charge state distribution for ^{40}Ar calculated according to Eq. 3.12.

q	14	15	16	17	18
%	3.9	19.8	41.1	29.2	5.6

From Lorenz force (Eq. 3.8) we obtain the quantity $B\rho TOF/L$ which is proportional to the ratio A/q. Since velocity of ions is around $v/c = 10\%$, by taking into account relativistic formula $TOF = TOF\sqrt{1-\beta^2}$ one obtains:

$$\frac{A}{q} = B\rho \frac{TOF\sqrt{1-\beta^2}}{L}. \quad (3.13)$$

By plotting this quantity as a function of the x_{PPAC} position, as shown in Fig. 3.11A for Ar ($Z = 18$), a clear discrimination with characteristic repetitive pattern of the different

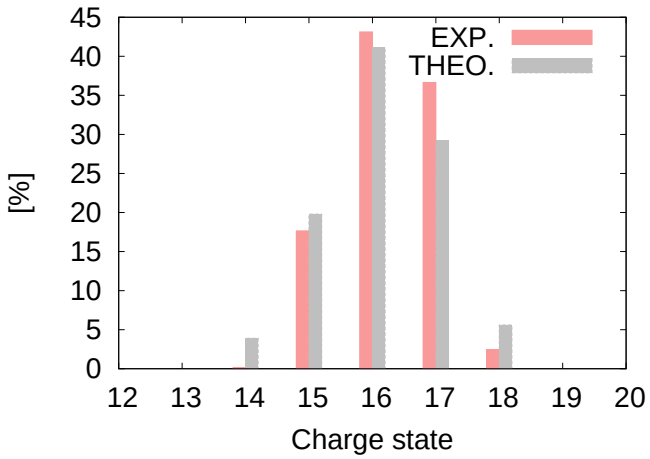

Figure 3.10: The experimental (red) and calculated (grey) atomic charge state distribution for the ^{40}Ar ions.

A/q is obtained. The large acceptance of the spectrometer is reflected in the fact that different atomic charge states cover several sections in the focal plane, which are all joined together in the figure.

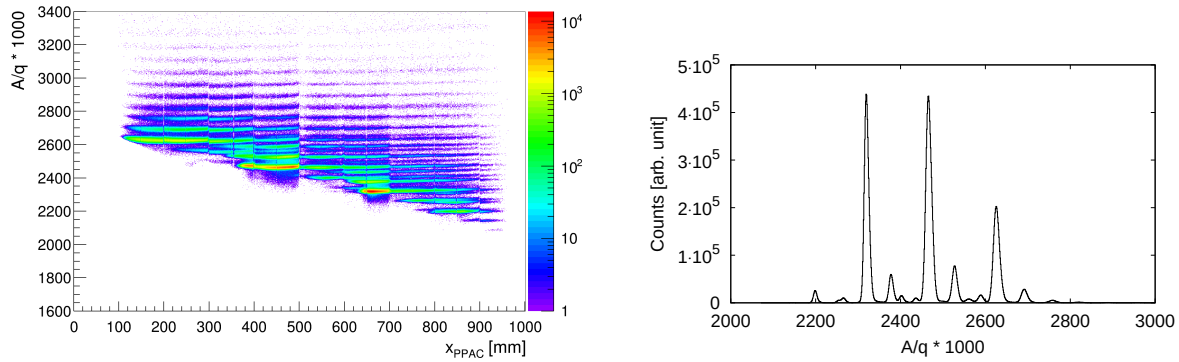

(A) The x_{PPAC} position on the focal plane versus A/q.

(B) Projected A/q spectrum.

Figure 3.11: A/q for the Ar isotopes.

Selection (extraction) of charge states depends strongly on the energy resolution of the IC, which is more critical for heavy ions and low kinetic energies. Without the unambiguous identification of q, spurious mass peaks are produced which contribute to the background in the mass spectra. The good identification of atomic charge states in the present case resulted in clear mass spectra.

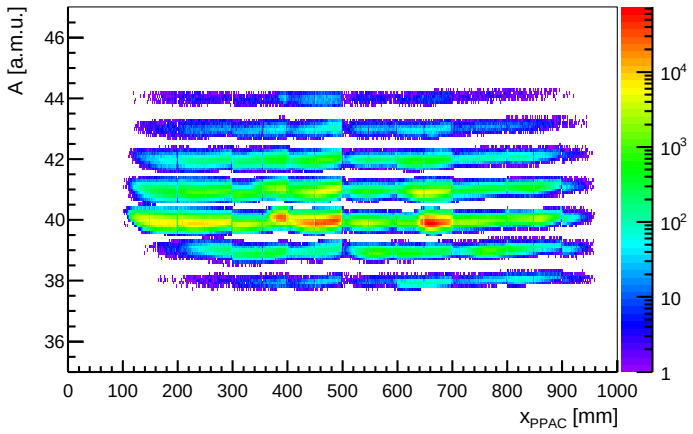

Figure 3.12: Masses versus the focal plane position for the Ar isotopes.

Reconstruction of the mass A

After the identification in atomic number Z and atomic charge state q, mass numbers can be assigned by multiplying A/q values with q ($A = qB\rho/v$). This procedure is then repeated for every atomic number. The example shown in Fig. 3.12 for the Ar isotopes demonstrates background clear spectra and good resolution achieved.

To assure the exact mass numbers in atomic mass units, one has to check A/q ratio. For example, for the most intense mass, ^{40}Ar, with q calculated as in Table 3.2, the experimental value A/q has to match the calculated one, thus A/q axis has to be recalibrated until exact value is obtained. Any error in the q assignment would produce a strong shift in a mass spectra that can be easily noticed.

Final mass spectra for observed isotopes are plotted separately for all three measured angles in Fig. 3.13. A resolution of $\Delta A/A \approx 150$ for every Z has been reached. Also, not only proton stripping but also proton pick-up channels are visible.

3.2.4 The CLARA data analysis

Each of 25 Ge clover detectors of the CLARA array gives following signals:

- energy deposited in each of the four crystals (on 4 and 20 MeV scale)
- time signals for each of the four crystals
- total energy deposited in BGO shield.

In the ^{40}Ar+^{208}Pb experiment 22 clovers were active.

After the alignment of energy and time signals, the energy signals were calibrated crystal by crystal with ^{152}Eu radioactive source. Linear calibration curve relating energy

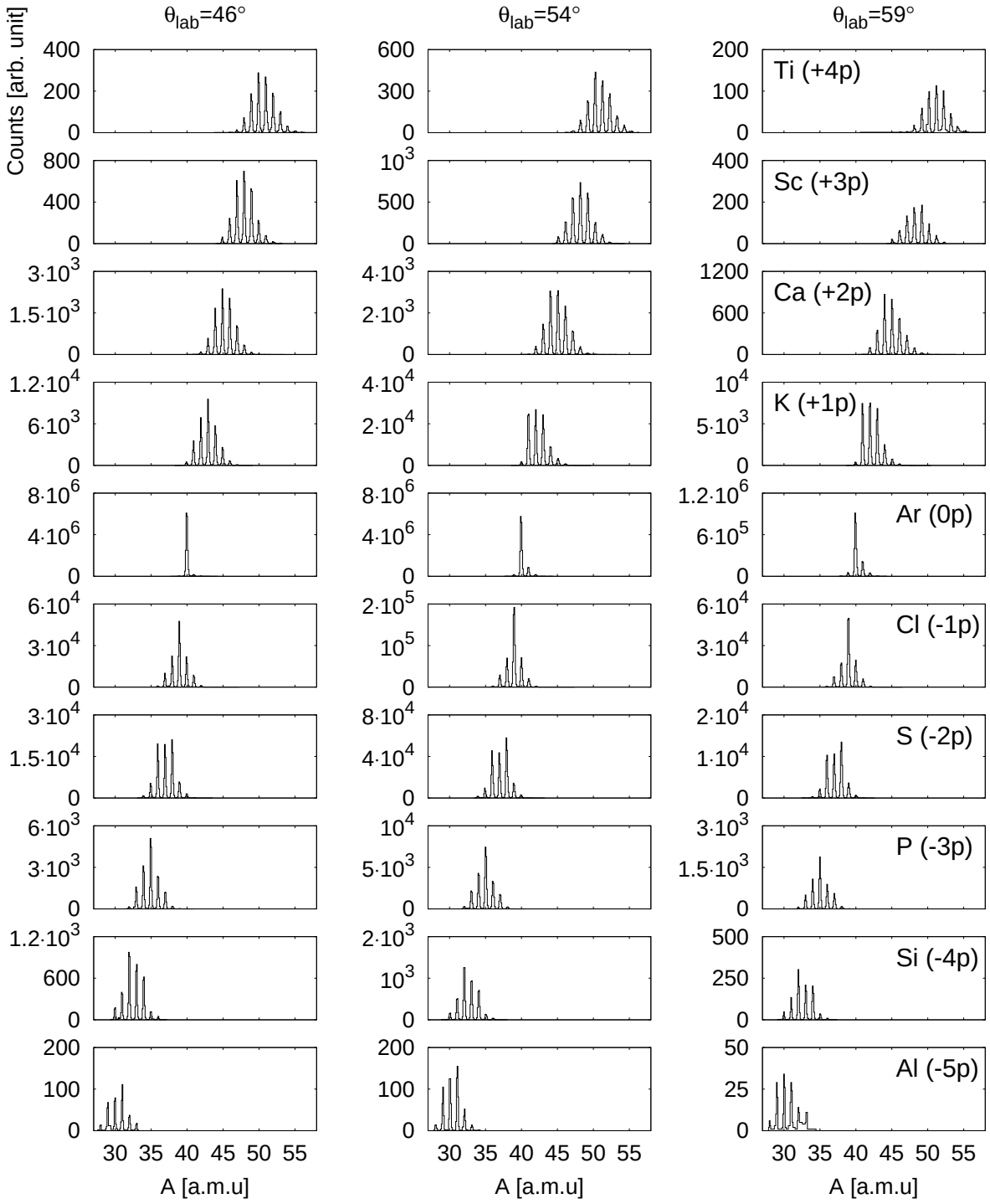

Figure 3.13: Mass spectra for three measured angles. Channels from $(+4p)$ to $(-5p)$ have been identified.

to channel number is derived for all crystals being the degree of non-linearity quite small. Figure 3.14 shows γ spectrum of ^{152}Eu source obtained as a sum of all calibrated Ge crystals.

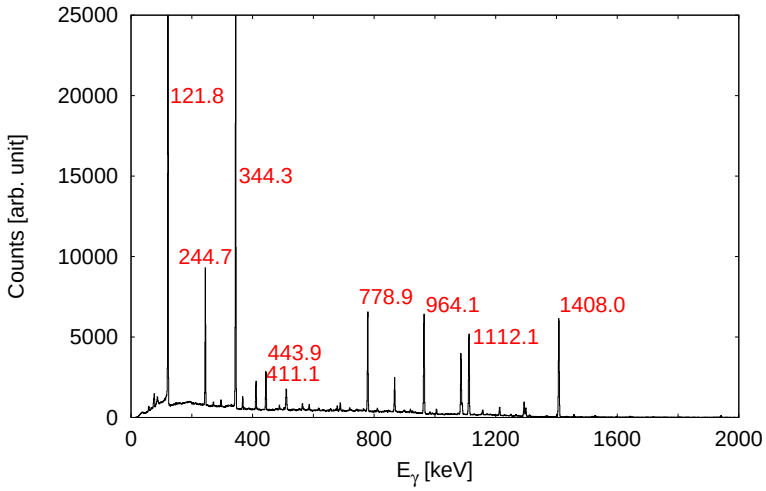

Figure 3.14: The γ spectrum of the ^{152}Eu radioactive source obtained as a sum of all calibrated Ge crystals.

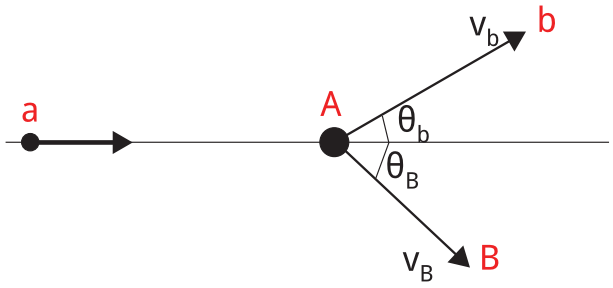

Figure 3.15: Scheme of a nuclear collision $a + A \longrightarrow b + B$.

While γ transitions from radioactive sources are emitted in rest, those from reaction products are emitted while they are moving. Energy of emitted radiation is due to Doppler effect shifted as compared to the real, tabulated value and needs to be corrected. Non-relativistic relation connecting the real energy $E_{\gamma 0}$ and detected one E_γ is:

$$E_\gamma = E_{\gamma 0}\left(1 + \frac{v_b}{c} cos\theta\right) \tag{3.14}$$

where θ is the angle formed by the velocity vector v_b of the nucleus and axis of the detector. Difference between $E_{\gamma 0}$ and E_γ has its maximum at 0° and minimum at 180°.

The direction of the moving ion and its velocity is measured with PRISMA. Angular position of each Ge detector in the CLARA array is known (see Table B.1 in Apendix B). With this it is possible to make event-by-event Doppler shift correction of γ rays emitted by the projectile-like products that are identified in PRISMA.

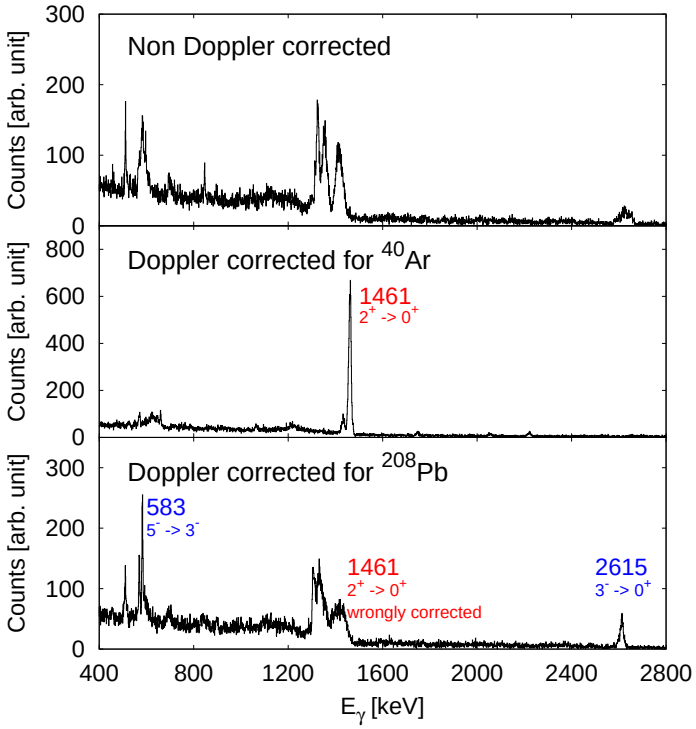

Figure 3.16: Gamma spectrum for ^{40}Ar without any Doppler correction and the same spectrum Doppler corrected for ^{40}Ar and ^{208}Pb.

Assuming a binary collision between a projectile a impinging on a target nucleus A at rest, $a + A \longrightarrow b + B$, absolute velocity and direction of partner-like ions B, v_B and θ_B in Fig. 3.15, can be identified from laws of conservations and kinematics. In this case v_B and θ_B of the binary partner can be calculated and applied for Doppler correction of γ rays of heavy (not detected) partner on event-by-event basis. Average velocity in this reaction for the projectile-like nuclei is $v/c = 10\%$ and for the partner-like is $v/c = 2\%$.

Figure 3.16 shows γ spectrum detected in coincidence with ^{40}Ar without any Doppler correction and the same spectrum Doppler corrected for ^{40}Ar and ^{208}Pb. Only after Doppler correction has been applied $2^+ \rightarrow 0^+$ transition in ^{40}Ar can be recognized. In that panel broad peaks correspond to ^{208}Pb not Doppler corrected.

Dominant characteristic of HPGe detectors is their excellent energy resolution. Resolution is normally determined by three factors: the inherent statistical spread in the number of charge carriers, variations in the charge collection efficiency and contribution of electronic noise [76]. Which of these factors dominate depends on the radiation and the size and quality of detector. Resolution obtained for the CLARA array with the ^{152}Eu radioactive source as a function of energy, together with the resolution of the most in-

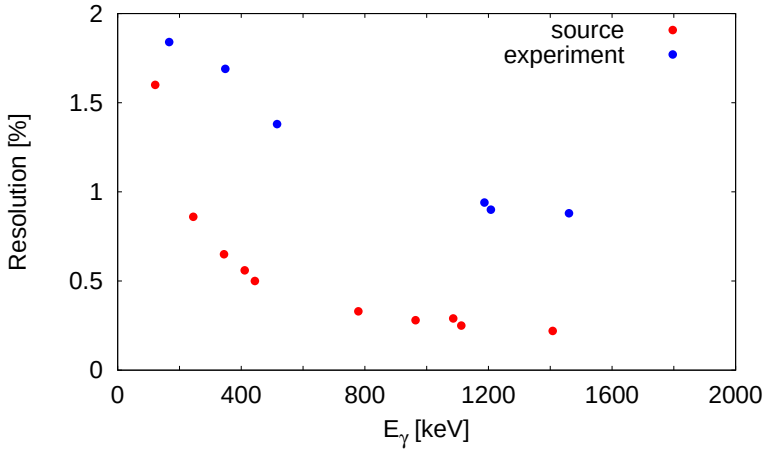

Figure 3.17: Resolution obtained for the CLARA array with the ^{152}Eu radioactive source (red points) and most intense γ rays from the Ar isotopes (blue points).

tense γ rays from the Ar isotopes, is given in Fig. 3.17. The width of the peaks generally worsens when one applies Doppler corrections and sums over many Ge detectors, taking into account the Doppler broadening due to the finite opening angle of detectors.

Coincidence requirement with PRISMA and background reduction

By selecting a specific nucleus in PRISMA, the γ spectrum belonging to that particular channel is obtained. Random coincidences can be reduced by time of flight coincidence requirements. Figure 3.18 shows the coincidence time spectrum between PRISMA and CLARA. Background that is seen belongs to random events recorded in CLARA. By selecting only events in the peak, the level of background can be significantly lowered as demonstrated in Fig. 3.19.

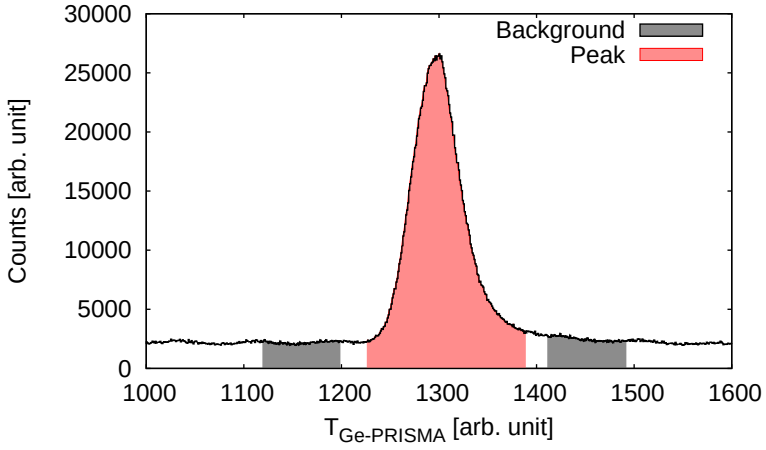

Figure 3.18: Ge-PRISMA coincidence time spectrum for $\theta_{PRISMA} = 54°$.

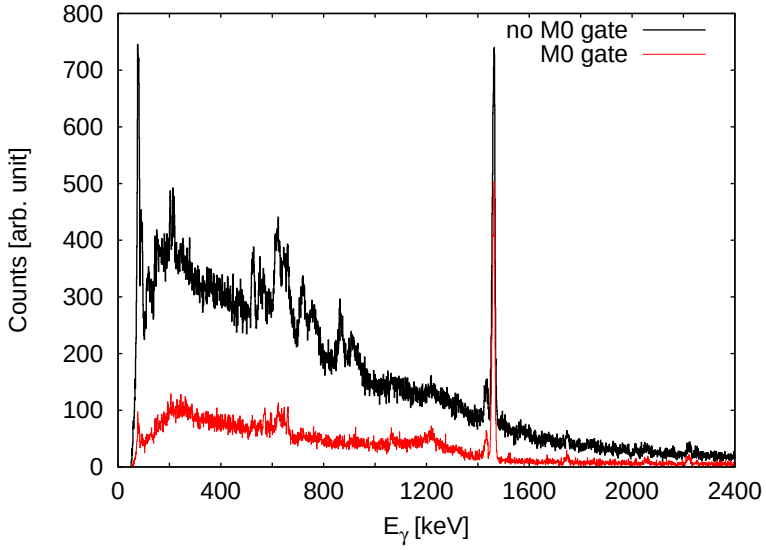

Figure 3.19: Reduction of background with condition on the Ge-PRISMA coincidence time spectrum (M0 gate corresponds to red surface in Fig. 3.18). ^{40}Ar γ spectrum without (black) and with (red) condition on.

Ge detectors of CLARA are surrounded by BGO scintillators large enough to intercept most of the photons escaping from Ge detector and with a good efficiency for their detection. In this way all events that release part of the energy in BGO are rejected.

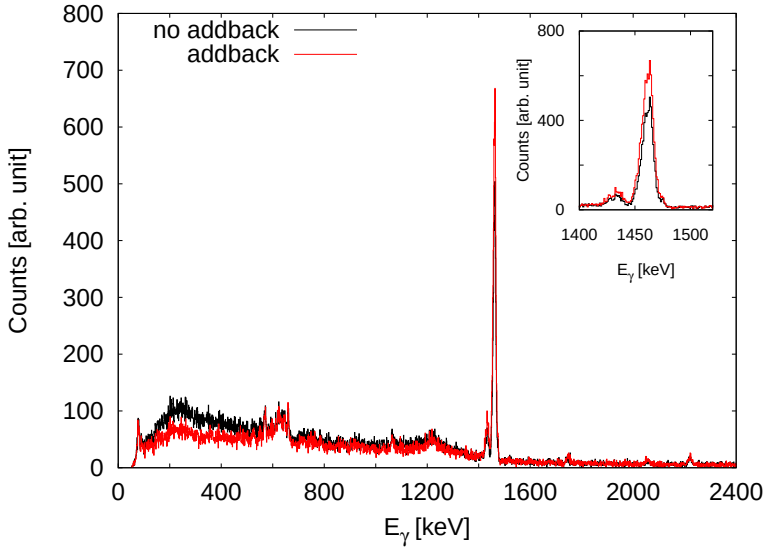

Figure 3.20: The γ spectrum for ^{40}Ar considering the contribution from each crystal separately (black line) and in add-back mode (red line). Add-back procedure further lowers background contribution and increases photopeak intensity.

In the clover detectors the energy signals from 4 crystals are acquired independently, and since one γ ray can interact with more than one crystal, add-back algorithms are used to determine the γ-ray energy. This also improves the efficiency for relatively high energies.

The effect of the add-back method can be seen in Fig. 3.20. This method improves the photopeak efficiency and helps in reducing background from Compton scattering.

CLARA efficiency

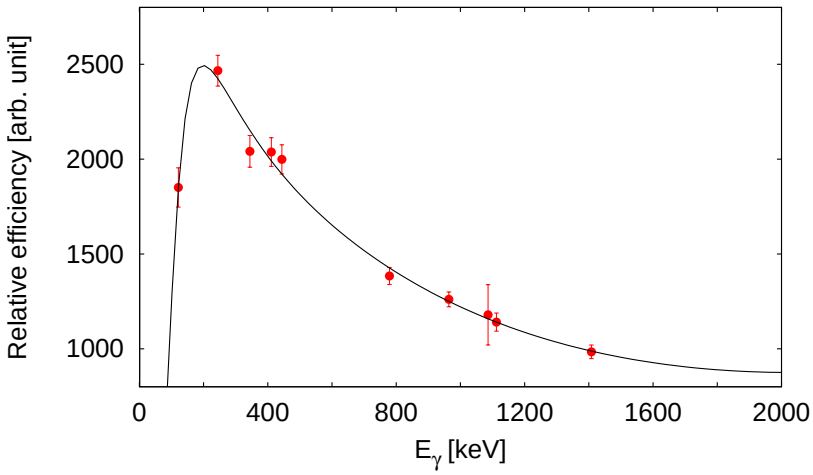

Figure 3.21: The relative efficiency of the CLARA array (red dots). Add-back procedure has been previously applied. Experimental data have been fitted with the expression $\epsilon = exp(-714.9 + 573.9ln(x) - 182.0(ln(x))^2 + 28.8(ln(x))^3 - 2.3(ln(x))^4 + 0.072(ln(x))^5)$ and result is presented with black line.

Measurement of absolute intensity of γ rays requires knowledge of the detection efficiency. Detection efficiency is defined as the ratio K/N between the number K of detected photons over the number N of emitted photons. Again the ^{152}Eu source has been used to construct an empirical efficiency versus energy curve as in Fig. 3.21.

4 Study of the transmission of the PRISMA spectrometer

The understanding of the reaction mechanism depends strongly on the determination of the absolute cross sections. This implies understanding of the ion transmission which for large solid angle spectrometers depends in a complex way on the entrance positions and momenta of the reaction products. Therefore, to determine the transmission one needs a Monte Carlo simulation of ion trajectories, where the kinematics of the reaction and the geometry of the magnetic elements and detectors are taken into account. In this Chapter a study of the response function of the large acceptance magnetic spectrometer PRISMA for transport of ions detected in the ^{40}Ar+^{208}Pb reaction is presented.

4.1 The response function of the PRISMA spectrometer

The aim of the transport study in PRISMA is to find a response function which allows to correct the angular distributions, and subsequently the total cross sections, from biases or cuts arising from ion transport effects. The study is performed in several steps:

- creating a uniform distribution of input events
- tuning of the magnetic fields
- transport of the uniform input distribution event-by-event
- definition of the response function.

4.1.1 Monte Carlo simulation code

The response function study is based on a Monte Carlo simulation code. The ion positions at the focal plane and their trajectories are calculated event-by-event on the basis of

detailed knowledge of magnetic (with fringing) fields, together with geometry of detectors. The energy losses in the different mylar windows of the MWPPAC and IC detectors of PRISMA are taken into account and the energy loss in the IC is treated in the conventional approximation of the motion of a charged particle in a gas.

The Monte Carlo method is a numerical technique for calculating probabilities and related quantities by using sequences of random numbers [77]. As a first step one uses event generator program that generates values of the velocity and energy of particles. The output of the event generator, i.e. velocity vectors and energy of the generated particles, is then used as an input for a detector simulation program.

The procedure employs a ray-tracing code, which uses numerical integrators to determine the trajectories of individual rays through the electromagnetic fields, the latter are being calculated by means of the Finite Element Method. For this reason, the reliability of the simulation depends on a correct calculation of the magnetic fields and corresponding fringing fields [72, 78]. Finally, a data file containing all the parameters measured with PRISMA is produced with a simulation code and the file can be analysed with the same code used to analyse experimental data.

4.1.2 Magnetic fields

Ion identification in the PRISMA spectrometer is based on ion trajectory reconstruction procedure that is using informations measured with refined detectors which, besides energy loss and timing, give necessary position information along ion trajectory. As the reconstruction relies on precise determination of the magnetic and fringing fields, the tuning of the magnetic fields used in the simulation procedure is a crucial point in the response function study. Thus, the first step is to calculate magnetic fields and to estimate the force that acts on the ion that is moving through the spectrometer. To adjust the value of the magnetic fields, a simple procedure has been used, based on the assumption that, under the same physical conditions, the charge state deflection is the same in simulation and in the experiment.

The tuning of the magnetic fields needs to proceed in two steps, one magnet (i.e. quadrupole or dipole) at a time. First a small number of events following isotropic distribution is created with fixed kinetic energy. The same ion with the same kinetic energy is also considered in the experiment, so a direct comparison of the two distributions can

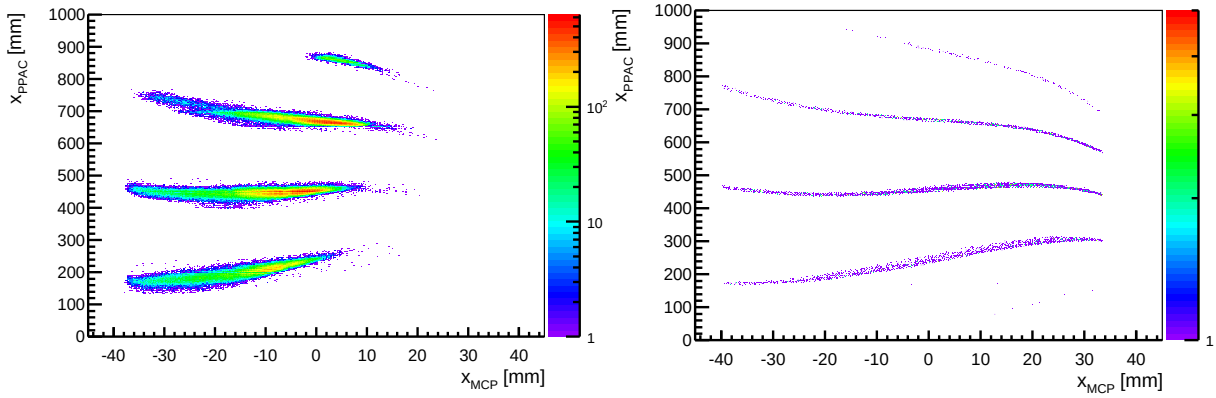

(A) Experimental distribution.

(B) Simulated distribution.

Figure 4.1: Charge state distributions of ^{40}Ar with E_{kin} = 222 MeV as a function of positions at x_{MCP} and x_{PPAC}.

be made at the focal plane. This comparison is illustrated in Fig. 4.1A (experimental charge state distribution) and Fig. 4.1B (simulated one) for ^{40}Ar with fixed kinetic energy as a function of the horizontal coordinates x_{MCP} and x_{PPAC}. The quadrupole field vanishes along the optical axis of PRISMA, so by comparing projections of the simulated and experimental distributions around $x_{MCP} = 0$ mm, one focuses on the dipole field effects only. It is found that small adjustment of the dipole field, of the order of 3% with respect to the set value, is needed to match the simulated charge state distribution with the experimental one (see Fig. 4.2A for ^{40}Ar and Fig. 4.2B for ^{41}Ar).

The same procedure is then applied outside optical axis in order to tune the value of the quadrupole field (see Figs. 4.3A and 4.3B). However, adjustment of the order of 10% is needed to match the experimental distribution. This is due to a combined effect of not optimal calibration between the values of the currents and the magnetic quadrupole field, and a rather schematic reconstruction of the trajectory in the spectrometer [72]. Final values of dipole and quadrupole fields used in the simulation are listed in Table 4.1.

Table 4.1: The experimentally set and simulated values of the dipole and quadrupole magnetic fields.

^{40}Ar+^{208}Pb	DIPOLE			QUADRUPOLE		
Angle	B_{set}	B_{sim}	$(\Delta B)/B_{set}$ [%]	B_{set}	B_{sim}	$(\Delta B)/B_{set}$ [%]
46°	636700	655000	2.9	561800	505600	-10.0
54°	619900	642000	3.6	546969	497000	-9.1
59°	612800	636000	3.8	540700	488000	-9.7

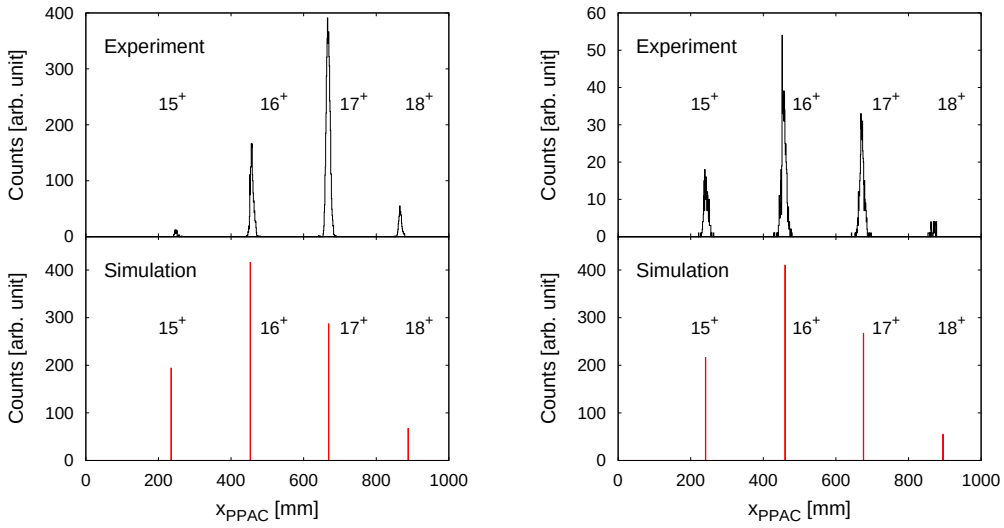

(A) ^{40}Ar. (B) ^{41}Ar.

Figure 4.2: The comparison of dipole fields along optical axis. Top panels display the experimental projection of charge states on the focal plane, while the bottom panels show the same projection in the case of simulated events. A good agreement is obtained in the position of the dominant atomic charge states in the focal plane, as well as in their relative strength, especially for ^{41}Ar.

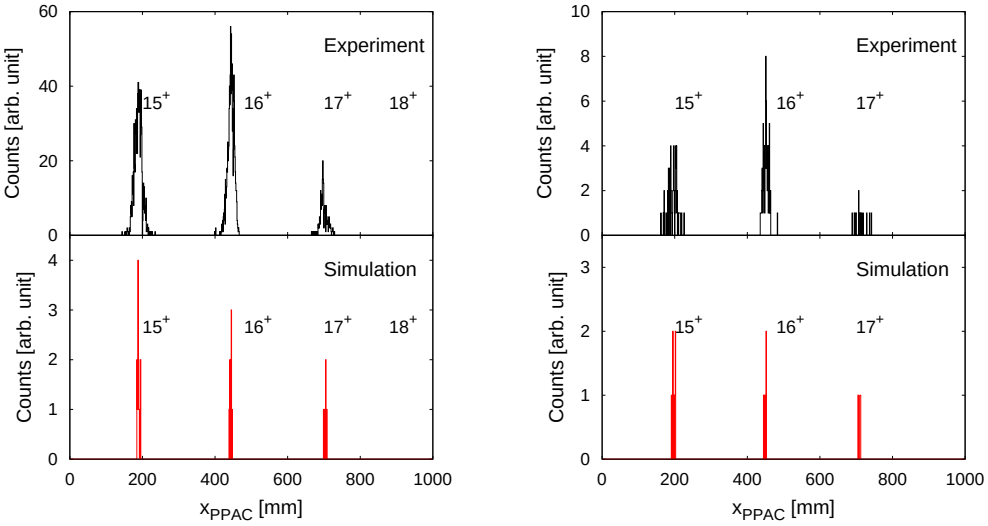

(A) ^{40}Ar at E_{kin} = 222 MeV. (B) ^{41}Ar at E_{kin} = 222 MeV.

Figure 4.3: The comparison of the quadrupole field strengths, where the trajectory outside optical axis is chosen. See Fig. 4.2 for more details.

4.1.3 The transport of the uniform distribution

After magnetic fields have been tuned to match the experimental conditions, two million events of ^{40}Ar ions have been randomly generated with uniform kinetic energy distribution and isotropic angular distribution, from a point-like source placed at the target position

in the laboratory frame. The kinetic energy E_{kin} has been varied in the interval 100 - 250 MeV, corresponding to the momentum acceptance of the spectrometer for ^{40}Ar ions. Events have been generated with spherical geometry, with the angular range slightly larger than the acceptance of the PRISMA spectrometer, which is defined by the entrance area of the quadrupole magnet. θ_{lab} and ϕ_{lab} are the azimuthal and polar angle in the laboratory frame with respect to the beam axis. To remind, PRISMA has geometrical acceptance of $\theta_{lab} = \pm 6^{\circ}$ and $\phi_{lab} = \pm 11^{\circ}$. At the entrance of quadrupole, the ions follow the charge states distribution according to the semi-empirical formula of Shima (Eq. 3.12) [75]. This distribution is then transported by the ray-tracing code up to the focal plane of the spectrometer.

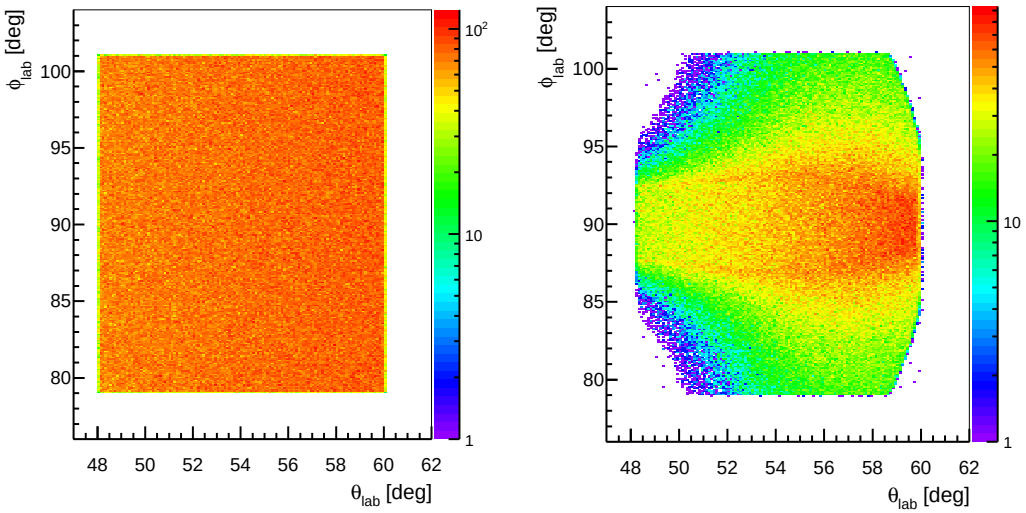

(A) Before transport.

(B) After transport.

Figure 4.4: The ^{40}Ar distribution in θ_{lab} and ϕ_{lab} of events before and after the transport through PRISMA. Input distribution consists of two million events with kinetic energy between 100 and 250 MeV. For comparison see the experimental matrix in Chapter 3, Fig. 3.2B.

Figure 4.4A shows incoming distribution of ions on the MCP detector, while Fig. 4.4B represents the same distribution after the transport to the focal plane. It is clearly visible that the spectrometer mostly affects the transport at the border of the acceptance region. It is important to notice how the distributions are symmetric in ϕ_{lab}. Also, it can be noticed that the active area of the MCP detector is larger than the acceptance of the spectrometer, i.e. the quadrupole entrance window. Due to this, a number of ions reaching the focal plane is less than half of the incident ions. This once again points to the importance of the precise determination of the response function of the spectrometer in order to have correct estimate of both the absolute number of events and the angular

distribution of every reaction channel under study.

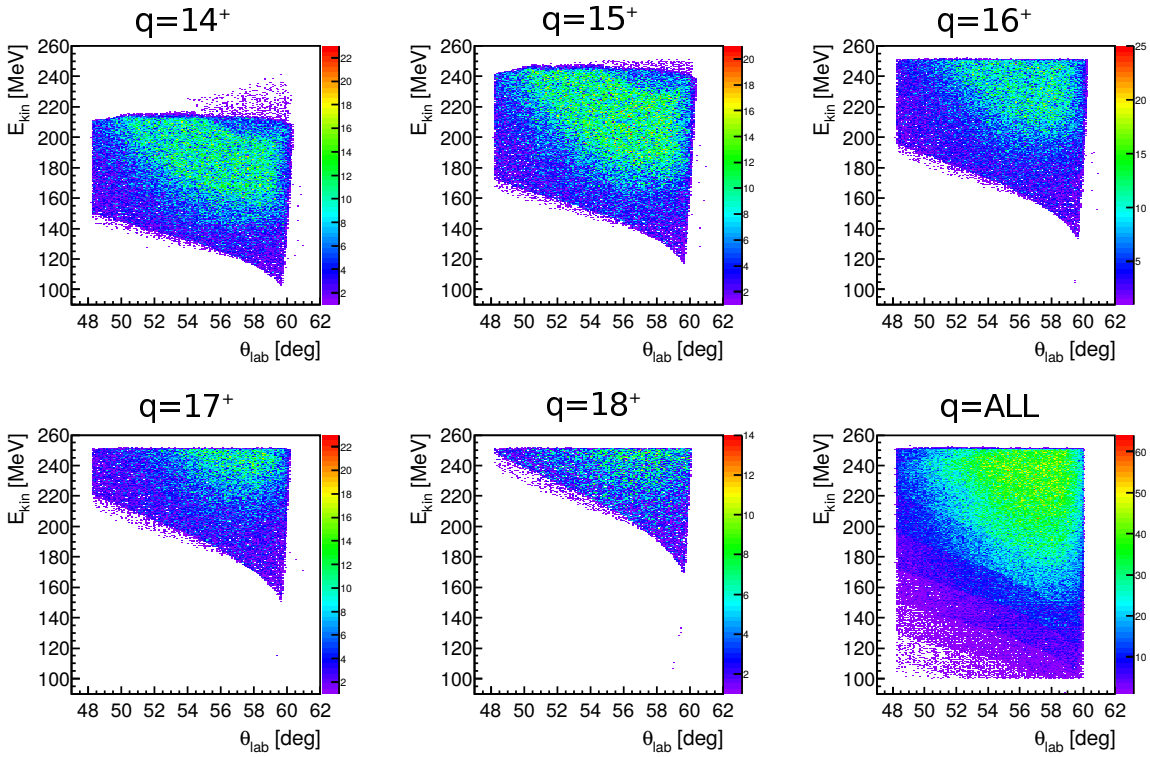

Figure 4.5: Transported kinetic energy E_{kin} as the function of dispersion angle θ_{lab} for different charge states labelled in panels for ^{40}Ar ions.

The study of the transport of the specific charge states can provide further informations about the response of the spectrometer. Figure 4.5 shows transported kinetic energy E_{kin} as a function of dispersion angle θ_{lab} for different atomic charge states of ^{40}Ar ions. For each charge state a non uniform distribution is obtained at the focal plane. The upper cut is due to the momentum acceptance of the spectrometer which defines the maximum values of the transported kinetic energies, while the lower diagonal cut is related to the minimum momentum acceptance. This minimum value depends on dispersion angle θ_{lab} which may be connected with the transport of different energies (momenta) in dipole.

Figure 4.6 shows angular distributions after transport through PRISMA for different charge states, while Fig. 4.7 for different kinetic energies for the charge state 17^+. A strong dependence on the kinetic energy (momentum) of the incident ions and on charge states is clearly visible.

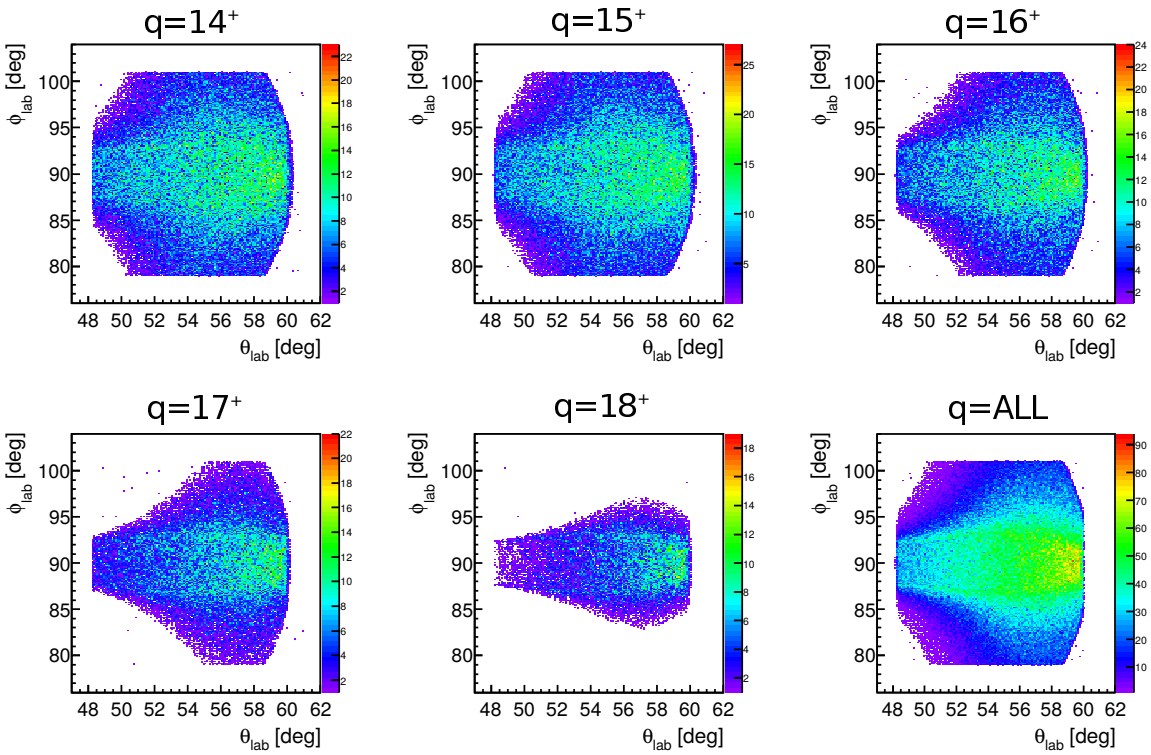

Figure 4.6: Transported $\theta_{lab} - \phi_{lab}$ matrices for different atomic charge states.

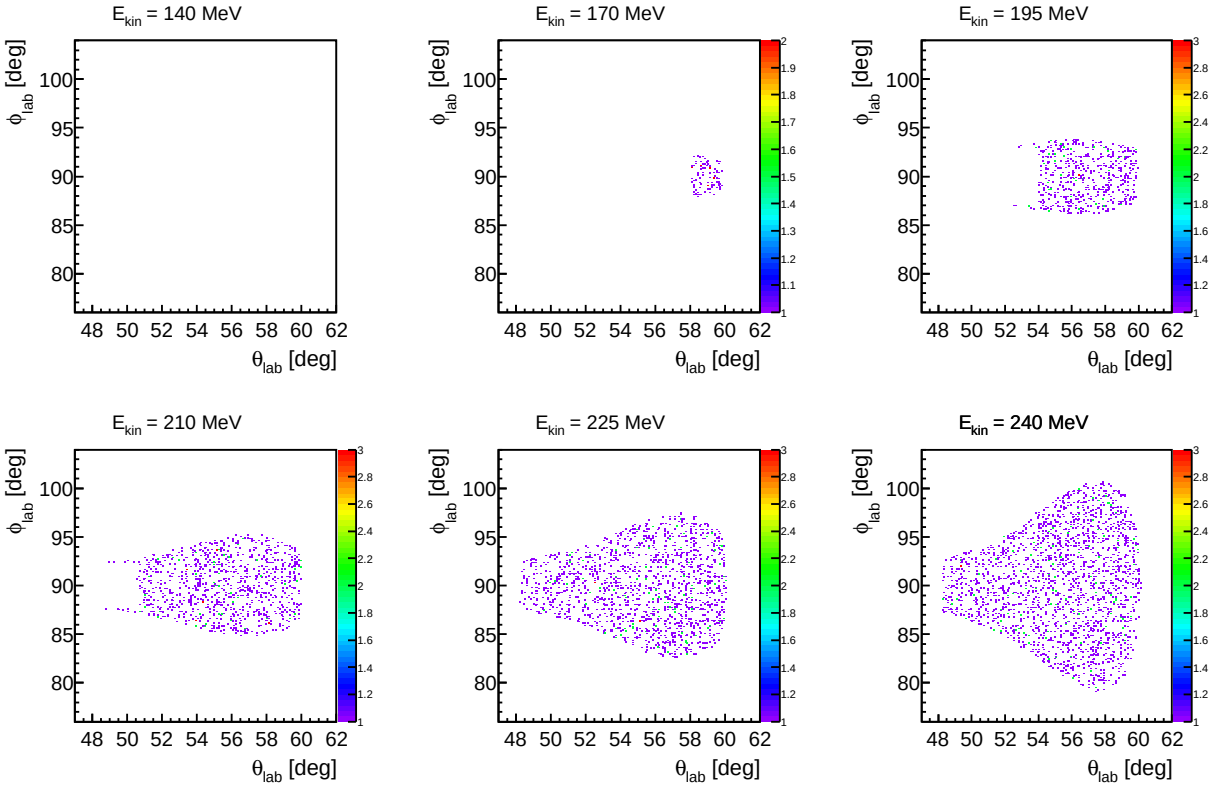

Figure 4.7: Transported $\theta_{lab} - \phi_{lab}$ matrices for different kinetic energy cuts for charge state 17^+.

4.1.4 The response function

The response function of PRISMA has been defined as the ratio between the output distribution of events detected on the focal plane $N_{\rm o}$ and the input distribution $N_{\rm i}$, both given as functions of $(E_{kin}, \theta_{lab}, \phi_{lab})$: $R(E_{kin}, \theta, \phi) = \frac{N_{\rm o}}{N_{\rm i}}$. Due to the symmetry, R can be integrated over ϕ_{lab}. Inverse of this matrix is the correction matrix, $f(E_{kin}, \theta_{lab})$, that is applied to the data detected at the focal plane. This function provides event distributions corrected by the response of the spectrometer and is used to obtain cross section in the following way:

$$\frac{d^2\sigma}{dE_{kin}d\theta_{lab}} = \left(\frac{d^2\sigma}{dE_{kin}d\theta_{lab}}\right)_{exp} \times f(E_{kin}, \theta_{lab}). \tag{4.1}$$

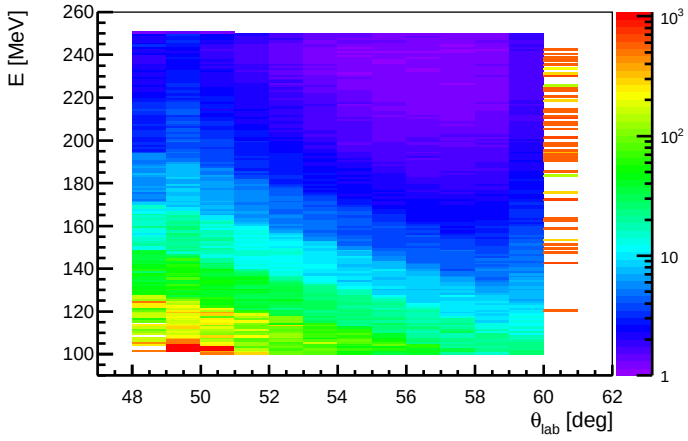

Figure 4.8: The correction matrix for ^{40}Ar.

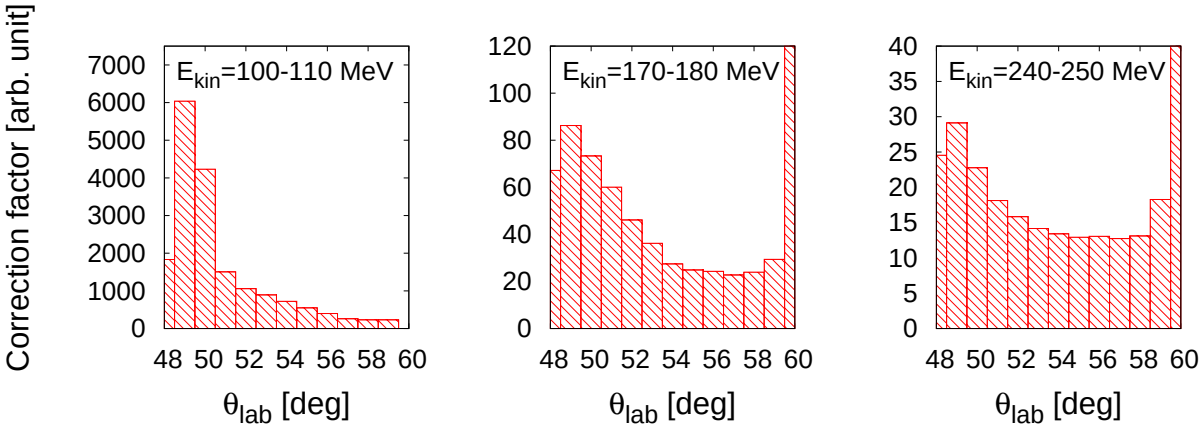

Figure 4.9: The correction factor for ^{40}Ar for different kinetic energy intervals labelled in the panels.

Figure 4.8 shows correction matrix obtained considering the entire charge state distribution of ^{40}Ar ions. Projections of θ_{lab} for different kinetic energy intervals are shown

in Fig. 4.9. As expected, in all three cases the largest corrections are at the borders of the angular acceptance, with large differences in absolute values depending on the kinetic energy of the incoming ion. It is important to notice that corrections are made on bi-dimensional matrices, and correction factors maybe be large both in θ_{lab} and energy.

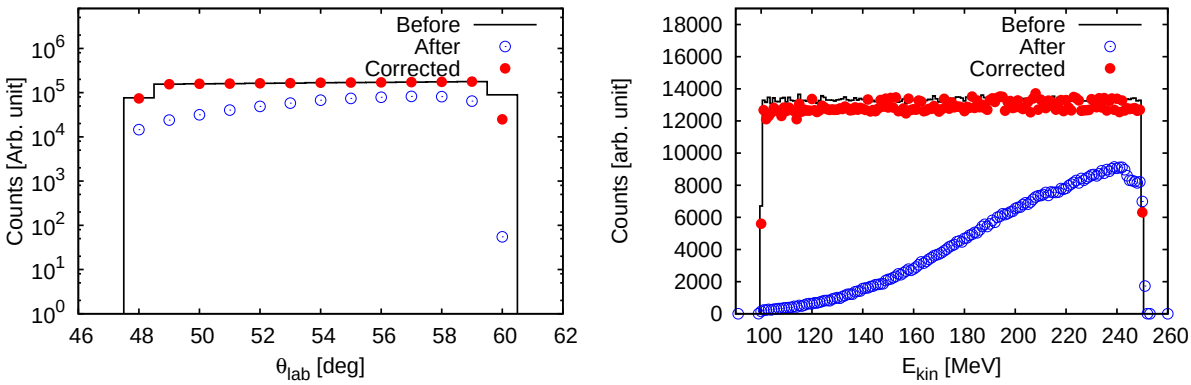

(A) Projection of θ_{lab}.

(B) Projection of E_{kin}.

Figure 4.10: The uniform distribution of ^{40}Ar. Black line represents input distribution, before the transport, blue open points represent transported distribution and the red full points are distribution corrected for the transmission of PRISMA.

To demonstrate the correctness of the described procedure we plotted in Fig. 4.10 projection of the uniform distribution before and after the transport, together with the transport corrected one. The borders (especially the largest angle) are not perfectly reproduced due to the trajectories which are not entering into the spectrometer since the input distribution is slightly larger than the quadrupole entrance.

Error induced by the response function can be estimated if one builds, for each of the studied channels, several response functions. This can be done by calculating the average value of nearby cells with different smoothing procedures, thus obtaining different response functions starting from the original one. Then the comparison of these different response functions is used to estimate the error. The average value depends on the technique and the size of the average bin. Two techniques are used:

1. **Gaussian smoothing**, which is a smoothing procedure that is using a Gaussian function to calculate the average value of the neighbouring cells in the matrix.
2. **Moving average**, is a calculation which analyses data points by creating a series of averages of different subsets of the full data set.

Finally, 5 different values of the correction factor for each response function cell are obtained:

- the original correction factor
- 2 moving average values (3 and 5 channel boxes)
- 2 Gaussian smoothing values (3 and 5 channel boxes).

The average of this 5 values gives the final correction factor. The total error is this one in quadratic sum with the statistical error of experimental data.

The same procedure has been applied for the construction of the response functions for different ions (Ca, K, Ar, Cl, S isotopes). The largest total correction factor (the ratio of the integral of transported corrected events and transported events) is obtained for proton pick-up and neutron stripping channels, since these channels are mostly affected by transport in PRISMA. Result is shown in Fig. 4.11. The difference is partly coming from different kinetic energies of the ions, together with magnetic fields that were adjusted for Ar isotopes (to remind it was adjusted to have the most intense charge state 16^+ of ^{40}Ar in the center of the focal plane). The transport of ions in magnetic fields depends on p/q (or A/q) and the transport of proton pick-up channels is affected more than the stripping ones, since the calculated charge state distribution (and the A/q ratio) deviates more from the ^{40}Ar channel.

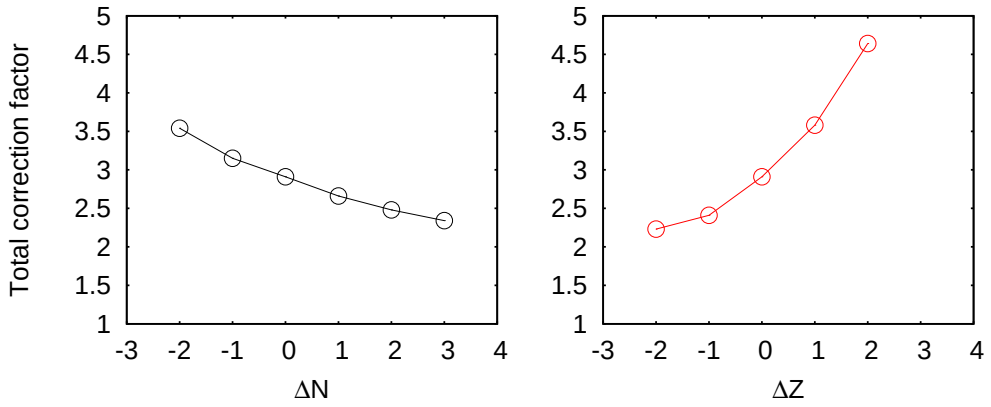

Figure 4.11: The total correction factors obtained for different channels.

A 100% intrinsic detection efficiency is assumed over the whole PRISMA angular range, which is quite reasonable for medium-mass systems.

4.2 The response function test

The response function R has been tested with the input distributions calculated with the semi-classical model GRAZING [4–6]. As it has been demonstrated [1] this model well reproduces the multinucleon transfer reactions in absolute values of cross sections, shapes of angular distributions and total kinetic energy loss distributions. In particular, one nucleon transfer channels, $(+1n)$ and $(-1p)$, are very well reproduced. Thus as a first check of the response function we constructed the input events calculated by GRAZING, with energy and angular distributions similar to the experimental ones.

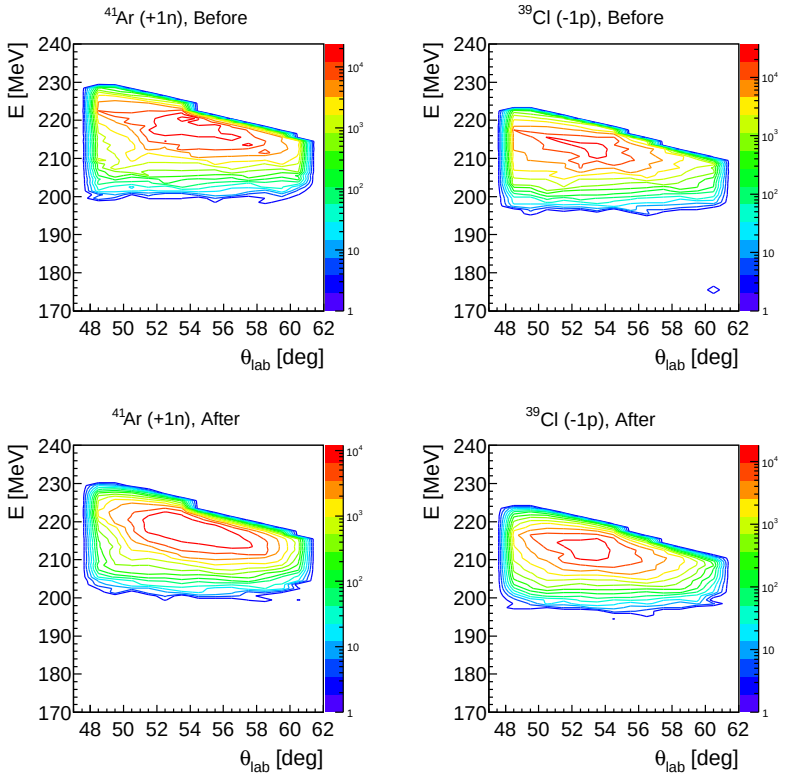

Figure 4.12: Input GRAZING distribution and distribution after the transport for $(+1n)$ and $(-1p)$ channels.

One million events have been produced with a Monte Carlo code for $(+1n)$ and $(-1p)$ channels according to (E_{kin}, θ_{lab}) calculated with GRAZING and transported with the ray-tracing code to the focal plane of PRISMA. Two-dimensional matrices showing input and transported distribution are shown in Fig. 4.12. The projections on the θ_{lab} axis (left) and the E_{kin} axis (right) are displayed in Fig. 4.13. In each panel the solid lines are the input distributions calculated with GRAZING, the blue points correspond to the transported

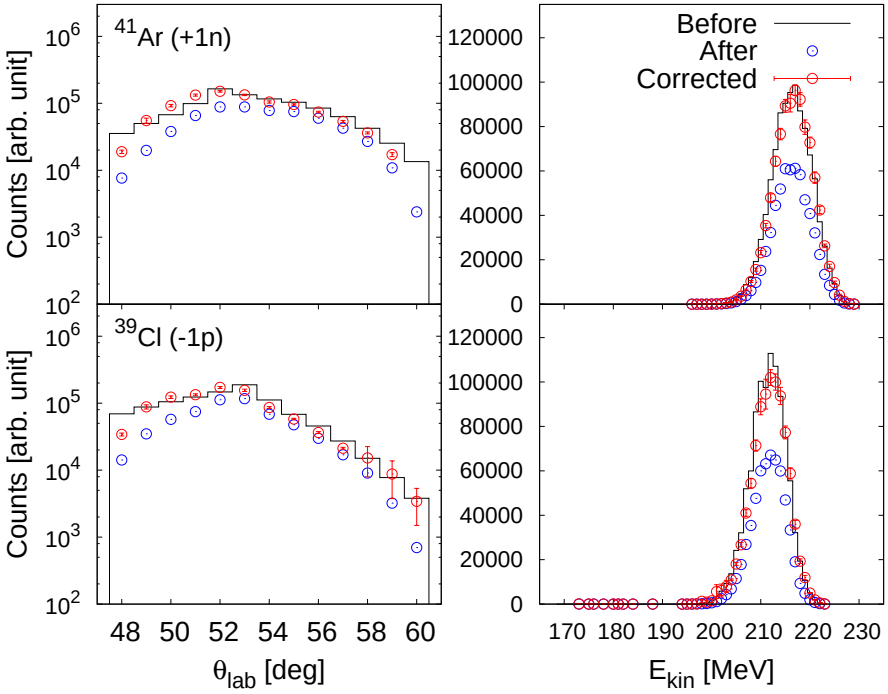

Figure 4.13: Projections of the dispersion angle θ_{lab} and the kinetic energy E_{kin} with errorbars for $(+1n)$ and $(-1p)$ channels before (black solid line) and after the transport (blue points), and also corrected with the response function (red points).

distributions at the focal plane and the red points are events after the correction function has been applied. The excellent agreement between the original input calculations and the corrected distributions of events demonstrate the validity of the response function, and of the applied procedure.

5 Experimental results

This Chapter presents main experimental results from the ^{40}Ar+^{208}Pb multinucleon transfer reaction performed with PRISMA-CLARA set-up: elastic cross section, angular distribution and total kinetic energy loss distribution of different transfer channels, together with energy and angle integrated cross sections. The results have been compared with the GRAZING calculations [4–6], and this comparison will be discussed in Chapter 7.

5.1 Yields

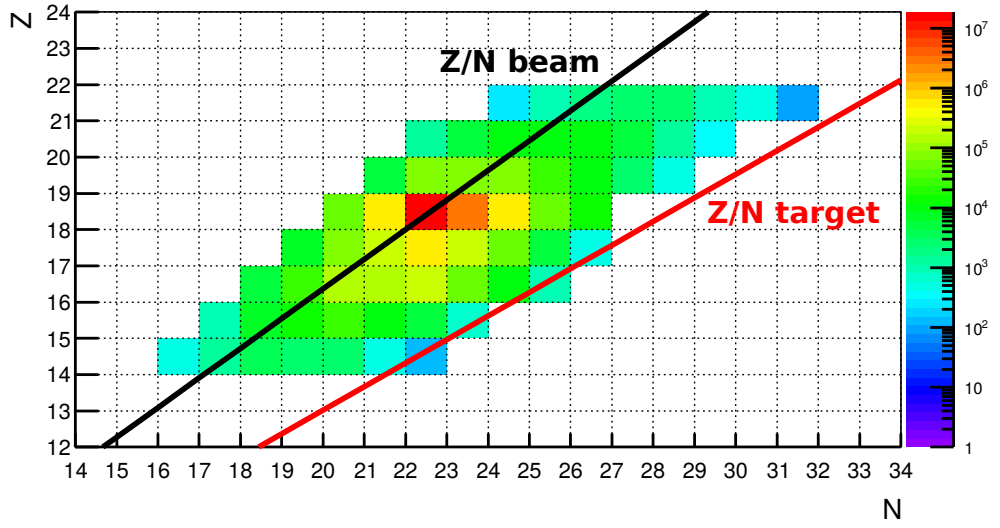

Figure 5.1: Energy and angle integrated yields for different channels produced in the ^{40}Ar+^{208}Pb multinucleon reaction. Only channels with significant statistics are presented. The strongest channels, from two proton pick-up to two proton stripping, will be further discussed.

Energy and angle integrated yields for different channels produced in the ^{40}Ar+^{208}Pb multinucleon reaction are shown in Fig. 5.1. The ^{40}Ar+^{208}Pb reaction shows quite sym-

metric distribution around the projectile nuclei in the sense that not only the favoured neutron pick-up and proton stripping channels, but also the neutron stripping and proton pick-up channels are populated. This can be understood from the simple Q-value considerations which are essentially dominated by the properties of the lighter projectile [12]. Since ^{40}Ar is on the right side of the stability line, toward neutron-rich nuclei, also proton pick-up and neutron stripping channels start to be open, being still the proton stripping and neutron pick-up channels stronger.

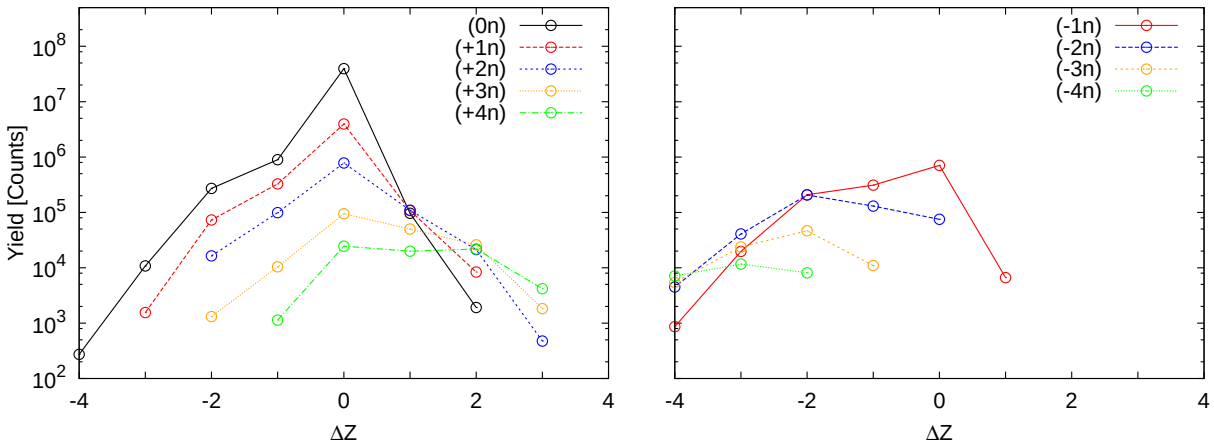

Figure 5.2: Energy and angle integrated yields for different neutron pick-up (left panel) and neutron stripping (right panel) channels as a function of number of transferred protons.

The same yields are plotted in Fig. 5.2 separately for neutron pick-up and stripping channels as a function of number of transferred protons. Channels presented on the left panel show regular behaviour especially when the proton stripping channels are involved, i.e. for channels $(-xp+yn)$. The crossing starts for the neutron pick-up channels in the proton pick-up side being the most pronounced in the point where $(+1p)$ crosses with $(+1p+1n)$ and $(+1p+2n)$ channels. The same irregular, but even more pronounced, behaviour can be seen on the right panel, especially for channels where three or more neutrons are transferred together with the large number of protons. These crossings of different lines can indicate the importance of secondary processes like evaporation. The evaporation is expected to contribute more in this region since yield can be severely affected with even a small contribution of nearby more neutron-rich channel with larger cross section.

The same was observed for the ^{40}Ca+^{208}Pb reaction [30] where the regular pattern observed for proton stripping and neutron pick-up was compatible with a successive mechanism where neutrons and protons acted independently. The irregular pattern that was

observed for neutron stripping channels indicated neutron evaporation process that influenced the final isotopic distribution especially for massive proton transfers ($\Delta Z > 3$).

The behaviour observed on the left panel, for $(+xp+yn)$ channels, may arise from significantly different energy distribution which may be attributed to the presence of different mechanism, like deep inelastic collision, or some additional degrees of freedom like correlations. The effect of different mechanisms can be studied with the total kinetic energy loss distributions (TKEL). It would be interesting to see if these channels that show irregular behaviour also have different TKEL. Thus, as a second step we looked more closely at the TKEL distributions of different channels.

5.2 The TKEL distributions

In a binary reaction $a+A \rightarrow b+B$, where a is the projectile nucleus that impinges on the target nucleus A that is at rest, the target-like and the projectile-like nuclei, B and b respectively, are produced. Total kinetic energy before and after the collision is $K^i = K_a$ and $K^f = K_B + K_b$, so the reaction total kinetic energy loss can be defined as:

$$TKEL = K^i - K^f = K_a - (K_b + K_B) \tag{5.1}$$

where kinetic energy of the projectile nucleus K_a is known, kinetic energy of the projectile-like nucleus K_b is measured in PRISMA, and kinetic energy of the target-like K_B is reconstructed. Q-value is defined as:

$$TKEL = -Q. \tag{5.2}$$

For a binary process, and taking into account the conservation of energy, one gets:

$$m_a c^2 + m_A c^2 + K_a = m_b c^2 + m_B c^2 + K_b + K_B + E_b^* + E_B^* \tag{5.3}$$

$$-Q = K^i - K^f = (m_b + m_B - m_a - m_A)c^2 + E_b^* + E_B^* = -Q_{gs} + E_b^* + E_B^* \tag{5.4}$$

where E_b^* and E_B^* are excitation energies of two nuclei produced after the collision. The quantity Q_{gs}, which is the ground-to-ground state Q-value, is then well defined as:

$$-(m_b + m_B - m_a - m_A)c^2 = Q_{gs} \tag{5.5}$$

and corresponds to the TKEL of a reaction leading to the nuclei b and B in their ground states. The calculated values are plotted in Fig. 5.3.

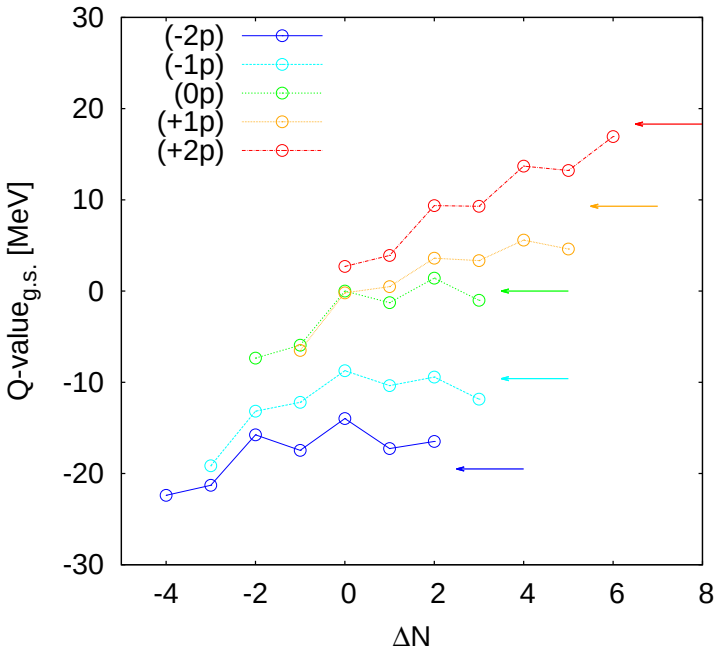

Figure 5.3: The ground-to-ground state Q-value. The arrow indicates the position of the optimum Q-value.

Table 5.1: The Q-optimum values calculated with Eq. 1.8 in Chapter 1.

Channel	Q**-optimum [MeV]**	**Channel**	Q**-optimum [MeV]**
$(-2n)$	-0.67	$(-2p)$	-16.95
$(-1n)$	-0.34	$(-1p)$	-7.89
$(+1n)$	0.36	$(+1p)$	6.90
$(+2n)$	0.72	$(+2p)$	12.95

The matching between incident and outgoing channels, where heavy-ion induced direct transfers have the largest cross section, is characterized by the optimum Q-value. In the

first approximation it can be expressed as:

$$Q_{opt} \approx E_{cm}\left[\frac{Z_b Z_B}{Z_a Z_A} - 1\right] \tag{5.6}$$

and it is plotted in Fig. 5.3 with arrows. The optimum Q-value is also calculated with Eq. 1.8 for some channels and these are listed in Tab. 5.1. Notice that for $(-1p)$ and $(+1n)$ transfer channels Q_{gs} and Q_{opt} are better matched.

The Q-value or TKEL distributions thus define the excitation energies of the two nuclei produced in the reaction. Figures 5.4, 5.5 and 5.6 show as black histograms TKEL distributions for all three PRISMA angular settings for different reaction channels. Figure 5.5 with PRISMA at 54° (the grazing angle) shows also GRAZING calculations which will be discussed in Chapter 7. The ground-to-ground state Q-value is labelled with red line for all channels. The optimum Q-value is labelled with blue arrow. To remind, one detects secondary fragments and the TKEL spectra are constructed assuming binary reactions. The excitation energies of both light and heavy fragments, as well as their mutual excitation, are embedded into these TKEL distributions.

One can clearly follow the evolution pattern as a function of number of transferred neutrons and protons. It can be seen that the distributions for pure neutron transfer channels have major contribution close to the optimum Q-value (which is ≈0 MeV) with an increasing strength of large energy loss components as more and more neutrons are transferred. The trend is similar for channels including transfer of protons, with a faster growth of large TKEL components. As more nucleons are transferred, TKEL is changing and moving away from the ground-to-ground state value to higher losses. Even more, for massive transfer channels, especially in the proton pick-up region, the TKEL distributions look quite similar, with the shape which is almost channel independent, and can be described with the wide distribution centred at large energy losses. Of course, in these cases, in the interpretation of the spectra one should keep in mind the possible effects of the spectrometer, especially its energy acceptance.

Looking at Figs. 5.4, 5.5 and 5.6 one can follow how the TKEL distributions evolve while going from forward to more backward angles. To better follow these changes, we separated the TKEL distributions for selected channels in Fig. 5.7. One can notice two kinds of events. One is with the pronounced peak at small TKEL, which will be labelled as quasi-elastic (QE). The other is characterized by large TKEL, forming a long tail in

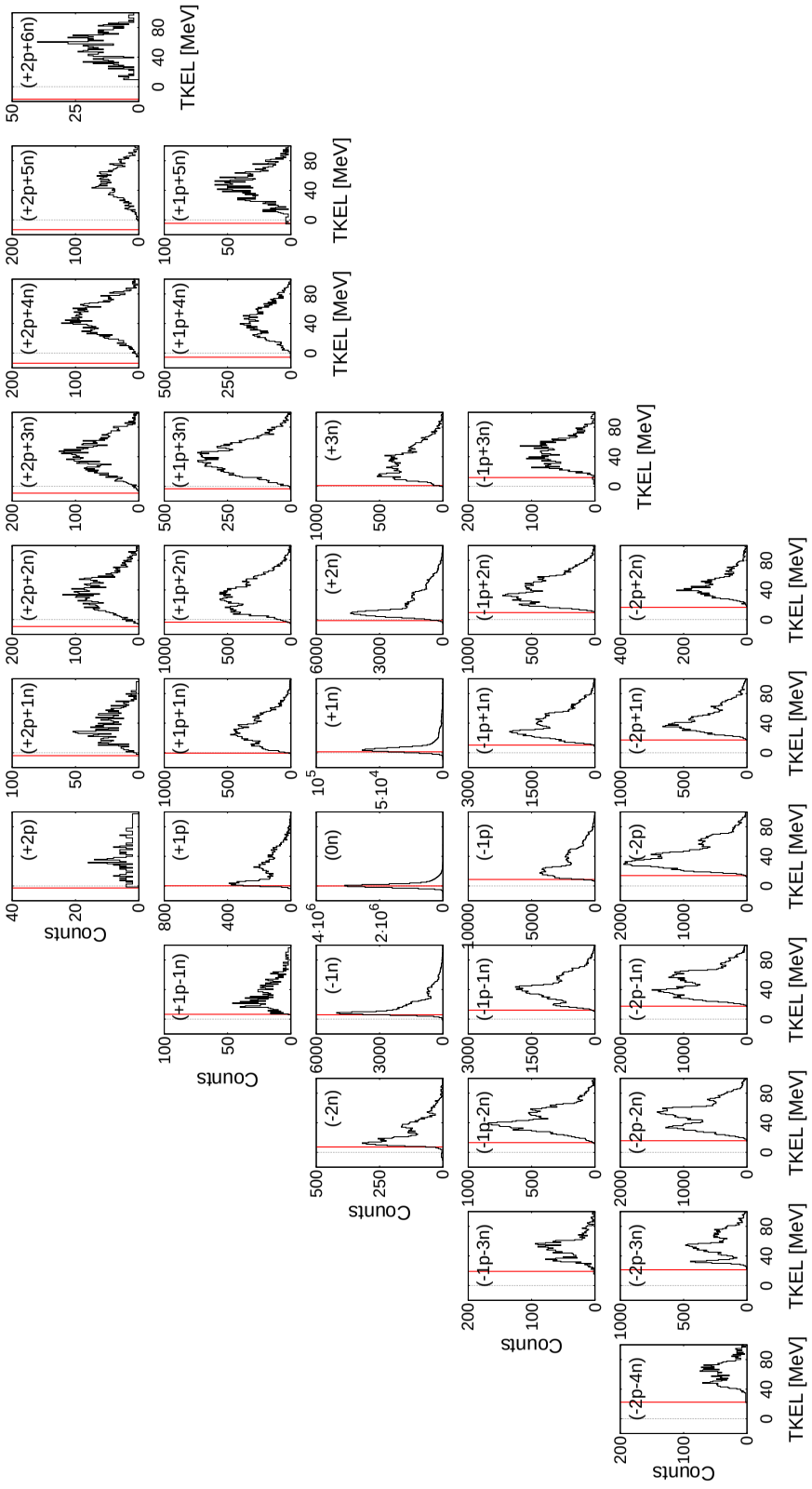

Figure 5.4: Experimental TKEL distribution for all analysed channels for PRISMA positioned at 46°. Red vertical line indicates position of the ground-to-ground state Q-value, Q_{gs}.

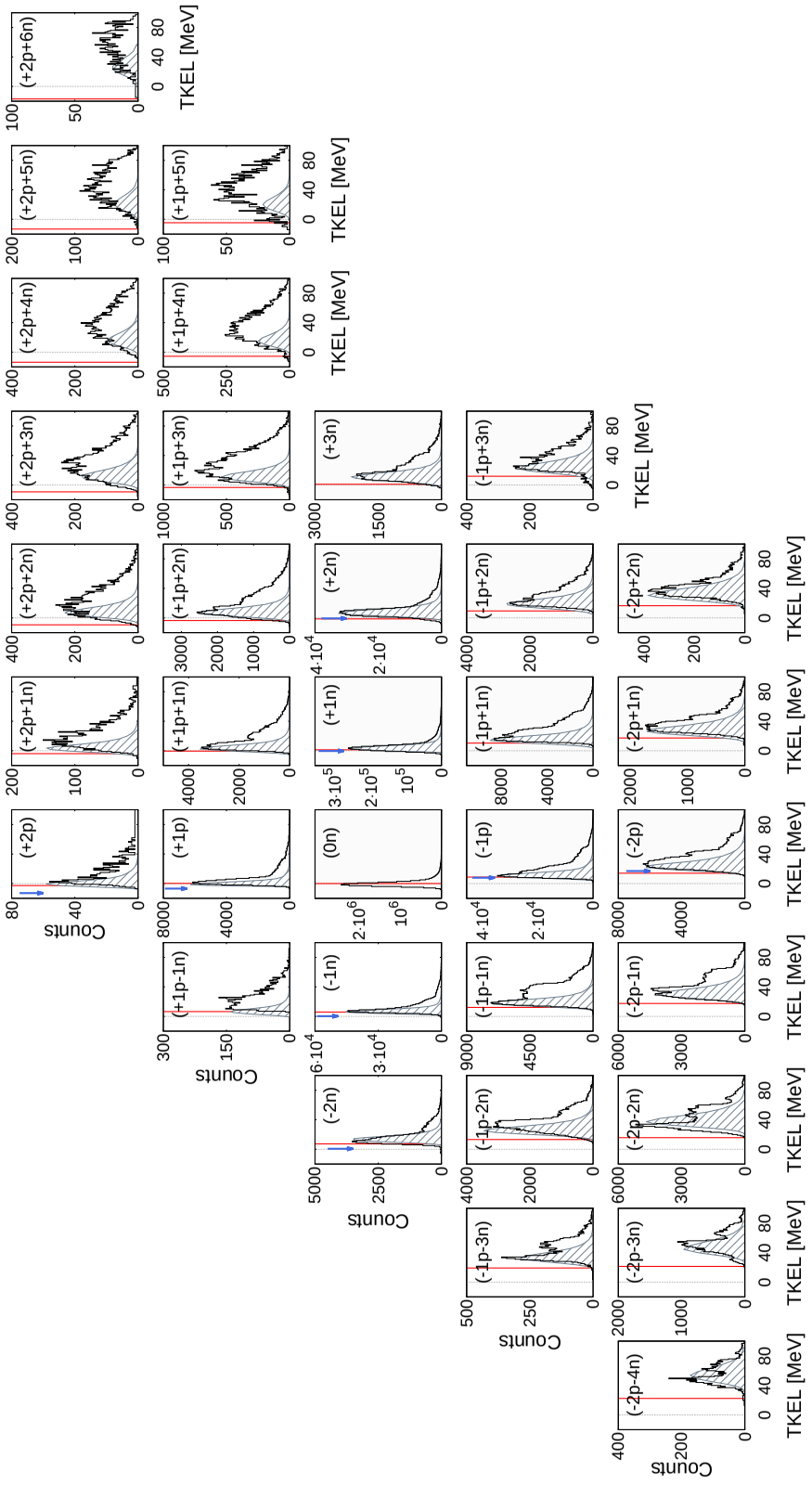

Figure 5.5: Same as in Fig. 5.4 for PRISMA positioned at 54°. The shaded grey area is TKEL distribution calculated by GRAZING. Proton stripping and neutron pick-up channels are shown with grey panels.

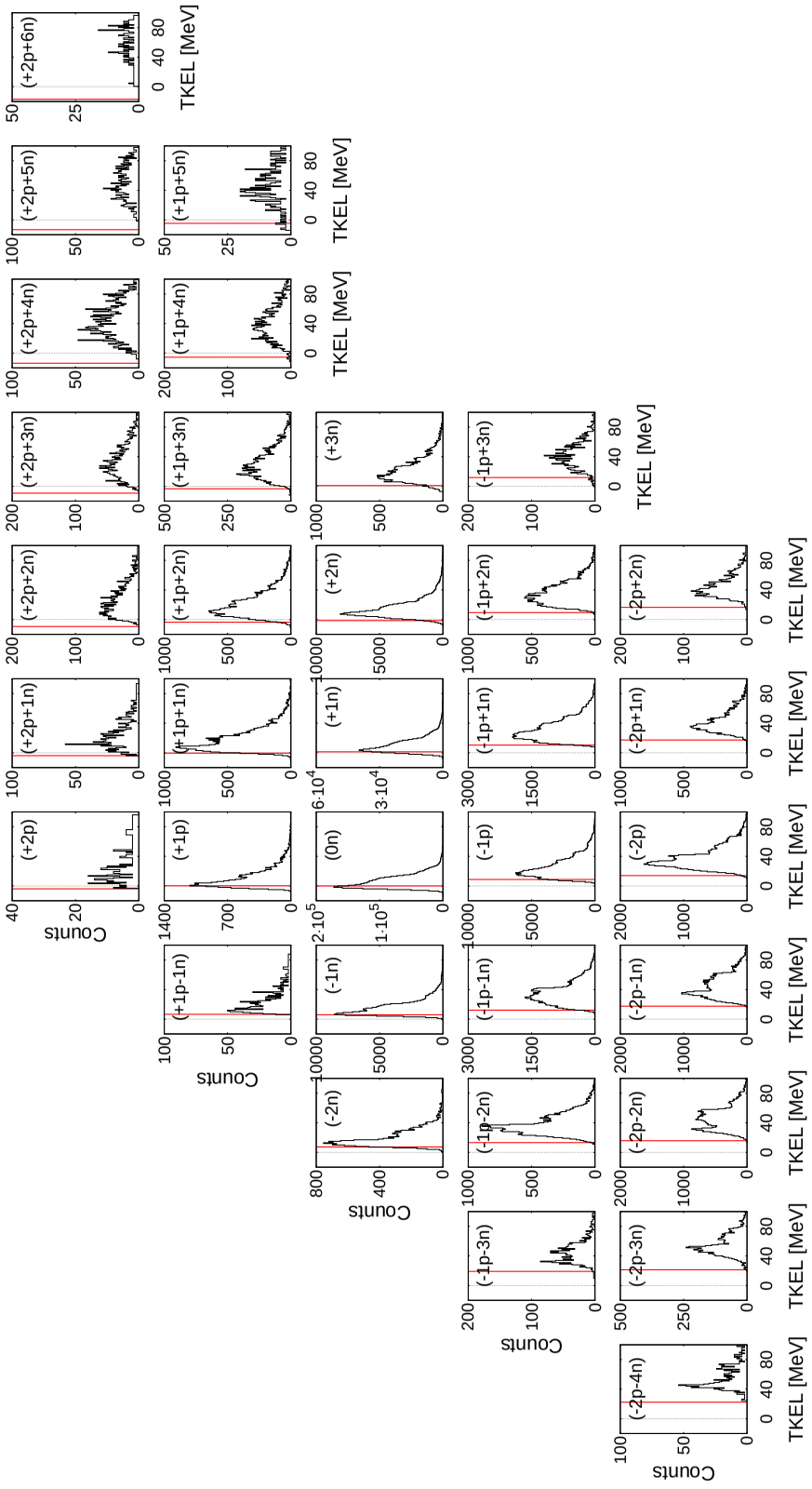

Figure 5.6: Same as in Fig. 5.4 for PRISMA positioned at 59°.

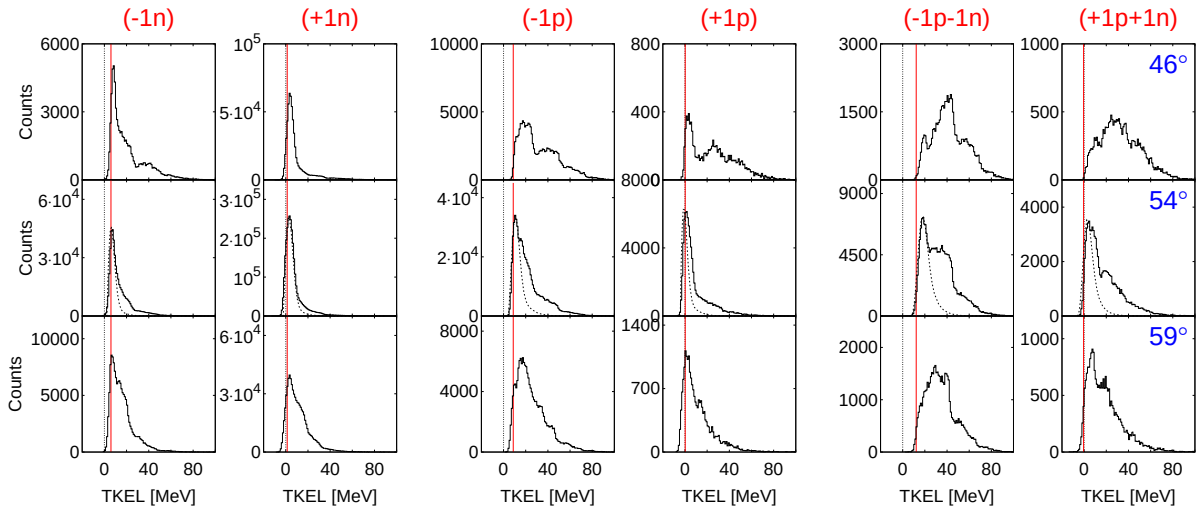

Figure 5.7: TKEL distribution of selected channels for all three PRISMA angular settings. It is important to notice that excitation energy of both light and heavy partner is embedded into the TKEL distribution. Red vertical line indicates position of the ground-to-ground state Q-value, Q_{gs}.

the distribution. Since incident energy is ≈30% above the Coulomb barrier, it is assumed that these large TKEL are associated with strongly deformed configurations and they will be labelled as deep inelastic collision (DIC). This assumption will be tested later.

A pure quasi-elastic scattering is recognized by a well defined peak in TKEL. This situation is present here in the neutron transfer channels. The deep inelastic collisions usually have large transfer of energy with a broad distribution since a large amount of kinetic energy is dissipated into internal excitation energies of two emerging fragments [79]. This kind of behaviour can be responsible for the formation of long tails, or additional peak-like structure. Even if generally there is a difference in the mean energy loss values of these two cases, it is difficult to disentangle them since their overlap may be significant. However, it is expected that DIC contributes more at more forward angles which will be discussed in more details in next section. One can notice, for example, that in the case of $(-1n)$ channel, the second wide peak is better separated from the narrow peak at small TKEL at the most forward measured angle, while for the most backward measured angle the overlap of these two structures is much stronger. In addition, the large energy loss component becomes more pronounced as more particles are transferred, especially at forward angles (see for example $(-1p-1n)$ channel in Fig. 5.7 or Ca isotopes in Fig. 5.4).

5.3 Quasi-elastic and deep inelastic components

To better discuss the structure of these two components seen in the TKEL distributions, we construct the differential and total cross sections trying to separate them. Large dynamic range of the PRISMA spectrometer allowed, to some extent, to detect and study both components, QE and DIC, with the same magnetic field settings. As already discussed, a clear distinction between quasi-elastic and deep inelastic reactions on the basis of the amount of energy or mass transfer is not easy to make since there is a smooth transition between them (i.e. no sharp separation) [10]. This type of study was performed in Refs. [79] and [80] where the ^{48}Ti+^{208}Pb, ^{64}Ni+^{208}Pb and ^{80}Se+^{208}Pb reactions were measured at energies slightly above the Coulomb barrier also at forward angles.

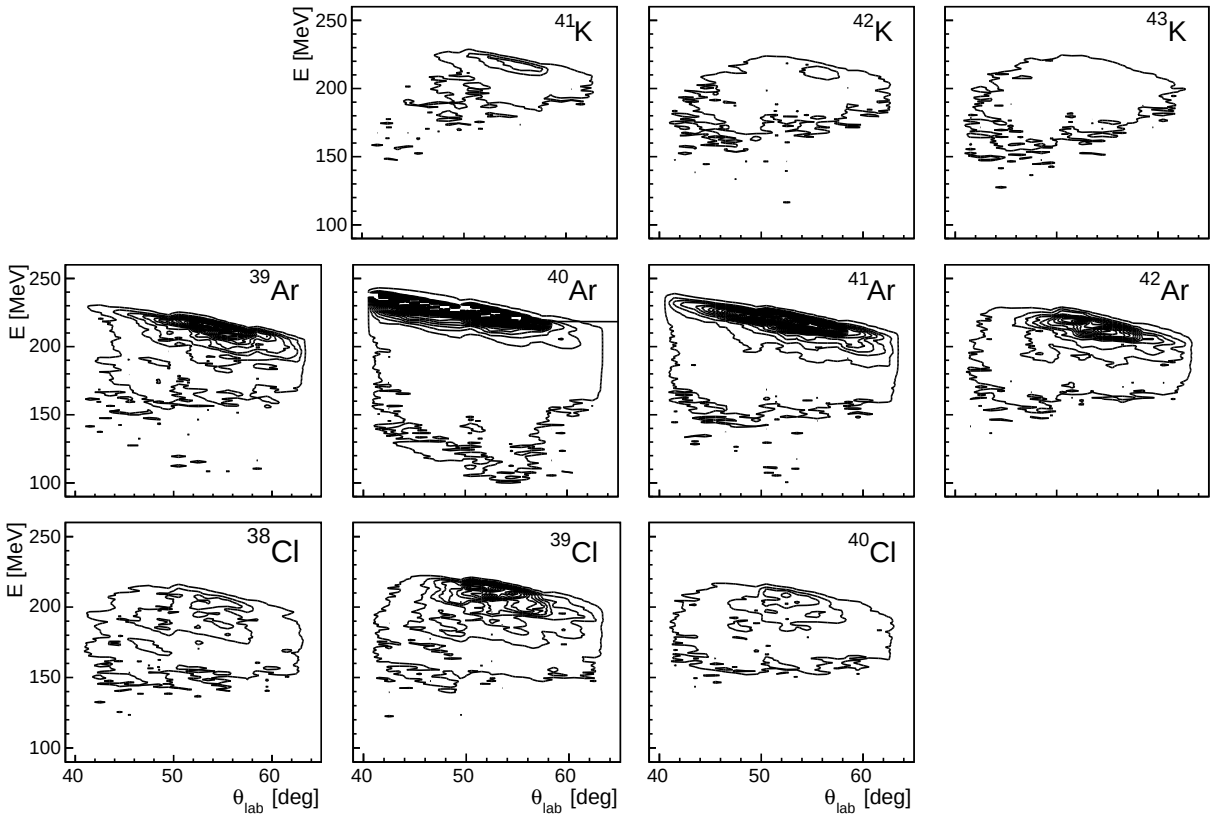

Figure 5.8: Wilczynski plots (i.e. E_{kin} versus θ_{lab}) for the indicated transfer channels. The contours are drawn in all the frames, every 200 μb/sr/MeV starting from 50 μb/sr/MeV.

Wilczynski plots (i.e. E_{kin} versus θ_{lab}) for the indicated channels are displayed in Fig. 5.8 and show the two-dimensional evolution of transfer process. For few-particle transfer, and especially for neutron transfers, the bulk of the distribution is concentrated within ∼10 MeV at energies closer to the beam energy, and the peak moves very smoothly

from the backward towards forward angles. Qualitatively this fact supports the idea that neutrons behave as independent particles in the transfer process. As the reaction proceeds with a larger number of transferred nucleons, events spread in energy. A shift of the distribution is seen in energies from backward to forward angle towards lower values that indicates that deep inelastic events with large losses of energy contribute in multinucleon transfer.

The two components present in the TKEL spectra were separated for each scattering angle with Q-value cuts in the TKEL-A matrix. The peak below TKEL ∼20 MeV was labelled as QE, and the one above as DIC. This limit was adjusted according to the ground-to-ground state Q-value, in order to cover ∼20 MeV range. This method has been tested by varying different approaches for the separation of two distributions. We tried to separate these two components in the two dimensional TKEL-A matrix, and with the fitting procedure by using two Gaussian distributions in the TKEL spectra, as well as with a sharp cut in the same spectra. Results of different approaches are very similar.

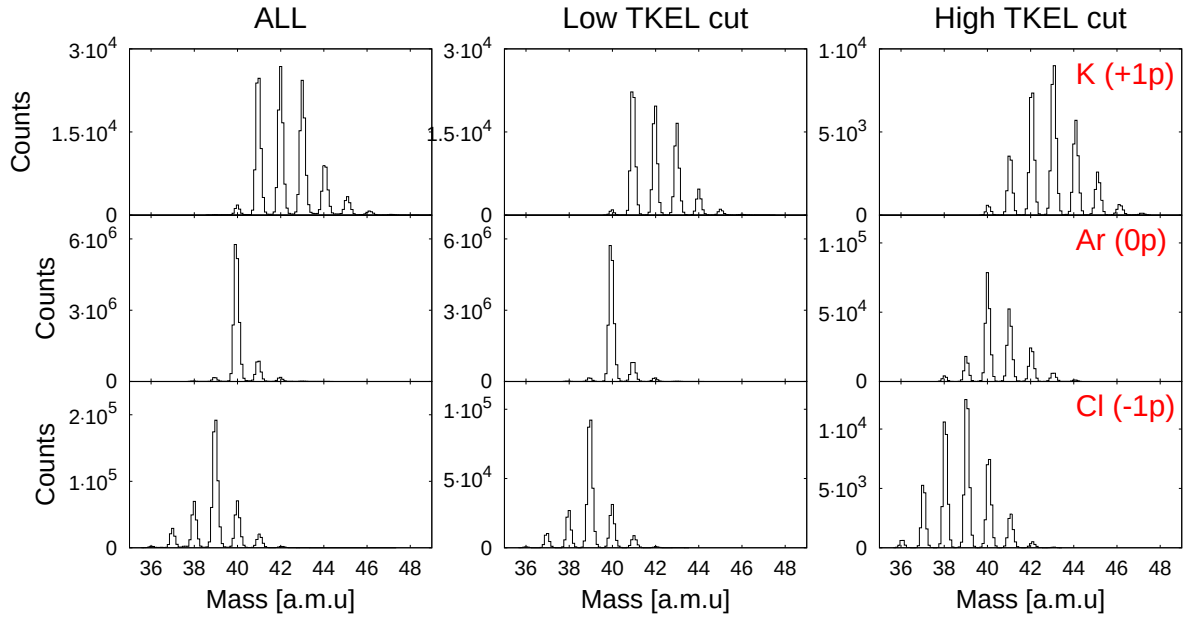

Figure 5.9: The mass distributions of three dominant channels for entire TKEL (left panel), for the low energy losses (central panel) and for the large energy losses (right panel).

Figure 5.9 shows mass distribution for entire TKEL range (left panel), and for small (middle) and large (right) energy losses separately. For these few nucleon transfer channels, looking at the low TKEL components, one sees asymmetric mass distribution typical for QE processes, with a tendency to become Gaussian-like as more and more nucleons are

transferred. This tendency becomes more marked for large TKEL. For large energy losses the shape of the mass distribution is different, much broader, more Gaussian-like. Such distribution is expected in DIC, where shape is built up from the convolution of the true distribution and the spectrometer's selection. One can notice that the strongest channels in low and high TKEL cuts are quite different. For example, the strongest channel for potassium isotopes for low energy cut (see Fig. 5.9) corresponds to the pure one proton pick-up channel, ^{41}K, while for the high energy cut it is shifted to $(+1p+2n)$, ^{43}K.

The ratio of the energy integrated yields for low and entire TKEL as a function of the scattering angle can be seen in Fig. 5.10. At the most forward angle the contribution of the low TKEL component in the total yield decreases for some channels down to ≈20%. One can also notice that few nucleon transfer channels are mostly associated with small energy losses. This is especially obvious for $(\pm n)$ channels. The large energy loss component becomes more dominant in more complex multiparticle transfers, especially when protons are involved.

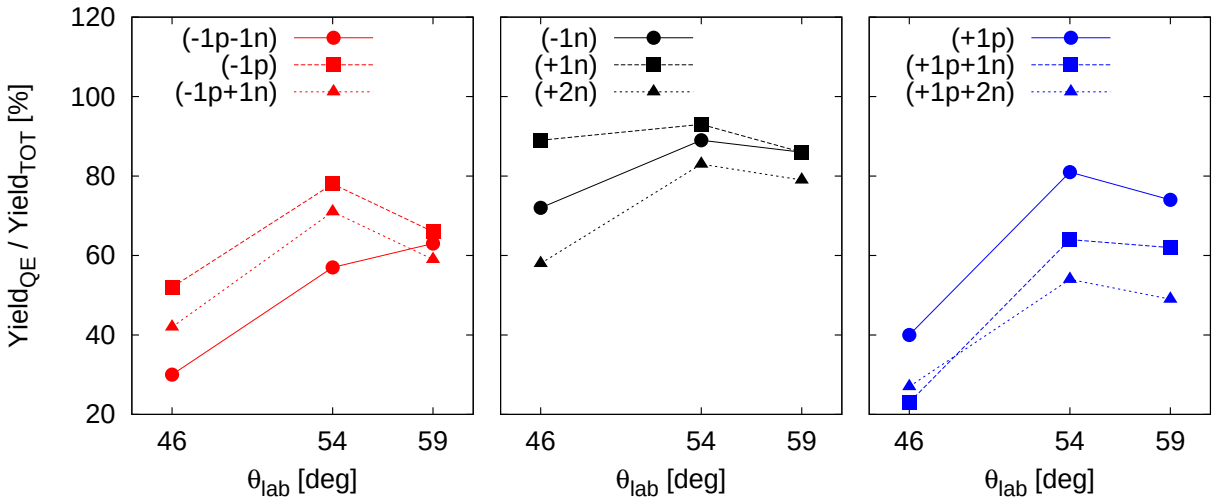

Figure 5.10: The ratio of the yield integrated over the low TKEL part and over entire TKEL for different PRISMA angular settings. Lines serve to guide the eye.

5.4 The elastic scattering

In elastic scattering the reactants preserve their mass and charge and its investigation is usually the first important step in any reaction mechanism study [8]. It provides information on the (outer part of) interaction potential between colliding nuclei and the

knowledge of its size and shape is the basis of the description of entire scattering process. Because of the Coulomb excitation and of the nuclear reactions which take place at the distance where the ion-ion potential is felt, one has also to take into account the depopulation of the elastic channel which is accounted for by an absorption [81]. This is usually done for heavy-ion reactions through the imaginary potential [82] or coupled channel calculations.

With the PRISMA energy resolution of $\sim 1\%$ it is possible to discriminate between individual states only in specific cases, for example when closed shell nuclei are involved [30]. The use of γ arrays may provide a much better energy resolution, but we are missing the possibility to measure the ground-to-ground state transitions [29]. The coupling of the PRISMA spectrometer to the large γ-array CLARA was successfully used to extract also the elastic scattering in heavy-ion collisions through the method illustrated in [72, 73, 83].

Utilization of two particle devices (i.e. PRISMA and a small Si detector), one of which is at forward angles to monitor the Rutherford scattered ions, eliminates the need of target thickness and beam intensity information. If we are in proper experimental conditions (PRISMA set at a proper angle) we can determine the effective solid angle of PRISMA and its overall detectors efficiency by comparing the measured elastic scattering and Rutherford calculated one. This solid angle $\Delta\Omega_P(\theta)$ is then used to obtain the absolute cross section for other transfer channels which is equal to:

$$\left(\frac{d\sigma}{d\Omega}\right)_{ch} = \frac{N_P}{N_{mon}} \frac{d\Omega_{mon}}{d\Omega_P} \left(\frac{d\sigma}{d\Omega}\right)^R_{mon} \tag{5.7}$$

where N_P is number of counts in PRISMA, N_{mon} number of counts in monitor, $d\Omega_P$ and $d\Omega_{mon}$ solid angles of PRISMA and monitor, and $\left(\frac{d\sigma}{d\Omega}\right)^R_{mon}$ is the Rutherford cross section.

Another approach is to use true elastic counts for the normalization purpose. This procedure, with PRISMA and CLARA, has been tested in Refs. [73] and [83] and it was adopted here. Such procedure should be reliable, provided that the shape of the spectrum in coincidence with γ rays is weakly dependant on the γ multiplicity. This fact is fulfilled for nuclei having low level density close to the ground state.

In the studied case, for each θ_{lab}, total kinetic energy loss spectra with PRISMA alone and PRISMA in coincidence with CLARA have been constructed as shown in Fig. 5.11. The first histogram presented with black line was built with the only requirement

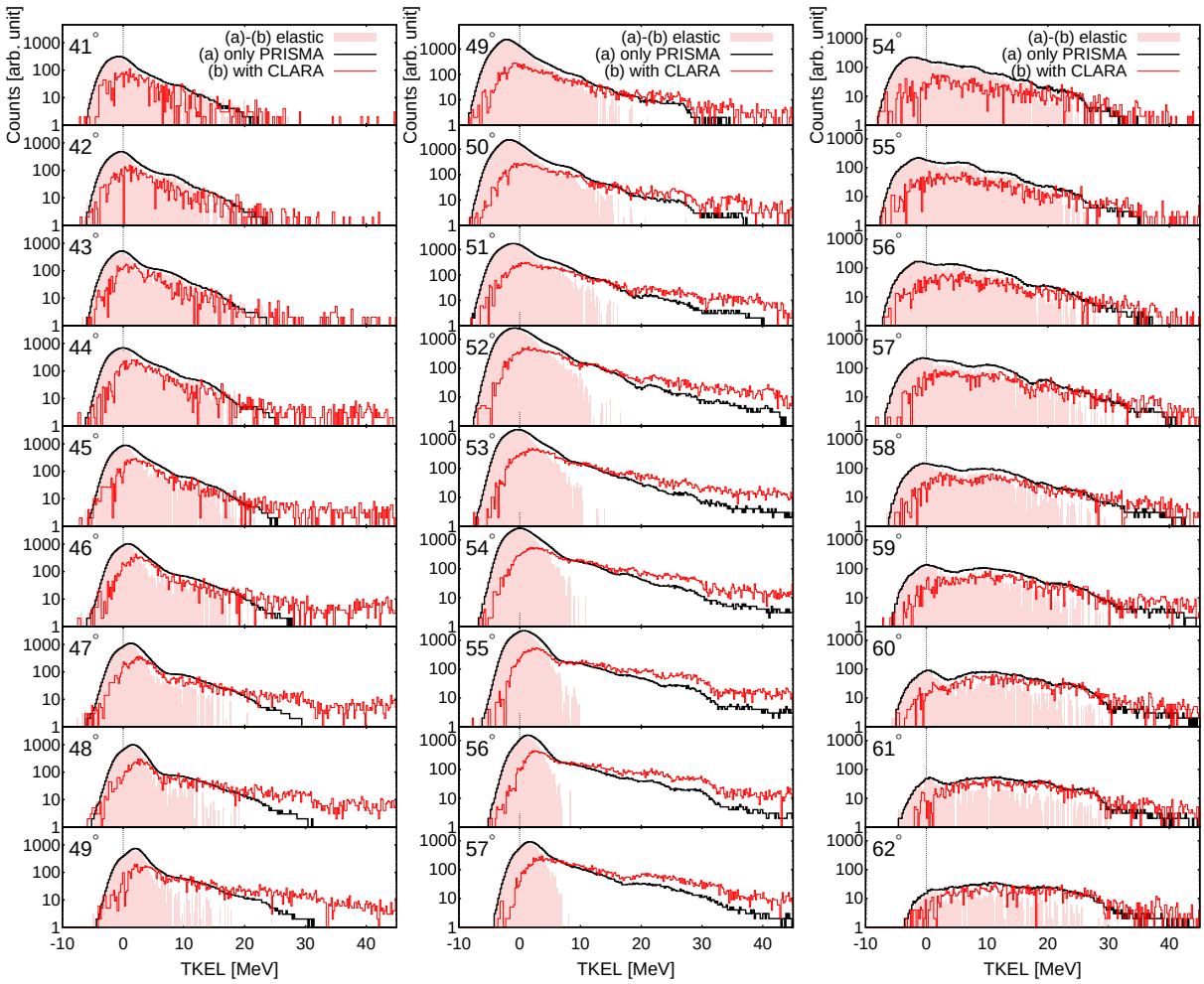

(A) PRISMA at 46°. (B) PRISMA at 54°. (C) PRISMA at 59°.

Figure 5.11: TKEL spectra for ^{40}Ar at three different PRISMA angular settings (angles 46°, 54° and 59° are shown in left, middle and right panels, respectively). Black lines (a) correspond to TKEL spectrum without coincidence with γ rays (PRISMA alone), while the red one (b) is with additional request of at least one γ ray detected in CLARA. The later have been normalized in the inelastic tail above 6 MeV. The red shaded area is the subtraction of the two spectra (a)-(b) and represents the elastically scattered ^{40}Ar on a ^{208}Pb target. The procedure of subtraction is performed in steps of one degree over the entire entrance angular range. The counts in the peak, at the most forward angles, are considered to be mainly due to pure elastic scattering.

of detecting the ^{40}Ar ion in PRISMA. The TKEL of PRISMA alone is characterized by the dominant narrow distribution centred around the $Q_{gs} = 0$, shown in Fig. 5.11 as a dotted grey line, with the tails going towards the large energy losses. The dominant narrow distribution weakens when moving to backward angles, for PRISMA positioned at angle 59°, and due to this tails appear to be more prominent in the TKEL distribution. The second histogram, presented with red line, was obtained requiring at least one γ ray measured by CLARA. These two spectra are normalized in the tail region (above 6 MeV) and finally the difference spectrum is obtained by their subtraction (red shaded peaks).

The elastic peak obtained in such way is centred at TKEL=0 and its width is ∼3-4 MeV. The left side of the histogram in Fig. 5.11 reflects only the resolution of the spectrometer. These widths are consistent with the experimental energy resolution which is determined by the combination of the uncertainty of the energy loss in the target, the beam energy spread and the intrinsic resolution of the PRISMA spectrometer.

Full width at half maximum is between 3-4 MeV, determined mostly by the spectrometer's response. First excited state in ^{40}Ar is 2^+ at 1.46 MeV, and for the ^{208}Pb is 3^- at 2.61 MeV. This means that the first excited state may even be incorporated in the peak, but if the subtraction of TKEL in coincidence with CLARA is done properly it is expected that this doesn't affect counts in the elastic peak.

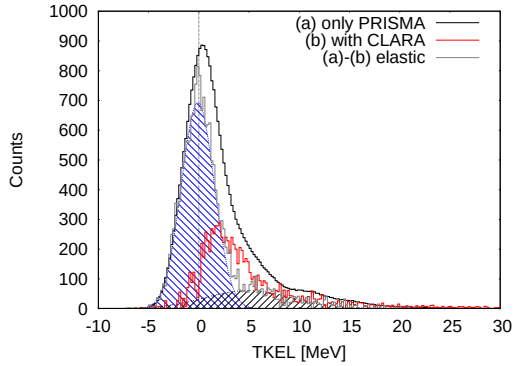

(A) An example of fitting procedure for $\theta_{lab} = 45°$.

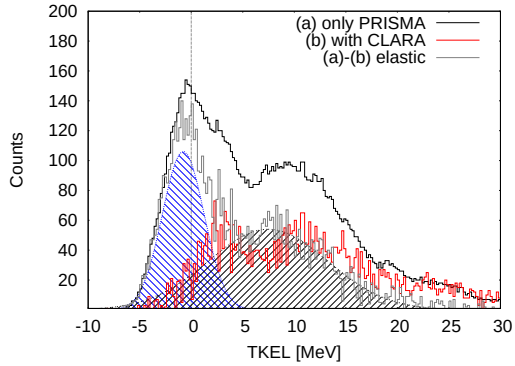

(B) An example of fitting procedure for $\theta_{lab} = 58°$.

Figure 5.12: Examples of fitting procedure for two different angles.

The number of events are obtained by fitting the red shaded peak in Fig. 5.11 with the Gaussian distribution or the sum of two Gaussian distributions where it was necessary to remove the remnant of the tail of the inelastic events, as illustrated in Fig. 5.12. In this way an elastic differential cross section has been constructed.

In order to ascertain the number of counts, additional analysis was performed. It was noticed that the lower part of the MCP detector had an inefficient surface segment. Thus the elastic scattering was constructed by using only the upper part of the MCP. The number of events was also corrected for shadows of the quadrupole mechanical nail structures. The fact that the distribution of events has to be symmetric in ϕ_{lab} was used to correct for the number of lost events. This procedure significantly lowered waiving behaviour of the angular distributions.

After that the correction factors for the transport of ions through the spectrometer,

Table 5.2: Transmission correction factors $f(\theta_{lab}, E_{kin})$ used for elastic scattering as a function of θ_{lab}. These factors were used to correct the experimental intensity of the elastic peak angle by angle.

θ_{lab} [deg]	$f(\theta_{lab}, E_{kin})$	θ_{lab} [deg]	$f(\theta_{lab}, E_{kin})$	θ_{lab} [deg]	$f(\theta_{lab}, E_{kin})$
41	2.65 ± 0.07	49	2.93 ± 0.08	54	3.32 ± 0.05
42	2.24 ± 0.02	50	2.46 ± 0.03	55	2.78 ± 0.02
43	1.91 ± 0.01	51	2.12 ± 0.01	56	2.28 ± 0.01
44	1.67 ± 0.01	52	1.81 ± 0.01	57	1.94 ± 0.01
45	1.49 ± 0.01	53	1.60 ± 0.01	58	1.69 ± 0.01
46	1.32 ± 0.01	54	1.43 ± 0.01	59	1.55 ± 0.01
47	1.26 ± 0.01	55	1.35 ± 0.01	60	1.48 ± 0.01
48	1.25 ± 0.01	56	1.32 ± 0.00	61	1.46 ± 0.01
49	1.23 ± 0.01	57	1.32 ± 0.01	62	1.50 ± 0.01

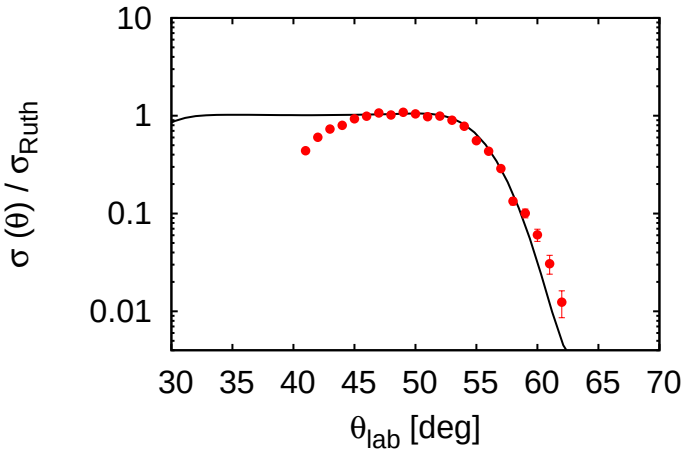

Figure 5.13: The ratio of elastic cross section $\sigma(\theta)$ and the Rutherford cross section σ_{Ruth}. The solid black line is GRAZING calculation. Points are experimental values normalized for all three PRISMA settings separately.

given in Table 5.2, were applied. The elastic cross section extracted in this way is shown in Fig. 5.13 as ratio to the Rutherford cross section (points) in comparison with the results of GRAZING calculations (black line). At more forward angles the elastic cross section is well approximated by the Rutherford scattering thus obtaining the absolute normalization factor (in mb/sr) for all other reaction channels. The pronounced falloff of the elastic cross section for large angles points to the onset of absorption. The discrepancy of the experimental cross section and the calculated one at most forward angles in Fig.

5.13 is ascribed to the inefficient part of the MCP. This behaviour was also observed in the last set of angles, but the effect was reduced by using the angular overlap region.

In this way a conversion of cross sections from [counts] to [mb/sr] can be obtained for each of the PRISMA settings separately. The value of these normalization factors reflects also the duration of measurement at each of the PRISMA angular settings. Normalization factors are for PRISMA at 46°: 1 [mb/sr] = 1322 ± 24 [counts] and for PRISMA at 54°: 1 [mb/sr] = 3139 ± 33 [counts]. Since the last angle, 59°, is in the angular range where absorption becomes more and more important, normalization factor was obtained from the matching with the previous two and the factor was estimated to be 2000 [counts]. In this way beside the determination of the absolute cross sections for other channels, the described procedure allowed us to match for the first time angular distributions obtained with different PRISMA angular settings.

5.5 Differential cross sections

The experimental differential cross sections corrected for the transmission through PRISMA for $(+1n)$ ^{41}Ar and $(-1p)$ ^{39}Cl channels are shown, as selected examples, in Fig. 5.14 together with results from the GRAZING calculation. This was achieved after the transmission factors through PRISMA have been applied as a correction to each experimental differential cross section separately. The absolute differential cross section has been extracted in the following way:

$$\frac{d\sigma}{d\Omega} = \frac{N(E_{kin}, \theta_{lab})}{C} \times f(E_{kin}, \theta_{lab}) \tag{5.8}$$

where $N(E_{kin}, \theta_{lab})$ are experimental data, $f(E_{kin}, \theta_{lab})$ is correction matrix for that channel and C conversion factor from [counts] to [mb/sr] for that angular setting. Experimental angular distributions that are presented in Fig. 5.14 with blue points show how spectrometer mostly affects the borders of the angular range. Only after the distribution was corrected for the transmission one obtained smooth differential cross section.

The $(+1n)$ and $(-1p)$ channels are known to be well reproduced by GRAZING calculations [1]. These one-nucleon transfer channels constitute the building blocks over which are based the calculations for the more complex multinucleon transfer channels. Noteworthy is the fact that good agreement between experiment and theory, both in shape

and magnitude especially at forward angles and near the grazing one, has been achieved. The experimental angular distributions are bell shaped in a narrow angular range centred at the grazing angle. For large scattering angles, larger than quarter points (see also Fig. 5.13), where absorption, due to the reaction channels not explicitly included into calculation, starts to be important, the GRAZING calculations under-predict the data. The similar situation have been observed in previously measured systems, see for example Fig. 6 and 8 of Ref. [30].

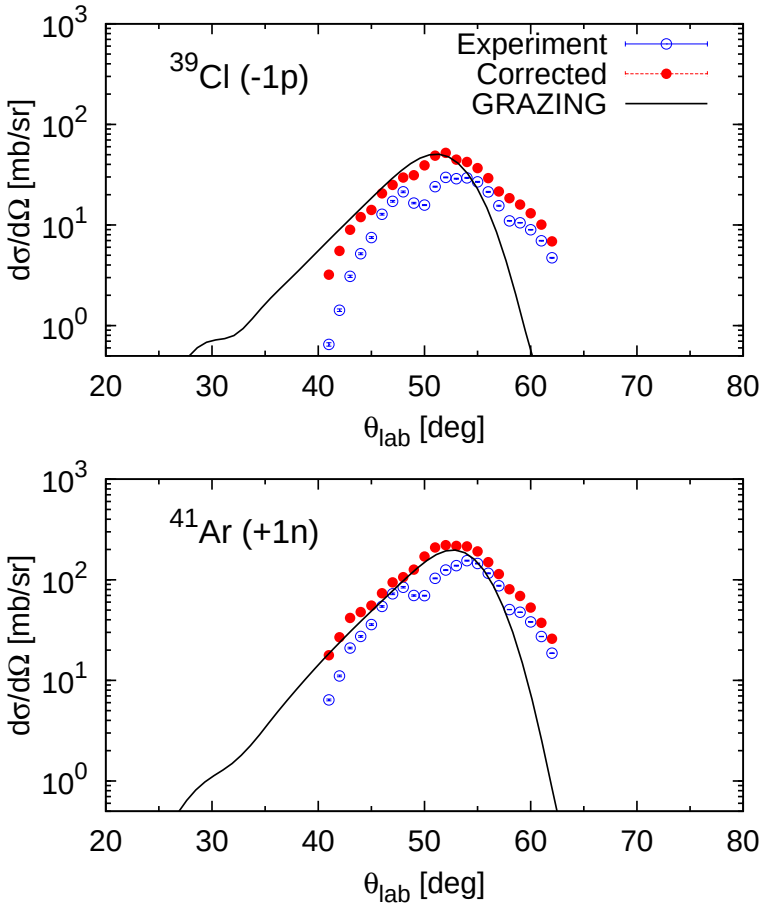

Figure 5.14: Experimental angular distributions for $(+1n)$ and $(-1p)$ for all three PRISMA settings joined together. Experimental angular distributions that are presented with blue points have statistical errors, while corrected distributions presented with red points have quadratic sum of statistical errors and errors induced by the response function. Black line is GRAZING calculation.

The same procedure was repeated for all analysed channels. Figure 5.15 shows these angular distributions for different reaction channels populated in the ^{40}Ar+^{208}Pb reaction. The experimental differential cross sections (the full TKEL range integrated) are presented with black points together with results from GRAZING calculations (black solid line). Comparison with GRAZING calculation will be discussed in Chapter 7. From the grazing

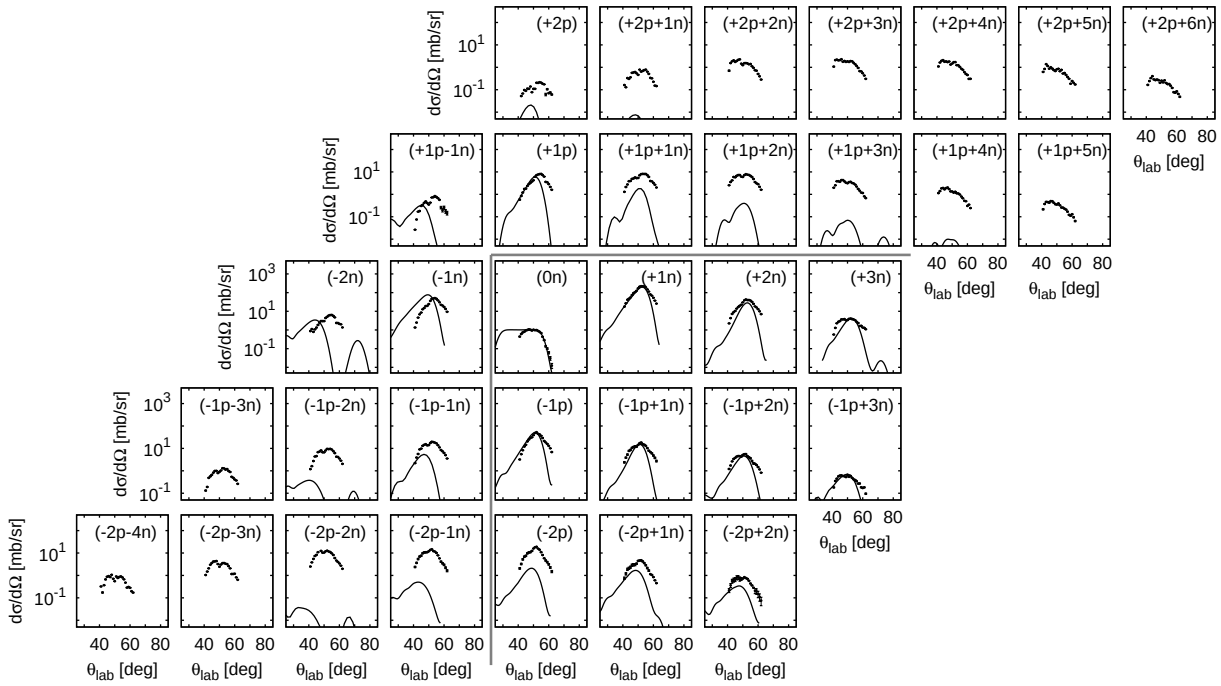

Figure 5.15: The differential cross sections for different reaction channels populated in the ^{40}Ar+^{208}Pb reaction (label in each panel). The experimental, energy integrated, angular distributions are presented with points, while GRAZING calculation is shown with black solid line. Notice that for some channels the GRAZING calculation is much lower than the experimental differential cross sections and is outside the scale.

character of these reactions we know that most of the yield in the different transfer channels is concentrated in a narrow angular range close to the grazing angle with shape of the angular distribution weakly dependant on the isotope. All one nucleon transfer channels show such shape centred at the grazing angle typical for quasi-elastic processes. As more protons are transferred the distribution becomes flatter (see for example Ca isotopes) and starts to lose bell-shape characteristic of QE. With the increase of proton transfers forward part in the angular distribution becomes more and more pronounced and the distribution becomes broader, especially for proton pick-up channels.

In the case of the one proton stripping channels (Cl), the strongest channel corresponds to the pure proton stripping channel (^{39}Cl) as expected from the optimum Q-value considerations, while in the case of the one proton pick-up channels (K), $(+1p)$, $(+1p+1n)$ and $(+1p+2n)$ channels are of similar strength (see Fig. 5.16). This may indicate the importance of additional degrees of freedom. One of such degrees of freedom can be a transfer of a correlated neutron-proton pair. Of course, the influence of other reaction mechanism can affect the cross section. Thus special care has been taken in detailed

analysis of total kinetic energy losses for these channels (see sections 5.2 and 5.3) and two angular distributions have been separated.

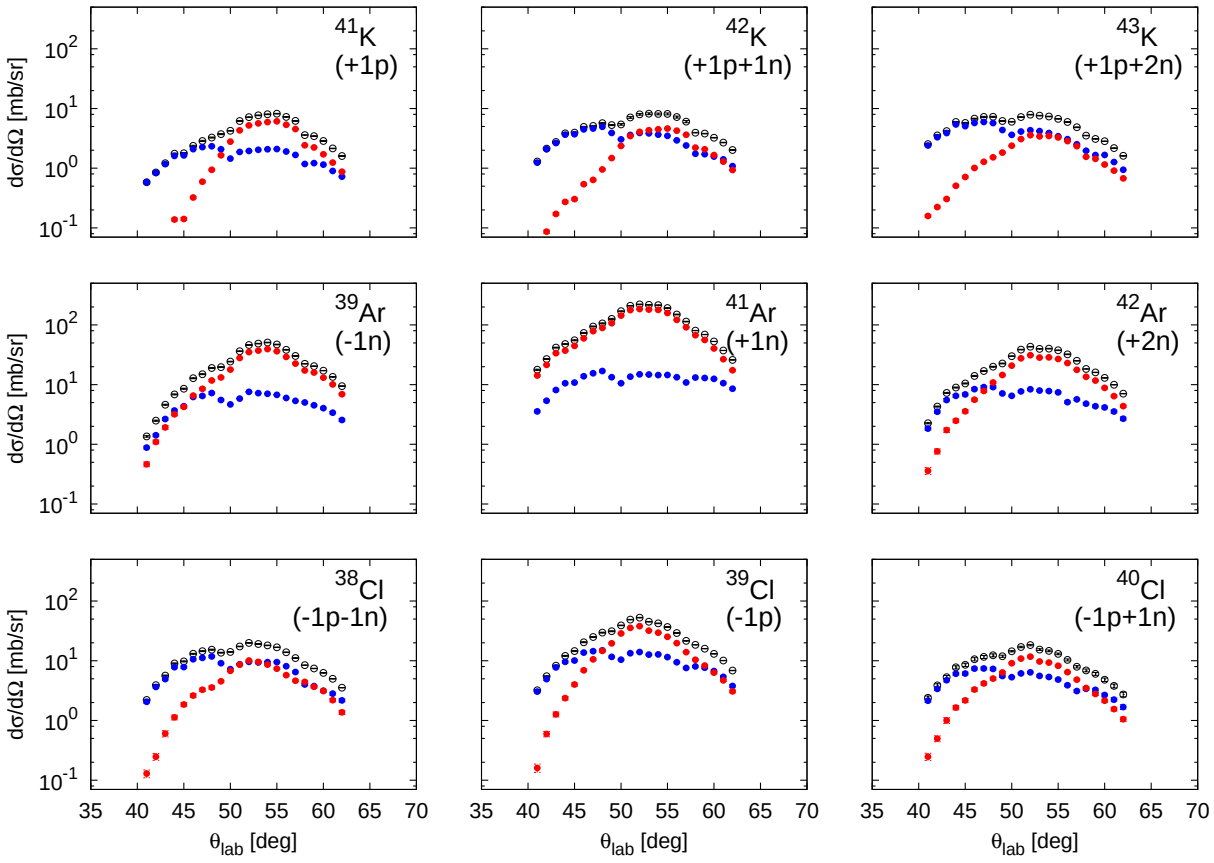

Figure 5.16: The differential cross sections for different reaction channels (label in each panel): integrated over entire TKEL (black points), integrated over lower TKEL part (red points) and integrated over higher TKEL (blue points).

Angular distribution for different reaction channels populated in the ^{40}Ar+^{208}Pb reaction integrated over entire TKEL (presented with black points), integrated over lower TKEL (red points) and over higher TKEL part (blue points) are presented together in Fig. 5.16. It is important to notice that differential cross sections represented with red points have bell shaped angular distributions typical for QE processes with maximum around grazing angle. Also the matching of three different PRISMA settings is much better in this case, in the sense that there is less "waiving". The angular distributions connected with the large TKEL are much flatter, the bell-shape is lost and the fluctuations are more pronounced. This is due to DIC, where these fluctuations result from energy cuts of the spectrometer since the energy acceptance is $\approx \pm 20\%$.

5.6 Total cross sections

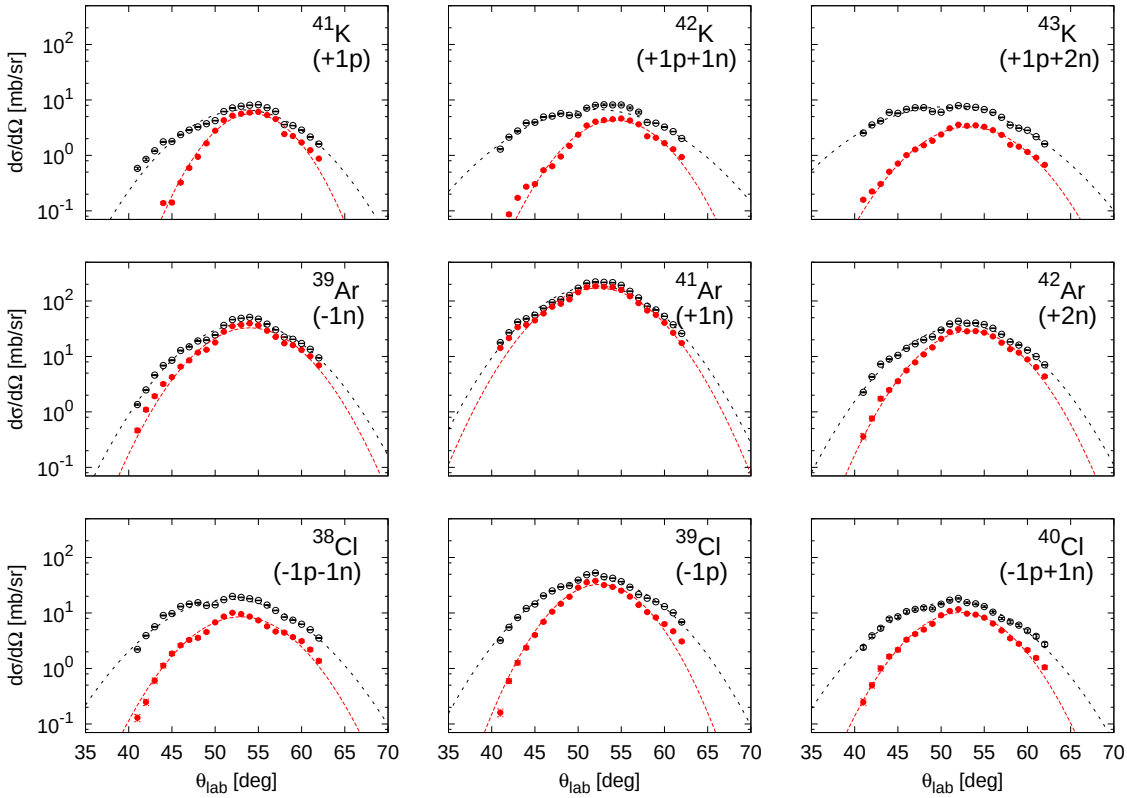

Figure 5.17: Angular distribution integrated over entire energy range (black points) and QE component (red points). The Gaussian fit used to extract total cross section of both is shown with lines.

The angular distributions span the angular range larger than $\Delta\theta = 20°$. This range covers most of the transfer strength and thus the total cross section can be extracted for different reaction channels. The total cross sections have been obtained by integrating angular distributions. The example of such integration with the Gaussian fit is shown in Fig. 5.17 with the total cross section obtained as:

$$\sigma = \int \left(\frac{d\sigma}{d\Omega}\right) d\Omega = 2\pi \int \left(\frac{d\sigma}{d\Omega}\right) sin\theta d\theta. \tag{5.9}$$

Figure 5.18 shows experimental total cross sections for indicated channels obtained by integration over entire TKEL (grey histogram) and by integration of the low TKEL part (red histogram). The cross sections are also listed in Table 5.3.

Neutron pick-up channels follow the smooth trend observed also in other experiments,

with similar average decrease for each transferred nucleon [1]. The $(+1n)$ channel is the strongest channel observed and it is followed by $(-1p)$. It may be interesting to notice that the strength of the $(-1p)$ channel is very similar to the strength of the $(+2n)$ (observed also in numerous previous experiments). Notice also that the total cross section is not symmetric around the projectile nucleus, the $(+1n)$ channel is $\sim$5 times stronger than the $(-1n)$ channel, and the $(-1p)$ is $\sim$6 times stronger than the $(+1p)$ channel.

For two proton stripping channels one observes a drift toward lower masses which in part can be attributed to neutron evaporation. On the other side, for the two proton pick-up channels the shift is on the neutron pick-up side, a fact which cannot be explained through the neutron evaporation process.

Total cross sections obtained in this way will be compared with the semi-classical model GRAZING in Chapter 7 in order to better understand presented results.

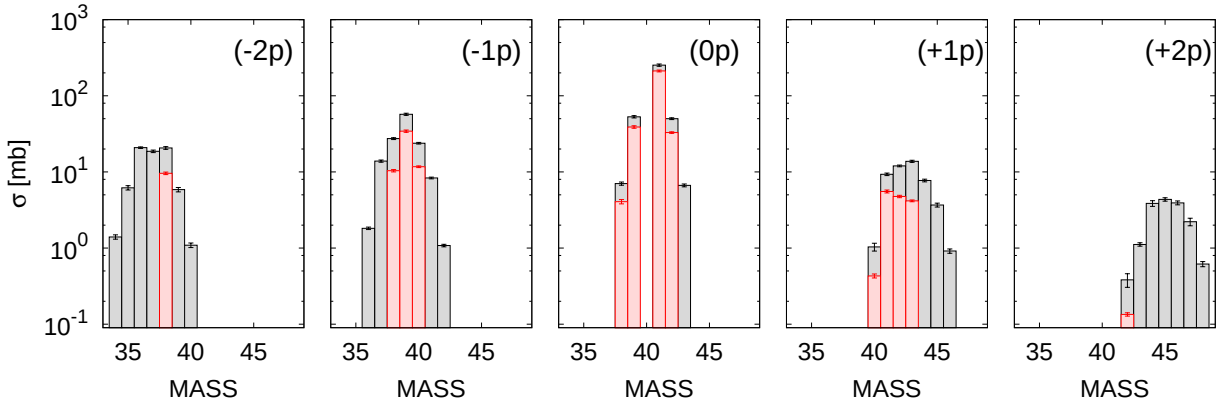

Figure 5.18: The inclusive total cross sections integrated over total energy loss (grey histogram). For some channels, the integration over the QE part of TKEL is added (red histogram). Errors are statistical, and also include transmission factors and conversion factor errors. See also Table 5.3.

The ratio of QE component of cross section and total cross section for several representative channels is shown in Fig. 5.19. The contribution of QE component in total cross section is, as expected, larger for neutron transfers. It is seen that the ratio drops as we move further away from the projectile nuclei, particularly for proton transfers. The contribution of QE process for both one proton pick-up and one proton stripping is the same, and around $\sim$60%, which may be an indication of correct extraction of QE component.

Table 5.3: Angle and energy integrated experimental cross section, σ_{exp}, and cross section integrated over low energy, σ_{expQE}, for different (Z, A) channels. The cross sections have been obtained for all PRISMA settings joined together and integrated. Errors are statistical, and also include transmission factors and conversion factor errors.

Z	**A**	σ_{exp} **[mb]**	σ_{expQE} **[mb]**
16	34	1.40 ± 0.09	
	35	6.2 ± 0.4	
	36	20.8 ± 0.5	
	37	18.6 ± 0.7	
	38	20.7 ± 0.8	9.6 ± 0.4
	39	5.9 ± 0.4	
	40	1.1 ± 0.1	
17	36	1.82 ± 0.07	
	37	13.9 ± 0.5	
	38	27.4 ± 0.8	10.4 ± 0.4
	39	57 ± 2	34 ± 1
	40	23.8 ± 0.6	11.7 ± 0.3
	41	8.3 ± 0.2	
	42	1.08 ± 0.04	
18	38	7.0 ± 0.3	4.1 ± 0.3
	39	53 ± 2	39 ± 1
	40		
	41	253 ± 8	212 ± 6
	42	50 ± 1	32.9 ± 0.7
	43	6.7 ± 0.3	
19	40	1.0 ± 0.1	0.43 ± 0.03
	41	9.3 ± 0.4	5.5 ± 0.2
	42	12.0 ± 0.3	4.8 ± 0.2
	43	13.8 ± 0.5	4.2 ± 0.1
	44	7.7 ± 0.3	
	45	3.7 ± 0.2	
	46	0.91 ± 0.06	
20	42	0.38 ± 0.08	0.135 ± 0.007
	43	1.12 ± 0.06	
	44	3.9 ± 0.3	
	45	4.4 ± 0.2	
	46	3.9 ± 0.2	
	47	2.2 ± 0.3	
	48	0.62 ± 0.05	

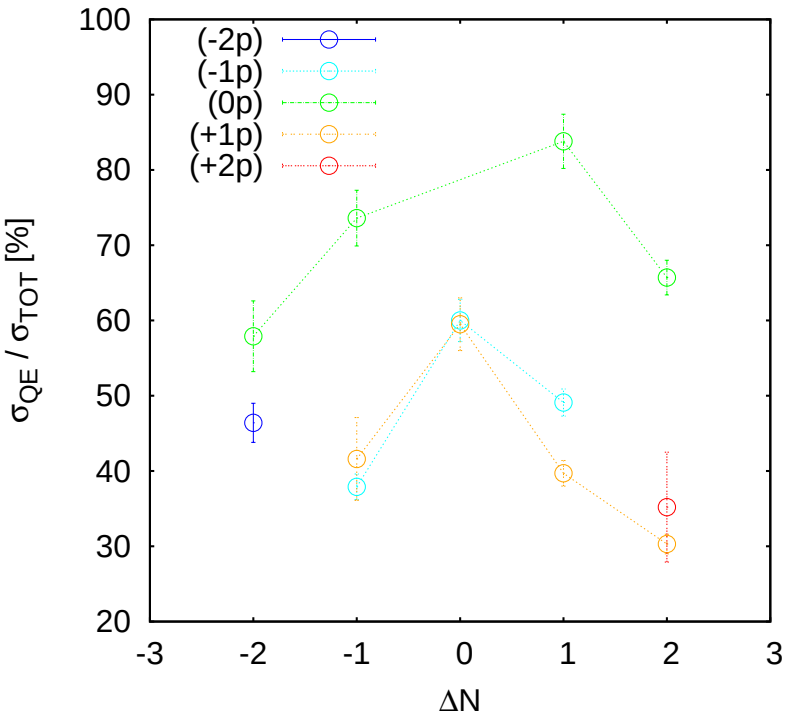

Figure 5.19: Ratio of QE component of cross section and total cross section.

6 The PRISMA spectrometer coupled to the CLARA array

The coupling of the PRISMA spectrometer with the CLARA array allowed to fully identify reaction products and to attribute to each of them its characteristic γ-ray spectra. This gives the possibility to identify individual transitions and excited states, their population pattern and decay modes. Gamma spectra and level schemes of channels relevant for this work, with emphasis on the (np) correlations, will be presented in this Chapter.

6.1 Fragment-γ coincidences

The constituents of the heavy-ion collision may exchange many nucleons, thus providing information on the contribution of single particle and correlated particle transfer, and also on the contribution of surface vibrations (bosons) and their coupling with single particles (fermions). The analysis and interpretation of results of heavy-ion transfer reactions can be quite complex because the informations about correlations are often hidden in the inclusive character of the extracted cross sections. One of the possibilities to distinguish excited states is the coincident detection of γ rays. It has been demonstrated that grazing reactions favour a certain degree of selective population of states associated with specific excitation energy, angular momenta or with specific structural properties [84]. The population pattern of these individual states provides important complementary information for the reaction mechanism studies and in particular for correlation studies, as the short-range pairing interaction redistributes the transfer strength over the different final states. We will study in more details if the transfer flux will enhance some specific states, and we will try to connect the underlying structure of such states with the transfer mechanism.

The γ rays detected in coincidence with the relevant transfer channels studied in the ^{40}Ar+^{208}Pb reaction should provide quantitative information to establish possible decay

modes related to the population of specific nuclear states. In this section we will search for this selective population and concentrate on the distribution of transfer flux over different populated states in several channels relevant for (np) correlations. In particular we will present spectra of the $(+1n)$, $(+1p)$, $(+1p+1n)$ and $(+1p+2n)$ channels. We will concentrate on the strongest transitions whose structure is relevant for reaction mechanism study. Similar structure is expected in similar transfer channels (i.e one or two nucleon transfer channels) and, where possible, comparison will be made with shell model calculations.

The shell model calculations have been performed using the most recent $sd-pf$ residual interaction (SDPF-U) [85]. The valence space for the protons includes the full sd shell, covering from $Z=8$ to $Z=20$, while for the neutrons it includes the full sd and pf shell, from $N=8$ to $N=40$. We remind that below $N=20$ these calculations reduce to the pure sd shell. Thus, the shell model calculations are unrestricted in the full sd shell for protons and the full pf shell for neutrons.

In addition, the analysis of Doppler corrected γ transitions of the heavy partners associated to each A and Z detected in PRISMA will help to evaluate the contribution of evaporation processes.

6.1.1 The $(+1n)$ channel, ^{41}Ar

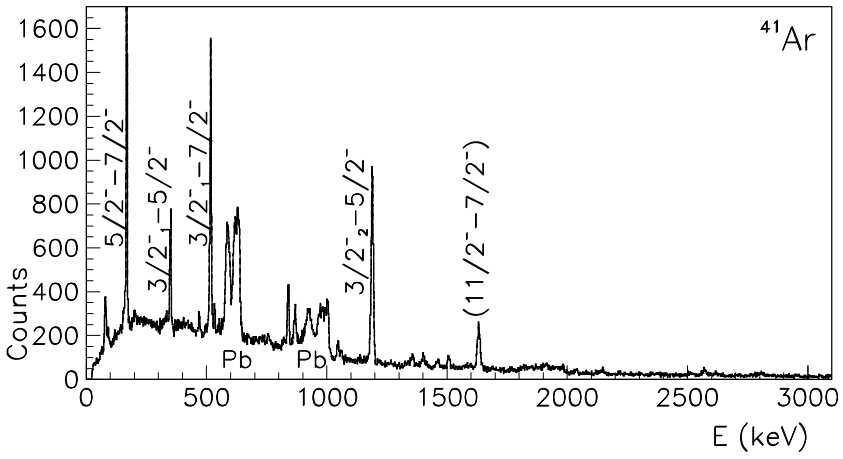

Figure 6.1: The ^{41}Ar γ spectrum. The strongest transitions are labelled with spin and parity of initial and final states.

The γ spectrum of ^{41}Ar, the one-neutron pick-up channel, is presented in Fig. 6.1. Experimentally observed levels and intensities of the observed transitions are listed in

Table 6.1: Experimentally observed levels and intensities of the populated excited states, I^{EXP}, for ^{41}Ar. The intensities have been obtained by subtractions of the feeding from above in agreement with the level scheme presented in Fig. 6.2.

Isotope	E_{level} [keV]	J_i^π	I^{EXP} [%]
^{41}Ar	516	$3/2^-$	21
	1035	$3/2^+$	20
	1354	$3/2_2^-$	100
	1505	$9/2^-$	7
	1630	$11/2^-$	27
	1870	$1/2^+$	7
	2398	$1/2^-$	7

Tab. 6.1. The level scheme of ^{41}Ar is displayed in Fig. 6.2. The strongest populated state is the negative parity low-lying $3/2_2^-$ state at 1.35 MeV. When compared with the shell model wave functions this state turned out to have a pronounced single-particle character. We constructed strength functions in the framework of shell model by using Lanczos method and pivot states that corresponds to the creation of neutron in $p_{1/2}$, $p_{3/2}$, $f_{7/2}$ and $f_{5/2}$ on the 0^+ ground state of ^{40}Ar [86, 87]. These strength functions clearly display a concentration of single-particle strength in $3/2_2^-$ state of ^{41}Ar [2]. The large part of the $0^+ \otimes f_{7/2}$ strength is in the ^{41}Ar ground state, while the $0^+ \otimes f_{5/2}$ component is in the $5/2^-$ states with excitation energies of $\sim$5-6 MeV. Thus, the strongest excited low-lying state is the state with the pronounced single-particle character.

In addition to the adopted γ transitions of the low-lying states, a strong line at 1629.7(3) keV was observed and attributed to the population of the yet unknown $11/2^-$ state [2]. As already mentioned, the $7/2^-$ ground state of ^{41}Ar can be understood as $0^+ \otimes f_{7/2}$. By coupling this particle state with the 2^+ of ^{40}Ar, one expects a multiplet of states ($3/2^-$, ..., $11/2^-$). The reaction mechanism does not populate the components of the multiplet uniformly but favours the high-spin stretched configuration. At low bombarding energies, where the relative velocity of the two ions is much smaller than the intrinsic velocity of the transferred nucleon, the transfer process maximizes the transferred angular momentum to allow a good matching between the orbital angular momentum of the involved states. Thus the transition at 1629.7 keV was interpreted as the decay from the $11/2^-$ to the ground state. We populate significantly the $11/2^-$ state, with about one-third of the strength of the strongest populated single-particle state. As discussed before, for the $11/2^-$ state the shell model strength function calculations point to a large

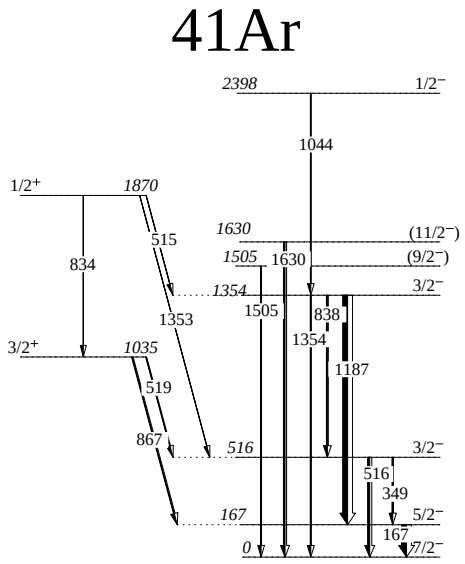

Figure 6.2: The experimental level scheme of ^{41}Ar, populated via the $(+1n)$ channel. Relative γ-ray intensities are indicated by the width of the arrows. Only γ transitions observed in our measurement are plotted. The energy, spin and parity of levels, their branching ratios and energy of transitions, if known, are as in Nuclear Data Sheets [88]. The intensity of each transition was corrected for the efficiency of CLARA.

concentration of 2^+ of ^{40}Ar coupled to the valence neutron in $f_{7/2}$.

The negative parity states take about 86% of the total flux, while the positive parity states have about 14% of the total flux. It can be noticed that the negative parity low-lying $3/2^-_2$ state at 1.35 MeV, with a pronounced single-particle character, is strongly populated. In fact, about 53% of the total flux is in this state. Also, one observes strong population of states that can be explain as coupling of single-particle degrees of freedom to nuclear vibration quanta, which is essential for the description of many basic states in the vicinity of closed shells [2].

6.1.2 The $(+1p)$ channel, ^{41}K

Mass spectra for potassium isotopes are shown in Fig. 6.3 for PRISMA alone and in coincidence with the γ-array CLARA. The main difference is exactly in the $(+1p)$ channel which is more pronounced in the PRISMA alone distribution, showing the importance of the ground-to-ground state population in this channel. This agrees with the TKEL spectra shown in Fig. 6.4, which clearly displays that for the $(+1p)$ channel the most of the transfer flux is concentrated close to the ground-to-ground state. As one adds

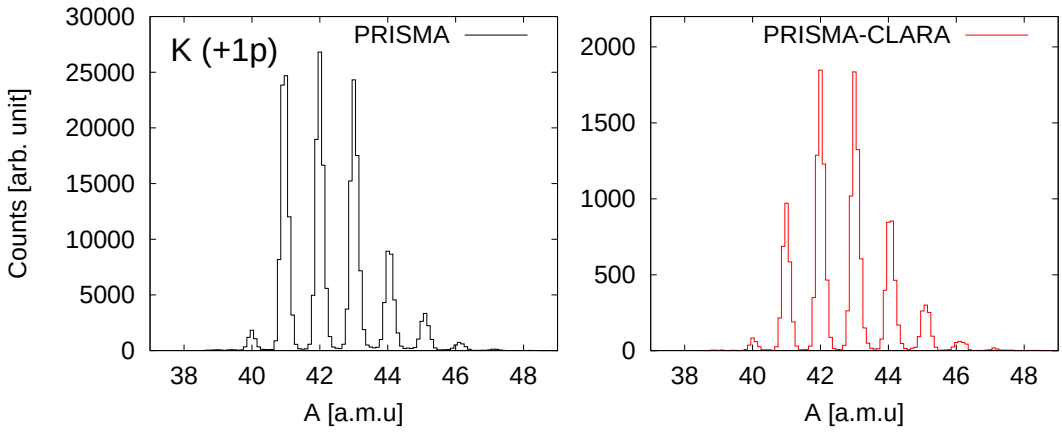

Figure 6.3: Mass spectrum for potassium isotopes. Black line shows PRISMA only distribution, while the red one has a coincidence with γ rays in CLARA.

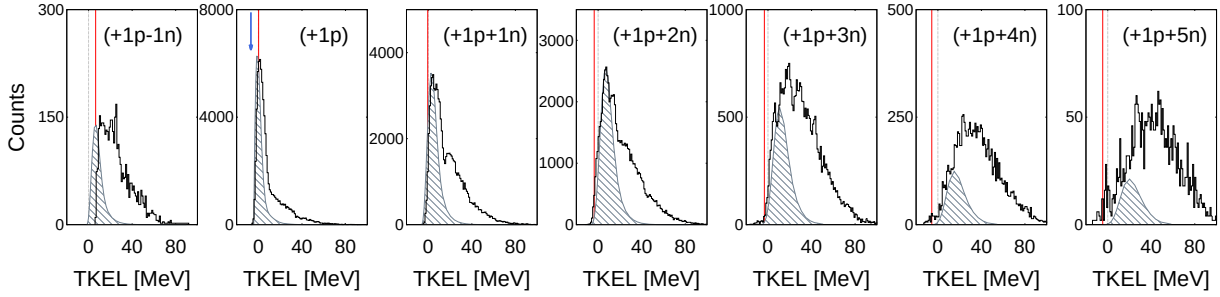

Figure 6.4: Experimental TKEL distribution for K isotopes for PRISMA positioned at 54°. Red vertical line indicates position of the ground-to-ground state Q-value, Q_{gs}, while blue arrow is the optimum Q-value. The shaded grey area is TKEL distribution calculated by GRAZING.

more neutrons, TKEL spectra display large contribution of DIC components and the relative yields of these more neutron-rich potassium isotopes do not depend strongly on coincidence with γ rays. The γ spectra for odd-even and odd-odd isotopes are given in Fig. 6.5.

First we will look at the pure one proton pick-up channel leading to ^{41}K ($Z = 19, N = 22$). Experimentally observed levels and intensities of the populated excited states are listed in Tab. 6.2. The level scheme is displayed in Fig. 6.6. What can be seen is that about 52% of the total flux goes to the negative parity states, while 48% goes to the positive (natural parity states). The strongest observed populated state is the $11/2^-$ state at 2.8 MeV. In principle, this spin and parity can be formed as 2^+ in ^{40}Ar ($Z = 18, N = 22$) coupled to the proton promoted in the $f_{7/2}$ orbital (stretched configuration), similar to $11/2^-$ in ^{41}Ar with the coupling to the neutron in $f_{7/2}$.

Concerning the positive (natural parity) states, the strongly populated states $3/2^+$,

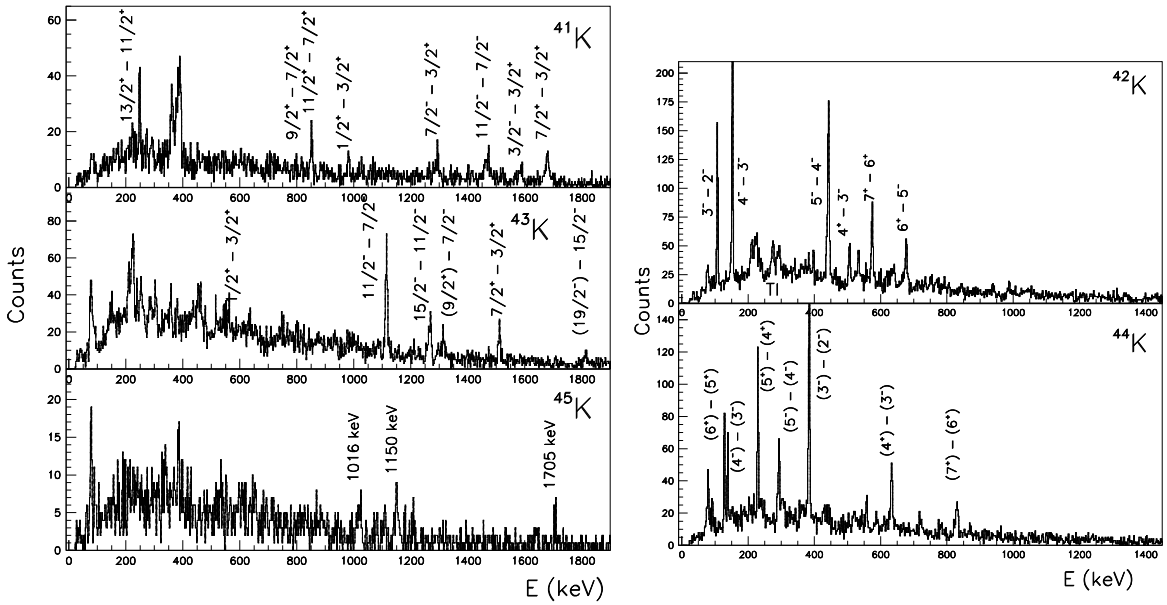

(A) Odd-even K isotopes.

(B) Odd-odd K isotopes.

Figure 6.5: Gamma spectra for different K isotopes.

Table 6.2: Experimentally observed levels and intensities of the populated excited states, I^{EXP}, for ^{41}K. The intensities have been obtained by subtractions of the feeding from above in agreement with the level scheme presented in Fig. 6.6. The intensity of each transition was normalized to the strongest transition.

Isotope	E_{level} [keV]	J_i^π	I^{EXP} [%]
^{41}K	1560	$3/2^+$	43
	1677	$7/2^+$	2
	2144	$5/2^+$	24
	2495	$9/2^+$	60
	2528	$11/2^+$	23
	2774	$13/2^+$	61
	1582	$3/2^-$	96
	2317	$5/2^-$	35
	2762	$11/2^-$	100

$5/2^+$, $9/2^+$, $11/2^+$ and $13/2^+$ have one dominant component in the SM wave function ($\sim$80%) $\pi(d_{5/2})^6(s_{1/2})^2(d_{3/2})^3 \otimes \nu(f_{7/2})^2$. The only state of this yrast sequence, with similar wave functions, which we didn't directly populate, is $7/2^+$. Thus, we observed strong excitation of natural parity yrast states. In addition, half of the total flux is in the negative parity states, of which the strongest one is $11/2^-$.

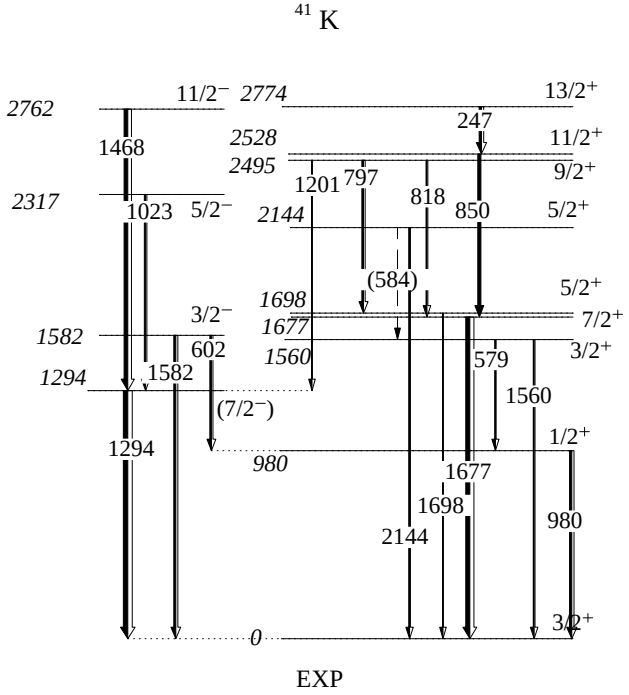

Figure 6.6: The experimental level scheme with positive and negative parity level scheme of ^{41}K, populated via $(+1p)$ channel. Relative γ-ray intensities are indicated by the width of the arrows. Only transitions observed in our measurement are plotted. The energy, spin and parity of levels, their branching ratios and energy of transitions, if known, are as in Nuclear Data Sheets [88]. The intensity of each transition was corrected for the efficiency of CLARA.

6.1.3 The $(+1p+1n)$ channel, ^{42}K

The γ spectrum of the $(+1p+1n)$ channel leading to ^{42}K is shown in Fig. 6.5B. The odd-odd nucleus ^{42}K ($Z = 19, N = 23$) has a rather high level density which makes the study of the properties of these levels rather difficult. The corresponding experimental level scheme is presented in Fig. 6.7. Experimental intensities of the strongly populated excited states, I^{EXP}, are listed in Tab. 6.3.

About 61% of the total flux goes to the negative (natural) parity states, while 39% goes to the positive parity states. Low-lying negative parity states, 3^- at 0.6 MeV and 5^- at 0.7 MeV, are strongly populated. The dominant component ($\sim$70%) of the wave function of these low-lying negative parity states is: $\pi(d_{5/2})^6(s_{1/2})^2(d_{3/2})^3 \otimes \nu(f_{7/2})^3$.

In the positive parity band the strongest populated state is 7^+ state at 2 MeV with about 74% (or about 16% of the total flux). The structure of 7^+ state according to Ref. [89] can be viewed as stretched configuration of a proton and a neutron in the $f_{7/2}$ orbital.

Table 6.3: Experimentally observed levels and intensities of the populated excited states, I^{EXP}, for ^{42}K. The intensities have been obtained by subtractions of the feeding from above in agreement with the level scheme presented in Fig. 6.7. The intensity of each transition was normalized to the strongest transition.

Isotope	E_{level} [keV]	J_i^π	I^{EXP} [%]
^{42}K	258	4^-	20
	639	3^-	100
	699	5^-	90
	841	3^-	28
	1144	4^+	32
	1947	7^+	74

The corresponding $E_\gamma = 572$ keV depopulating the 7^+ state can be seen in Fig. 6.5B.

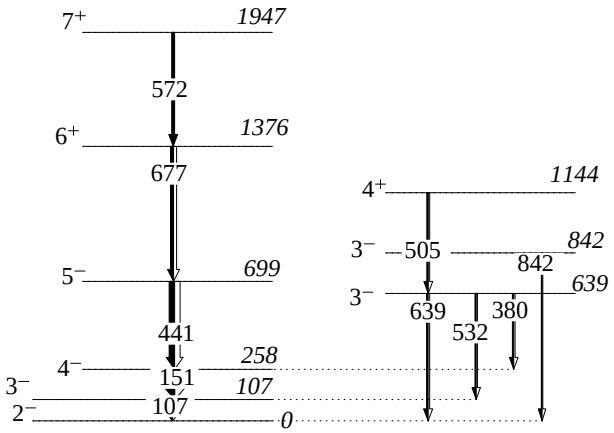

Figure 6.7: The experimental level scheme of ^{42}K, populated via $(+1p+1n)$ channel, showing most intense transitions. Relative γ-ray intensities are indicated by the width of the arrows. Only levels of significant strength are shown. The intensity of each transition was corrected for the efficiency of the γ-array.

We can conclude that the γ spectrum of ^{42}K shows the population of the low-lying negative parity states and the population of the higher-lying positive parity states. The structure of low-lying negative parity states can be viewed as a multiplet arising from the coupling of the unpaired proton in the $d_{3/2}$ and the unpaired neutron in the $f_{7/2}$ orbital. Positive parity states can be explained as the excitation of the proton to the $f_{7/2}$ orbital and its coupling to the unpaired neutron in the same orbital. This strong population of the state with such structure may be important for neutron-proton correlation.

We will profit from the weak-coupling method calculation performed in the framework of the Bansal-French-Zamick. This model is based on the calculation of the binding energies of the particle-hole states and taking into account the known excitation energies

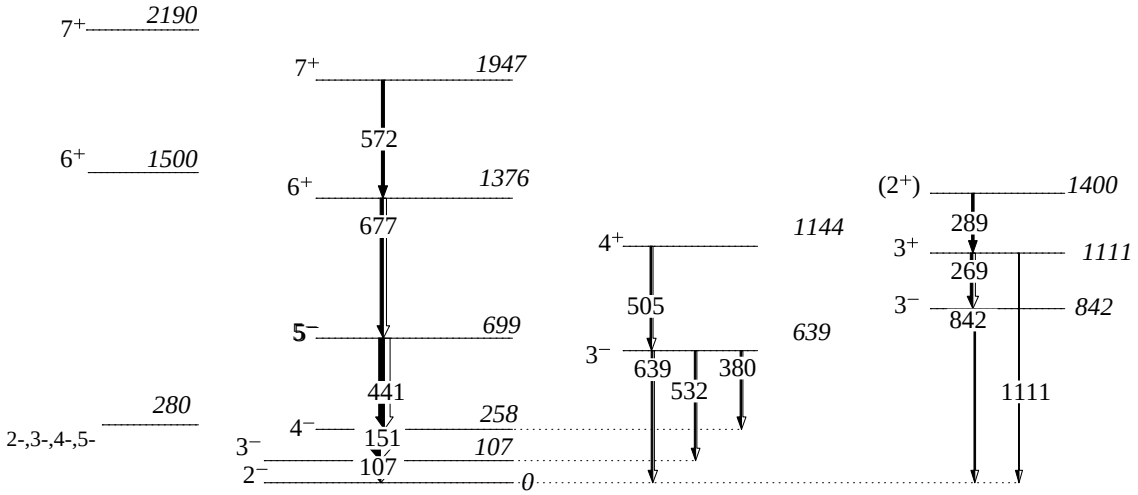

Figure 6.8: Populated levels of ^{42}K, with weak-coupling calculations (left) for the degenerate multiplet 2^-, 3^-, 4^- and 5^- and 6^+ and 7^+ states.

of the relevant states. In more details, the 6^+ and 7^+ configurations are considered as the promotion of a proton from the $d_{3/2}$ to the $f_{7/2}$, and (stretched) coupling to an uncoupled neutron in $f_{7/2}$. The energy differences between the 6^+ and 7^+ states in ^{42}K and ^{44}Sc isotons thus have to be the same. By taking the experimental excitation energies for ^{38}Ar(0^+), ^{44}Sc(6^+) and ^{44}Sc(7^+) together with the empirical fit to a number of particle-hole states in the ^{40}Ca region, the binding energy of 7^+ turned out to be -14.83 MeV. The natural parity quadruplet $\pi(d_{5/2})^6(s_{1/2})^2(d_{3/2})^3 \otimes \nu(f_{7/2})^3$ with 2^-, 3^-, 4^- and 5^- is degenerate in this weak-coupling model and is calculated at -16.74 MeV with respect to ^{40}Ca ground state. Considering the experimentally averaged excitation energy of the 2^-, 3^-, 4^- and 5^- levels, the 7^+ state is placed at 1.91 MeV excitation energy [90]. The corresponding levels are plotted in Fig. 6.8 and show good agreement with experimental ones.

The obtained results can be compared with the ^{42}K observed in the ^{40}Ca+^{96}Zr reaction via stripping of one proton and pick-up of three neutrons. The comparison presented in Fig. 6.9 shows that all strong γ lines are observed in both measurements. However, relative strength of these γ lines is significantly different. The $E_\gamma = 572$ keV depopulating the 7^+ state is much more enhanced in the ^{40}Ar+^{208}Pb system (top panel of Fig. 6.9).

The comparison of strength of states populated in ^{42}K for both reactions is given in Fig. 6.10. All values are normalized to the lowest lying 151 keV γ-ray depopulating the 4^- level, that has a similar strength in both experiments. While for the $(-1p+3n)$ channel in ^{40}Ca+^{96}Zr a similar strength of all populated states is observed, in the $(+1p+1n)$

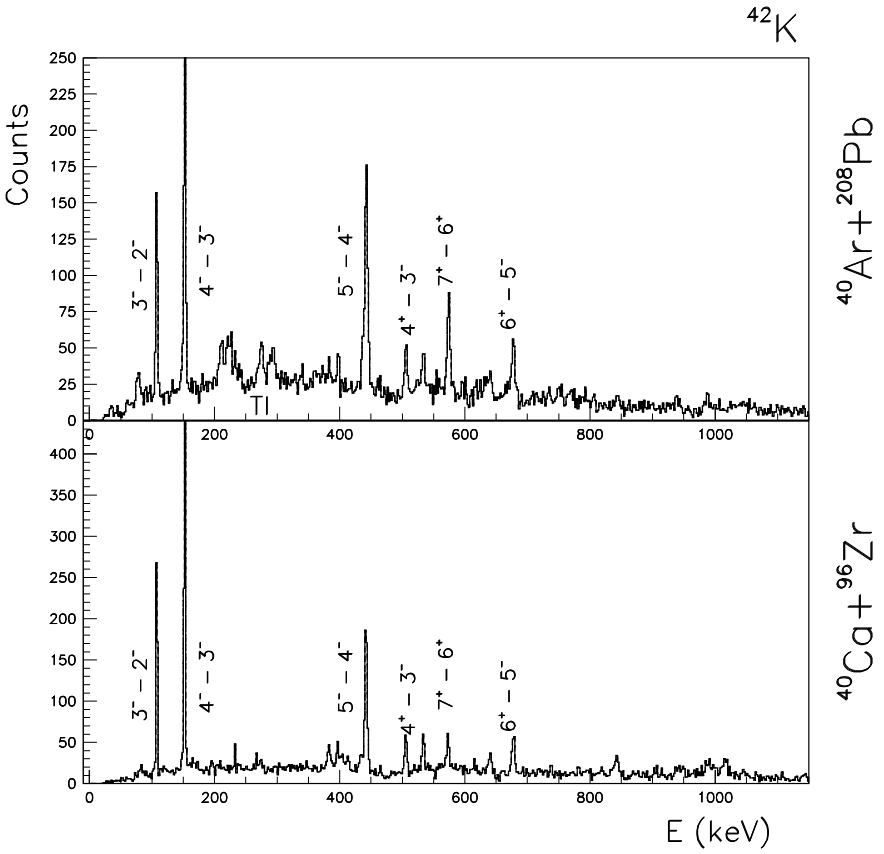

Figure 6.9: Comparison for ^{42}K measured in ^{40}Ca+^{96}Zr and ^{40}Ar+^{208}Pb.

channel in ^{40}Ar+^{208}Pb a more selective population has been evidenced.

Results were compared in the same way with ^{4}He+^{40}Ar leading to ^{42}K (see Fig. 6.10 bottom panel). In this deuteron transfer reaction the strong population of 7^+ has been observed [91]. This reaction is very selective and 7^+ is by far the strongest populated state.

A comparison of the TKEL spectra for the K isotopes obtained in three different reactions, ^{40}Ar+^{208}Pb, ^{40}Ca+^{96}Zr and ^{40}Ca+^{208}Pb, is shown in Fig. 6.11. They are plotted as $E^* = TKEL + Q_{gs}$, i.e. the ground-to-ground state Q_{gs} was taken into account for the easier direct comparison of systems. The energy for the ^{40}Ca+^{96}Zr system was about 10% above the Coulomb barrier, while in other system, ^{40}Ar+^{208}Pb, was about ∼30%. In the case of ^{40}Ca+^{96}Zr, the K isotopes were reached via $(-1p \pm xn)$ channels, while for the ^{40}Ar+^{208}Pb via $(+1p \pm xn)$. For TKEL measured in the ^{40}Ca+^{96}Zr system, only the TKEL of the pure $(-1p)$ channel has a pronounced low-energy peak, centred at the ground-to-ground state equivalent. Other channels, when neutrons are added, have

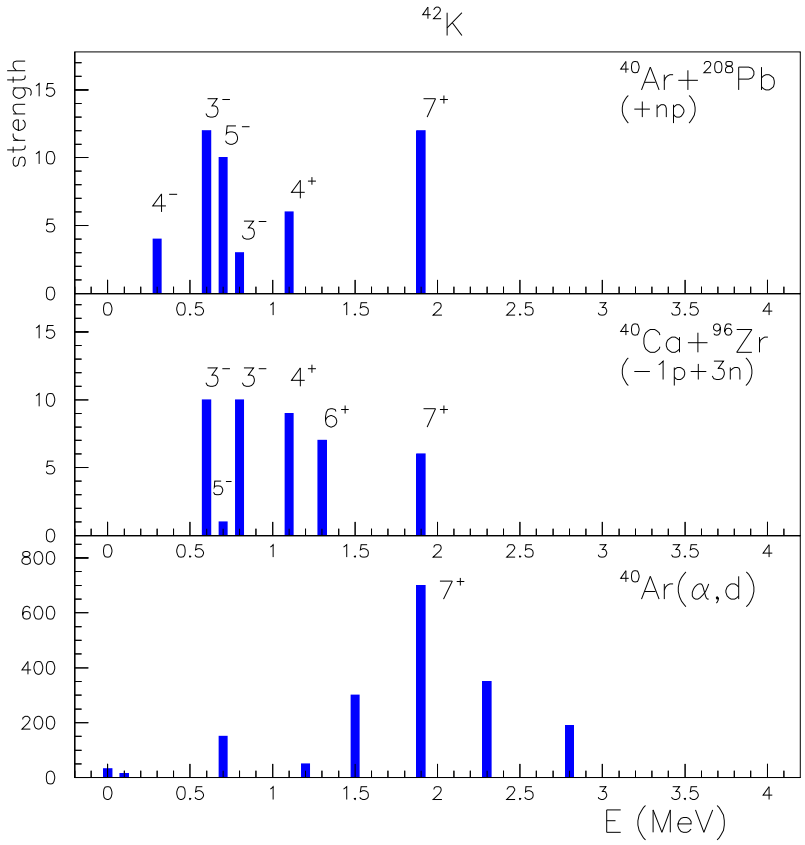

Figure 6.10: Comparison of the intensity of the populated excited states i.e. the experimental strength functions (SF) of the states populated in ^{42}K measured in ^{40}Ar+^{208}Pb (top panel), ^{40}Ca+^{96}Zr (middle) and ^{4}He+^{40}Ar (bottom). They were obtained from the intensity of γ transitions corrected by the efficiency of CLARA for that energy. In the construction of these strengths all γ transitions depopulating a certain state are taken into account together with the feeding from above in agreement with the level schemes. Values in first two panels are normalized to the lowest-lying 151 keV γ-ray depopulating the 4^- level, that has a similar strength in both experiments. Feeding from above to the 7^+ state was not taken into account in strength function construction. Even if we take into account also this transition, the main conclusion of the population of 7^+ state will remain.

similar shape with centroids located at larger energy losses. In the case of ^{40}Ar+^{208}Pb, due to the higher energy, the TKEL extended to large energy losses, but still kept the low-energy peak close to the ground-to-ground state transitions. The peak-like structure centred at large losses agrees better with the centroids in the TKEL obtained in the ^{40}Ca+^{96}Zr reactions. In general, such shapes of TKEL agree well with the observation of the dominant states populated in the, for example, ^{42}K. In the reaction where the centroid of the TKEL is at the larger energy losses, the strength of the populated states is more or less equal, without some preferred population of the state of the specific structure (beside

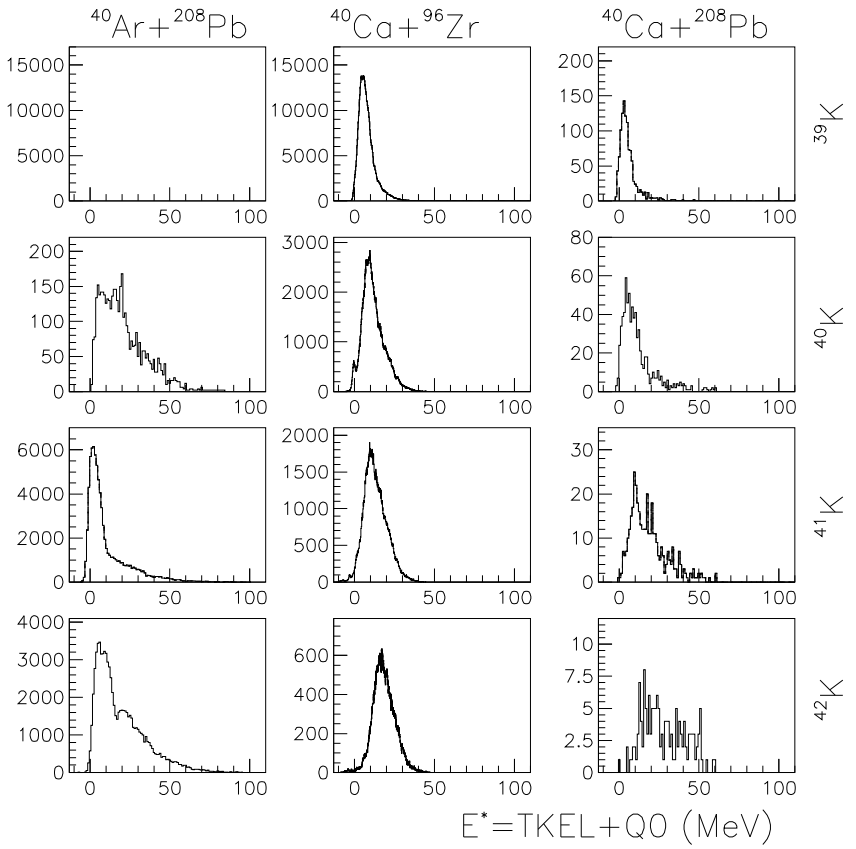

Figure 6.11: Comparison of the TKEL spectra for the K isotopes obtained in three different reactions, ^{40}Ar+^{208}Pb, ^{40}Ca+^{96}Zr and ^{40}Ca+^{208}Pb.

the preference for large angular momentum transfer). Such behaviour can be connected with the DIC-like reactions. In the case of the ^{40}Ar+^{208}Pb reaction, the distribution of the strength over the excited states is not uniform (as, in fact, one would expect form the "direct quasi-elastic" reaction). The last set of panels on the right present energy distribution for ^{40}Ca+^{208}Pb measured close to the barrier, which is included for completeness. Although, the statistic for these channels is quite low, behaviour is similar to the ^{40}Ca+^{96}Zr system.

6.1.4 The $(+1p+2n)$ channel, ^{43}K

Experimentally observed levels and intensities of the populated states of ^{43}K ($Z = 19, N = 24$) are listed in Tab. 6.4 and displayed in Fig. 6.12. The positive (natural) parity states take about ∼59% of the total flux, while ∼41% goes to negative parity states. What can be seen is that the most intense state is $7/2^+$. It is followed by a strongest

Table 6.4: Experimentally observed levels and intensities of the populated excited states, I^{EXP}, for ^{43}K. The intensities have been obtained by subtractions of the feeding from above in agreement with the level scheme presented in Fig. 6.12. The intensity of each transition was normalized to the strongest transition.

Isotope	E_{level} [keV]	J_i^π	I^{EXP} [%]
^{43}K	561	$1/2^+$	22
	738	$7/2^-$	34
	975	$3/2^-$	19
	1027	$5/2^+$ or $7/2^+$	34
	1510	$7/2^+$	100
	1550	$5/2^+$ or $3/2^+$	52
	1850	$11/2^-$	50
	2048	$9/2^+$	45
	3115	$15/2^-$	32
	4928	$19/2^-$	43

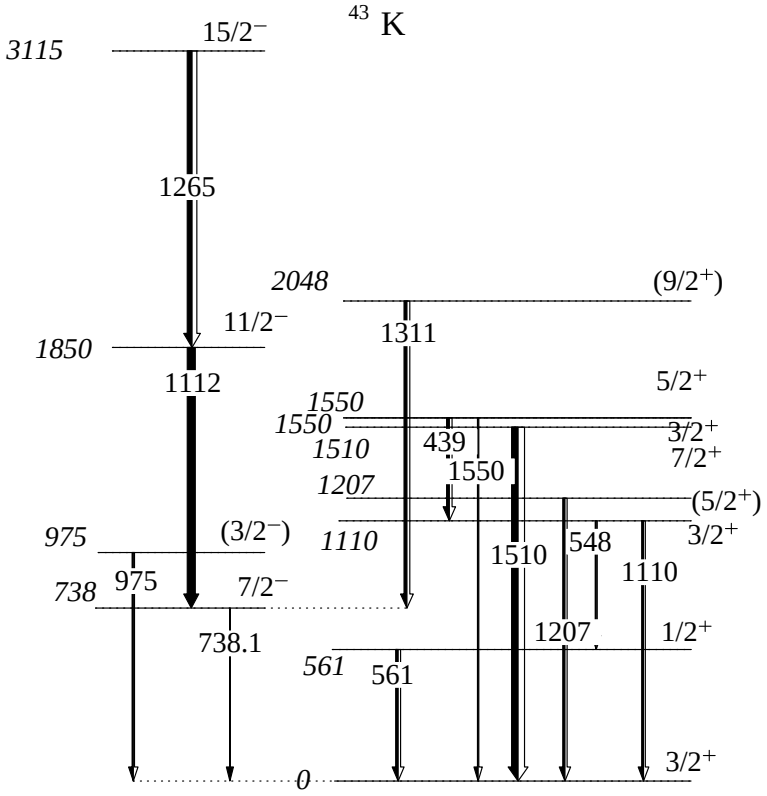

Figure 6.12: The experimental level scheme of ^{43}K, populated via $(+1p+2n)$ channel. Relative γ-ray intensities are indicated by the width of the arrows. Only γ transitions observed in our measurement are plotted. The energy, spin and parity of levels, their branching ratios and energy of transitions, if known, are as in Nuclear Data Sheets. The intensity of each transition was corrected for the efficiency of the γ-array.

populated negative parity state, $11/2^-$ with $\sim$50%, which is the strongest populated state in ^{41}K. Other higher-lying negative parity states, $15/2^-$ and $19/2^-$, are also observed with

significant strength. This is characteristic of heavy-ion induced transfer reactions where large angular momentum can be transferred. The transfer processes at energies near the barrier maximize transferred angular momentum to allow a good matching between orbital angular momenta of the involved states. This is reflected as a strong population of yrast states [1, 92].

It can be seen that many high-spin negative parity states are populated, about half of the total flux. These are non-natural parity states, and probably their configurations involve excitation of protons above $Z = 20$.

To conclude, in presented channels one observes a strong population of states with pronounced single-particle character. Both natural and non-natural parity states are populated. In addition, high spin states were also strongly populated which is one of the characteristics of heavy-ion induced transfer reactions since large angular momenta can be transferred. In particular, 7^+ state in ^{42}K is strongly populated, which was the strongest populated state in deuteron transfer reaction. It is interesting also to consider the position of such 7^+ states in other nuclei in the vicinity and we searched for the population of such states in other K isotopes. Unfortunately, the statistic in ^{40}K channel is to low for any conclusion about the population of the 7^+ state. Although ^{44}K channel has slightly larger statistic, it is relatively unknown nuclei. Very few levels are known and even less with attributed spin and parity, especially of high spin states. However, some new γ transitions are observed, but clear indication that one of these states belong to the 7^+ state has not been found.

6.2 Evaporation effect

In previous sections it was shown that beside direct transfer process, other mechanisms are present in defining the final distribution. In fact, secondary processes like evaporation can significantly modify the final yield. In the transfer process large amount of energy is exchanged between projectile and target, and part of this excitation energy is dissipated by evaporation, particularly the neutron evaporation. In this process a transfer product with primary mass A after evaporation feeds mass $A-x$, therefore the mass distribution of secondary products is affected mainly towards the lighter mass regions of a specific Z.

The ^{58}Ni+^{208}Pb multinucleon reaction was previously studied close to the Coulomb

barrier [31], and light and heavy fragments were identified in coincidence. For channels involving the stripping of few protons the isotopic distributions extend mainly along the neutron pick-up chain. As more protons are transferred the neutron flux tends to shift in the stripping direction. This trend was attributed, at least partly, to the effect of neutron evaporation from the primary fragments. Only after the effect of the evaporation was included in the calculations, the proton transfer channels were well reproduced. The same calculations were also performed for the heavy transfer products in order to obtain their survival probabilities against fission, which, averaged over neutron number, were from ∼100% for $(0p)$ to $(-2p)$ transfers, down to ∼50% for $(-6p)$ transfer. The inclusion of the evaporation mechanism in the calculations was also crucial in the description of the ^{40}Ca+^{208}Pb system that has similar mass and projectile-target asymmetry as our case.

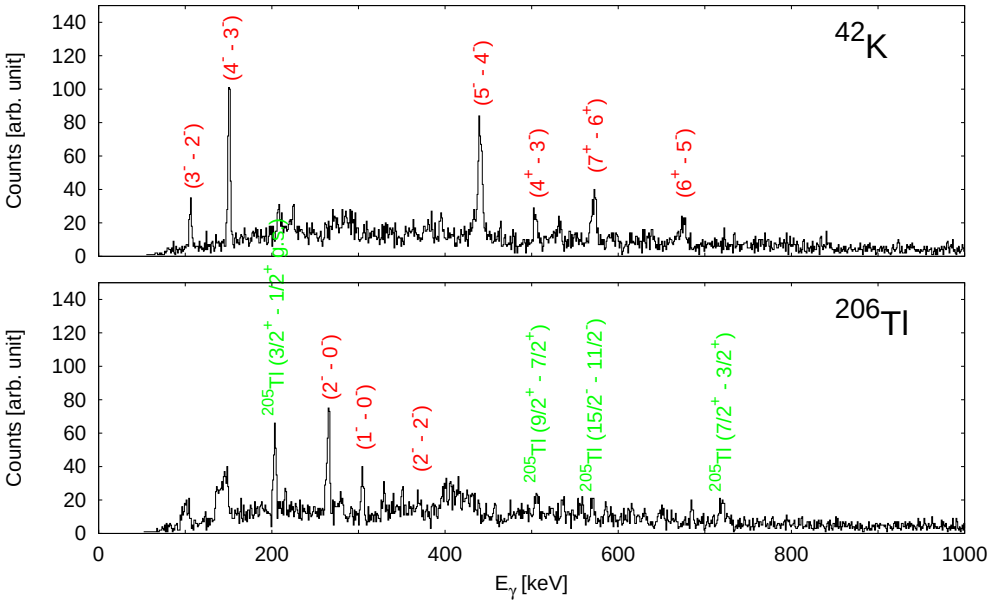

Figure 6.13: Doppler corrected γ spectrum of ^{42}K (top panel) and of heavy partner (bottom panel) where ^{206}Tl labels primary binary partner. γ rays belonging to nuclei after evaporation takes place are identified and labelled on the spectrum.

In the ^{40}Ar+^{208}Pb reaction we can directly observe these evaporation processes in the fragment-γ coincidence measurement. The method has been already used to evaluate the evaporation by looking at the γ-spectrum of the heavy partner [73]. The velocity vector of the undetected heavy partner can be evaluated and applied for the Doppler correction of its corresponding γ rays. Evaporation can be seen in the heavier partner since, after the light partner is selected, not only γ rays belonging to the primary binary partner are present, but also γ rays belonging to nuclei after evaporation takes place can be identified.

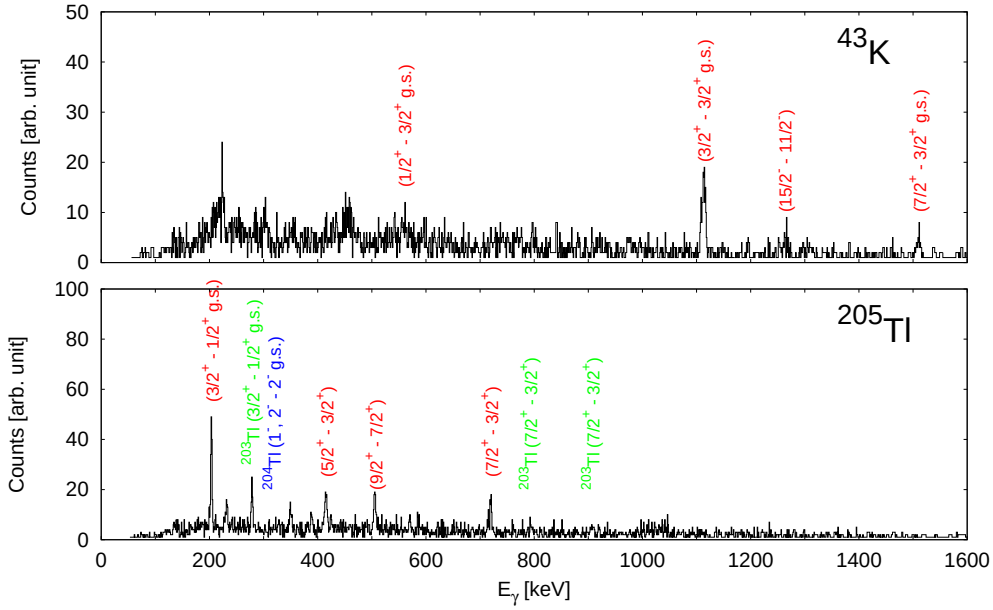

Figure 6.14: Doppler corrected γ spectrum of ^{43}K (top panel) and of heavy partner (bottom panel) where ^{205}Tl labels primary binary partner.

The effect is shown for the $(+1p+1n)$ and $(+1p+2n)$ channels in Figs. 6.13 and 6.14. The plot for $(+1p+1n)$ shows that strongest transitions, in fact, come from the primary heavy partner. However, a lot of transitions are coming also from ^{205}Tl, after the evaporation of one neutron takes place. This is even more pronounced in the case of $(+1p+2n)$ channel. Transitions belonging to ^{203}Tl, after the evaporation of two neutrons takes place, are very intense.

Figure 6.15 shows TKEL distribution of ^{42}K (top panel) and conditions that are put to construct γ-ray spectra in the bottom panels. Since neutron separation energy is $S_n = 7.5$ MeV, first gate is put at 8 MeV (gate A). γ rays after evaporation takes place are not visible in the corresponding γ spectrum. For higher energy gates γ rays from lighter Tl isotopes become stronger.

Evaporation is more relevant for nuclei far from the entrance channel, where it can significantly modify the final yield distribution. The TKEL spectra for neutron transfer channels show that major contribution is close to the ground-to-ground state Q-value. For proton transfer channels one observes higher TKEL values and one, thus, expects that the neutron evaporation has a stronger effect on the final mass distribution.

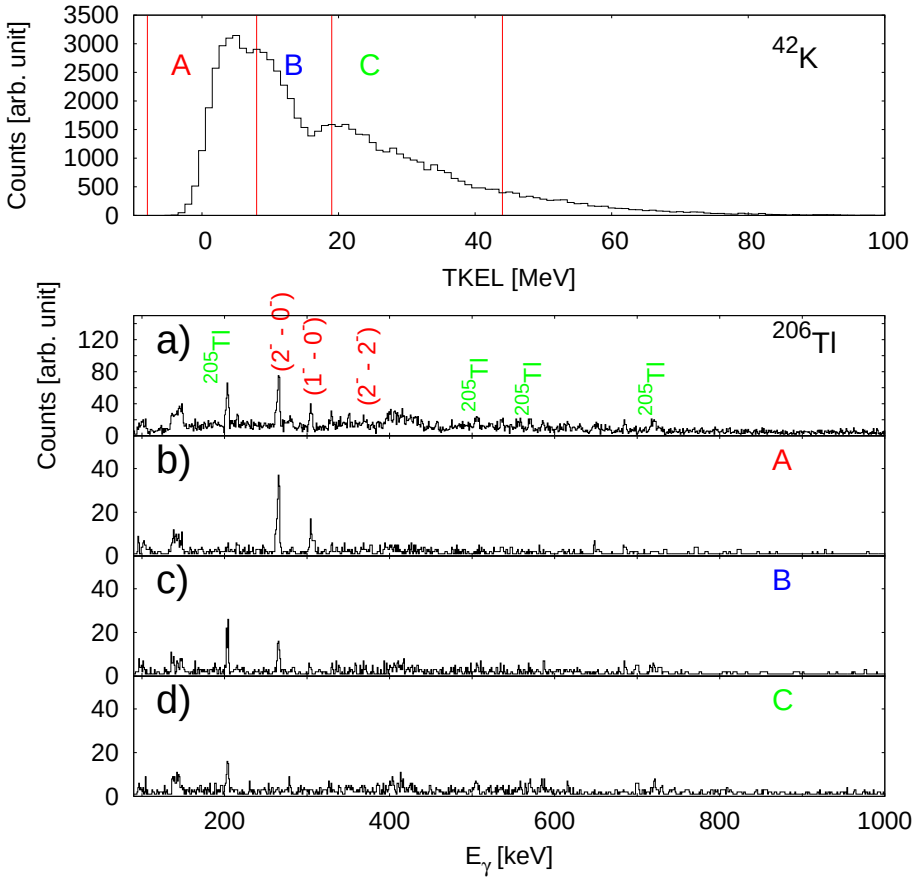

Figure 6.15: TKEL distribution for ^{42}K (top panel). Associated γ-ray spectra (bottom) for the heavy partner without conditions on TKEL (panel a) and conditioned (panels b, c and d) with different regions of TKEL distributions, marked as A, B and C in the TKEL spectrum (gates cover similar number of counts).

7 Discussion

7.1 Selected results of previous studies

When two-nucleon transfer takes place, the second nucleon follows the first one profiting from the nucleon-nucleon correlations. Due to weak binding, the correlation length of a pair is larger than nuclear dimension which allows the two members of a pair to move between target and projectile, essentially as a whole, also in the case of successive transfer. To study correlations in the nuclear medium, prediction of absolute cross sections, making use of nuclear structure spectroscopic factors informations, becomes necessary, since they are sole quantities which can be directly compared with experimental observables [25]. Experimental observables should be compared with calculations taking into account reaction dynamics and all important elementary degrees of freedom (single particles and phonons). In this way the effects of the additional degrees of freedom (as correlation) may be deduced.

The semi-classical models proved to properly reproduce a variety of experimental results with heavy ions. In the semi-classical approach the relative motion of the centre of mass of the two ions is treated classically. This is due to the fact that the wave length associated with the relative motion is much smaller than the interaction region (sum of the two nuclear radii) [1]. The transfer process is treated quantum mechanically.

Heavy-ion reactions are, in principle, an ideal tool for the study of the residual interaction in nuclei, in particular the components responsible for the couplings between the phonon degrees of freedom and those of the single particles (particle-vibration coupling), and via multinucleon transfer reactions the components responsible for particle correlations such as the pairing interaction [73]. Here we will briefly outline the main

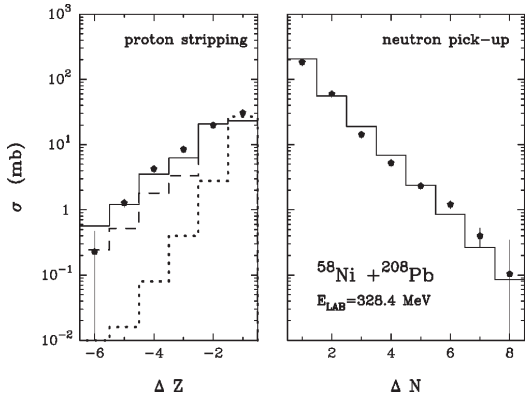

(A) The ^{58}Ni+^{208}Pb reaction. The dotted lines are the results of CWKB calculations using sequential transfer only, whereas the dashed lines also include pair-transfer modes. The solid line includes also the effect of evaporation [31].

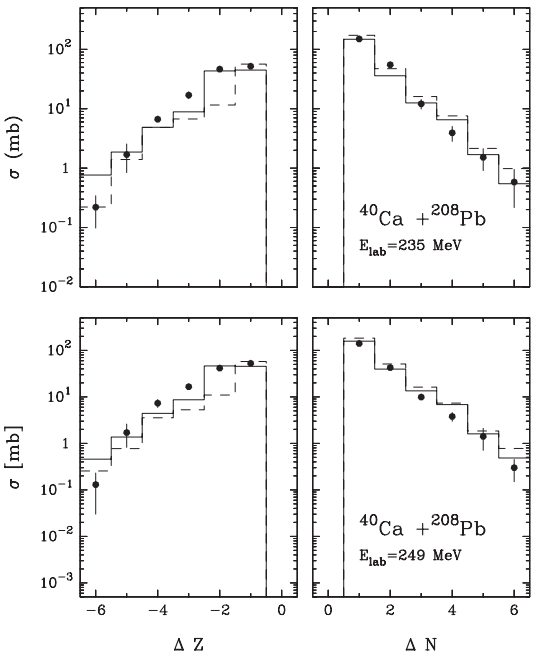

(B) The ^{40}Ca+^{208}Pb reaction. The dashed lines are the results of CWKB calculations using sequential transfer only, whereas the solid lines also include pair-transfer modes [30].

Figure 7.1: Experimental (points) and theoretical (lines) angle and Q-value integrated cross sections for pure proton stripping and pure neutron pick-up channels of the ^{58}Ni+^{208}Pb reaction measured at $E_{lab} = 328$ MeV and the ^{40}Ca+^{208}Pb reaction measured at $E_{lab} = 235$ and 249 MeV as a function of number of transferred nucleons.

findings from previous transfer reaction studies mainly illustrated through measurements performed at INFN - LNL, Italy [30, 31, 73, 93–95].

Two-nucleon transfer reactions have been investigated in order to obtain informations about correlated pair transfer. Because of the higher binding energy for protons and the associated steeper falloff of the wave functions at large distances, a larger overlap of the two interacting nuclei is required to exchange charged particles. Q-matching conditions and mostly negative ground-state Q-values favour proton stripping reactions. Proton pick-up reactions occur (with smaller yields) in systems involving neutron-rich projectiles [10]. In his review article [10], K.E. Rehm also noted that the ratio between the energy and angle integrated yields for one- and two-proton transfer reactions for a given ground state Q-value was only about 2, while it was 4-5 for the neutron transfer reactions.

In their review article [23], W. von Oertzen and A. Vitturi discuss transfer in terms of enhancement for pairs of both neutrons and protons in different systems (for instance

^{112}Sn+^{120}Sn, ^{86}Kr+^{54}Fe, ^{40,48}Ca+^{124}S). They discuss that the observed enhancement arises not only from the coherent successive transfer of two single nucleons, but also from the possible direct transfer of one spatially correlated pair. The interplay of these two processes is one of the key points in the understanding of pairing correlations in nuclei [23].

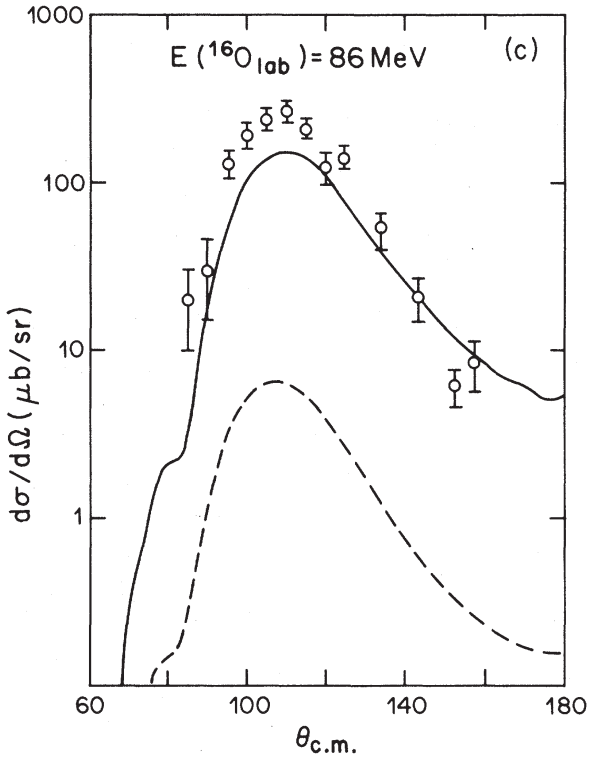

Figure 7.2: Comparison of calculated differential cross sections in a first-plus-second Born approximation and experimental data of ^{208}Pb(^{16}O,^{18}O)^{206}Pb ground state transition. The dashed lines give the result of the one-step calculation, and the solid lines the result of the one-step plus two-step calculation [96].

First full quantum mechanical calculation for one and two-neutron transfer performed by B.F. Bayman and J. Chen showed that the contribution of a process in which the two neutrons are transferred successively dominates over the simultaneous term, as illustrated in Fig. 7.2 for the two-neutron transfer reaction in the ^{16}O+^{208}Pb system measured near the Coulomb barrier. One-step plus two-step calculation gives a rather good representation of the absolute magnitude of the differential cross section over the entire measured angular range [96].

The second-order distorted wave Born approximation implementation of two-particle transfer direct reactions which includes simultaneous and successive transfer, properly corrected by non-orthogonality effects, was recently further improved and excellent agree-

ment with light-ion induced reactions and the mentioned ^{16}O+^{208}Pb reaction was obtained [25, 97–100].

Multinucleon transfer reactions ^{58}Ni+^{208}Pb [31] and ^{40}Ca+^{208}Pb [30] were studied at the time-of-flight spectrometer PISOLO at incident energies slightly above the Coulomb barrier. The total cross sections were obtained by integrating angular and Q-value distributions for each isotope and compared with semi-classical calculations (CWKB and GRAZING) (see Figs. 7.1A and 7.1B). The cross sections for neutron pick-up drop by almost a constant factor for each transferred nucleon, as an independent particle mechanism would suggest. A good agreement between data and theory is obtained for the pure neutron pick-up transfer and for channels involving the stripping of one proton. The pure proton stripping cross sections behave differently, and the population of the $(-2p)$ is almost as strong as the $(-1p)$ channel. This was explained by processes which involve the transfer of correlated protons in addition to the successive transfer of single protons.

These findings were fortified with calculations which explicitly included pair-transfer modes, both for proton stripping and neutron pick-up channels, with the same strength of macroscopic form factors. The treatment of the transfer degrees of freedom is based on the assumption that in a heavy-ion collision the exchange of a nucleon may proceed via many open channels that are all quite week, so that they may be treated as independent particles. The multinucleon transfer channels were estimated from the multi-step mechanism. The probability for the transfer of pair of nucleons is estimated by using the form factor for the transfer of two nucleons that is calculated from the macroscopic prescription [101]. The pair transfer couplings have following form:

$$f_P(r) \sim \beta_\lambda \frac{\partial U(r)}{\partial r} \tag{7.1}$$

where $U(r)$ is optical potential and the pair-deformation parameter β_λ gives the measure of the correlation strength. The full range of Q-value has been fulfilled by the inclusion of all transitions between the single-particle levels of projectile and target of a full shell below the Fermi surface and all single-particle levels above. Only one pair-transfer mode for $(-2p)$ and $(+2n)$ channels located at the optimum Q-value was used. The strength of these form factors was kept the same for protons and neutrons, and was fitted to the inclusive cross section of the $(-2p)$ channel.

The inclusion of the pair-transfer mode was essential for the description of the proton

channels, and didn't alter the good results for the neutron channels. Also, once the cross section of $(-2p)$ channel is reproduced, the predictions for the other charge transfer channels are much better, indicating the importance of the proton pair mode. Proton and neutron apparent asymmetry was present in all reactions studied so far. Nuclear structure calculations have shown that the pairing interaction has the same strength for both of them. Being the one-neutron transfer cross section almost one order of magnitude larger than the one-proton transfer, the contribution of a pair transfer mode is masked by the successive mechanism. The very short-range pairing interactions does not contribute directly to the transfer process but redistributes the strength around the pure particle-particle and hole-hole configurations of projectile and target. It is thus very difficult to deduce the effect of pairing correlations from inclusive cross sections only and separation of the individual states yields is very welcome.

The excitation functions, corroborated from the knowledge of the excitation spectra and the results of reaction and shell model calculations, provided valuable information in this respect for the ^{40}Ca+^{208}Pb system. By looking at the final population of the single-particle levels it was concluded that the maxima for the $(+2n)$ and $(+4n)$ channels are essentially due to two and four neutrons in the $p_{3/2}$ orbital. From the nuclear structure and reaction dynamics studies one expects that the $p_{3/2}$ orbital gives a much larger contribution to the two-nucleon transfer cross section than the $f_{7/2}$ orbital, which dominates the ground-state wave function. This fact, together with the known low-energy spectra of ^{42,44}Ca, suggest that these maxima correspond to the excited 0^+ states that were identified with the pair mode [102]. These experimental results (see Fig. 7.3) point to a selective feeding of 0^+ states dominated by a pair of neutrons in the $p_{3/2}$ orbital.

The ^{42}Ca was also populated in the ^{40}Ca+^{96}Zr reaction that was measured with PRISMA-CLARA set-up at energy 152 MeV, close to the Coulomb barrier. As in previous measurement, the TKEL spectra of ^{42}Ca shows that most of the cross section is concentrated in a pronounced peak at an energy that is compatible with the excitation of a group of 0^+ states at $\sim$6 MeV where a pairing-vibrational state should be located. The set-up allowed the observation of the decay pattern of the populated 0^+ state; and a γ transition at 4340 keV, which is consistent with a decay from a 0^+ level at 5.8 MeV to the 2_1^+ state, was observed.

Fully microscopic framework of the time-dependent Hartree-Fock (TDHF) theory have

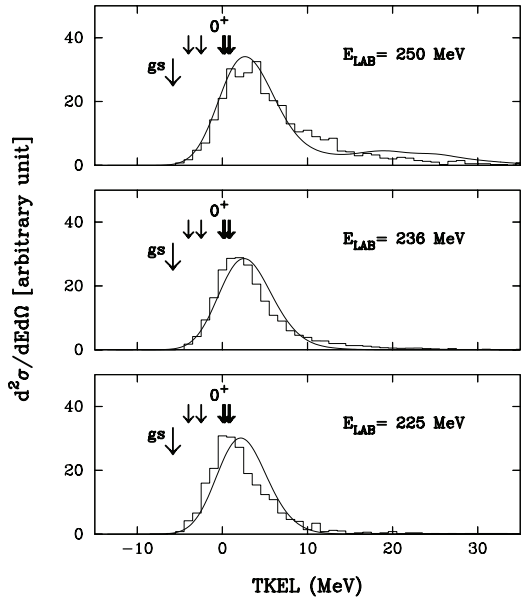

Figure 7.3: Experimental (histograms) and theoretical (curves) TKEL distributions of the $(+2n)$ channel in the ^{40}Ca+^{208}Pb reaction at the indicated energies. The arrows correspond to the energies of 0^+ states with an excitation energy lower than 7 MeV [30].

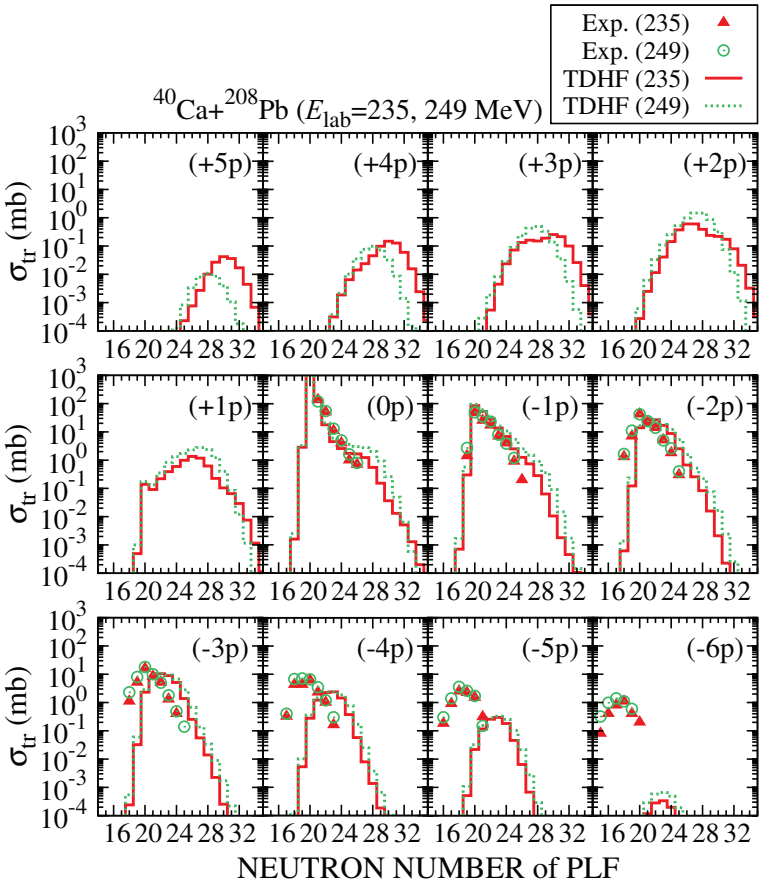

Figure 7.4: Transfer cross sections for the ^{40}Ca+^{208}Pb reactions at E_{lab}=235 and 249 MeV. Red filled triangles (green open circles) denote measured cross sections at E_{lab}= 235 (249) MeV. Red solid (green dotted) lines denote results of the TDHF calculations [21].

been recently applied for different systems [19–21, 103]. An example for the ^{40}Ca+^{208}Pb reaction at E_{lab}=235 and 249 MeV is shown in Fig. 7.4. Theory describes the transfer cross sections of a few nucleons reasonably and as the number of transferred nucleons increases, the agreement becomes less accurate. Results give qualitatively similar results to those of the semi-classical models [21]. In this comparison TDHF theory doesn't include correlations, but later it will be shown how they were incorporated in macroscopic approach.

An alternative way to probe correlations are measurements well below the Coulomb barrier. Theoretical interpretation of inclusive cross sections at and above Coulomb barrier is very complex due to the presence of many competing processes that depopulate channel of interest. At energies well below the Coulomb barrier, the interacting nuclei are at large distances so that they interact through the tail of their density distribution and are only slightly influenced by the nuclear potential [104]. When dealing with energies for which the colliding nuclei cannot overcome the Coulomb barrier, they are kept apart making negligible the formation of compound nuclei and ensuring that the transfer process is a direct one. Reaction products are excited in a restricted energy region (few MeV). Thus one needs to take into account few populated excited states which simplifies coupled channel calculations and quantitative information may be extracted on the nucleon-nucleon correlations. The main advantage, however, is that in the calculations of the transfer probabilities one needs only the overlap of the tails of the intrinsic wave functions that are involved in the transfer process, and these asymptotic behaviours are well known at least for single particle transfer [33]. The distortion of the Coulomb elastic waves by the nuclear attraction is very small and may easily be accounted for.

Measurements below the barrier are very complex and one encounters several problems. The transfer probability at large distances corresponds to forward angles where overwhelming yield of elastically scattered particles often prevents good identification of ions close to the projectile. Angular distributions are backward peaked reaching the maximum at $\theta_{cm} = 180°$. They are featureless with a behaviour that is independent on the transferred angular momentum l and grow monotonically. Also in direct kinematics projectile-like fragments have low kinetic energy. A complete identification of final reaction products in A, Z and Q-value thus becomes difficult. Cross sections are very small and this demands detectors with high efficiency.

Significant progress was made by using reactions in inverse kinematics to detect the lighter target-like outgoing recoils at forward angles. The ions are forward focused (high detection efficiency) and with high kinetic energy (for energy and therefore mass resolution). This method was first used to study the ^{124}Sn+^{58}Ni reaction with split-pole spectrometer [15, 16]. Due to low cross section, sub-barrier transfer reactions are difficult to measure and recently with the large solid angle and acceptance spectrometer PRISMA several systems were investigated with good ion identification also at very low bombarding energies [52].

In low energy collision the cross section for transfer products is proportional to the elastic one:

$$\frac{d\sigma}{d\Omega}_{tr} = P_{tr}\frac{d\sigma}{d\Omega}_{el+inel} \tag{7.2}$$

thus it is convenient to represent them in terms of the transfer probability. The transfer probability P_{tr}, defined for the measured angle as the ratio of the transfer cross section to the elastic cross section:

$$P_{tr} = \frac{d\sigma_{tr}}{d\sigma_{Ruth}} \tag{7.3}$$

is plotted as a function of the distance of closest approach (D) for a Coulomb trajectory. The distance of closest approach is related to the center-of-mass scattering angle θ_{cm} and the energy E_{cm}:

$$D = \frac{Z_a Z_A e^2}{2E_{cm}}\left(1+\frac{1}{sin(\theta_{cm}/2)}\right). \tag{7.4}$$

This is very attractive representation of the data since the angular distributions obtained at different bombarding energies will all be superimposed.

First the ^{96}Zr+^{40}Ca (closed shell nuclei) reaction has been measured in inverse kinematics where target recoils have been detected with PRISMA. Results of the measurement are presented in Fig. 7.5A, together with the semi-classical microscopic calculations for $(+1n)$ and $(+2n)$ neutron transfer channels that incorporated nucleon-nucleon correlations [33, 82, 106, 107]. The computed total transfer probability (full line) for $(+1n)$ channel was obtained by summing over all possible transitions that can be constructed from the single particle states in projectile and target. The set of single particle states covers a full shell below the Fermi level for the ^{96}Zr and a full shell above for the ^{40}Ca. One sees how calculations reproduce well the experimental slope as well as the absolute values of the transfer probabilities for the one neutron channel.

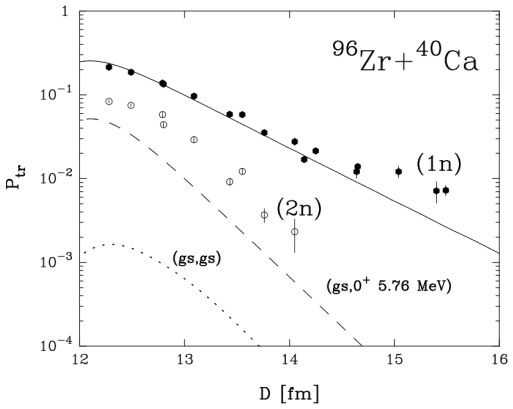

(A) The full line represents the inclusive transfer probability for $(+1n)$ transfer, the dotted line the ground-to-ground state transition for the $(+2n)$ transfer, and the dashed line the transition to the 0^+ excited state at 5.76 MeV in ^{42}Ca [33].

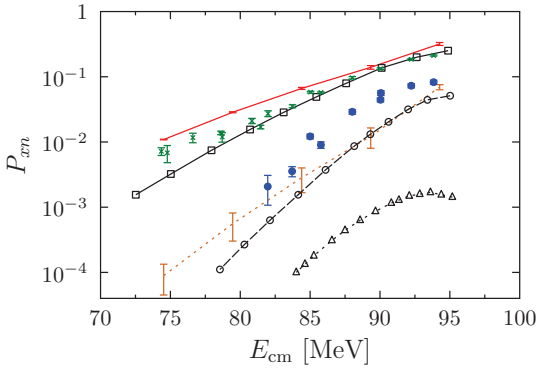

(B) The experimental data (same as in 7.5A) are represented by full circles for $(+2n)$ and crosses for $(+1n)$. The TDHF+BCS results are displayed by red solid line for the probability to transfer one neutron and by orange dashed line for the probability to transfer two neutrons. The results shown by squares and triangles are theoretical results shown in Fig. 7.5A. The open circles correspond to the $(+2n)$ transfer where also ground state to 0^+ excited state transfer is accounted for [105].

Figure 7.5: Transfer probability as a function of distance of closest approach for $(+1n)$ and $(+2n)$ in the ^{96}Zr+^{40}Ca reaction, measurement (points) is shown in comparison with the theoretical calculations (lines).

The ground state wave function for the ^{94}Zr was obtained from a BCS calculation by adopting a state independent pairing interaction, while for the description of ^{42}Ca the total Hamiltonian was diagonalized with a model space containing only two-particle configuration coupled to 0^+ (i.e. transfer of a $J = 0^+$ pair). The calculated probability for the ground-to-ground state transition is shown with a dotted line in Fig. 7.5A. The probability corresponding to the transition to the 0^+ state at 5.8 MeV in ^{42}Ca (dashed line) was much larger than the ground state one [33]. The role played by the single particle states $f_{7/2}$ and $p_{3/2}$ was already identified and discussed previously. The data are inclusive and the calculation includes only the transfer to 0^+ states, so a factor is still missing for the description of the total transfer cross section. The enhancement factor of $\sim$3 was ascribed to the fact that the two-nucleon transfer reaction does not populate only 0^+ states but it is much richer, and more complicated two-particle correlations have to be taken into account. The flattening of both probabilities at small internuclear distances, corresponding to large bombarding energies, is related to the increase of the absorption, and can be easily accounted for.

These transfer probabilities have been recently compared to the time-dependent Hartree-Fock + BCS (TDHF+BCS) theory where correlations are included in the approximative way via BCS (Fig. 7.5B) [20].

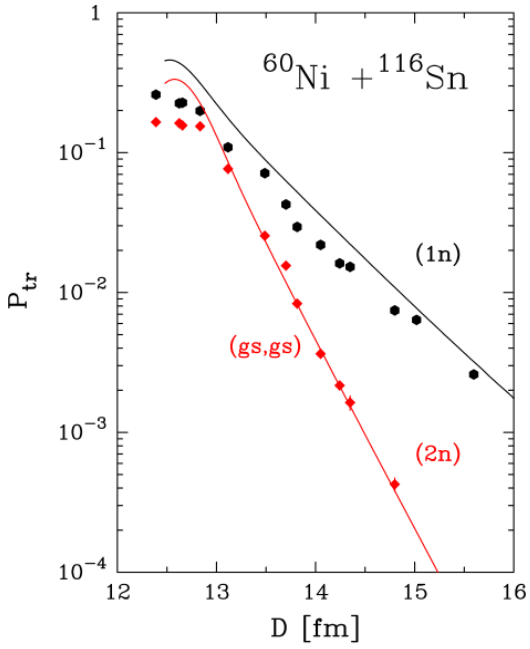

Figure 7.6: Transfer probability as a function of distance of closest approach, for $(+1n)$ and $(+2n)$ in ^{116}Sn+^{60}Ni reaction. Points represent the experimental values, solid lines are theoretical calculations [34].

The transfer probabilities for one- and two-neutron transfer channels in the ^{116}Sn+^{60}Ni system [34] were recently measured up to very large distances of closest approach. In this system the ground-to-ground state Q-values for neutron transfers are close to zero, matching the optimum Q-value (∼0 MeV). The same microscopic theory as for ^{96}Zr+^{40}Ca was applied and results are shown in Fig. 7.6. The result supports a mechanism in which a correlated pair is exchanged between the ground states of the interacting Sn and Ni nuclei. For the first time in a heavy-ion collision, a consistent description of one and two-neutron transfer reactions was obtained, both in shape and magnitude, by incorporating, in the reaction mechanism, all known structure information of entrance and exit channels nuclei. For the calculation of the two-neutron transfer channel, the formalism incorporates the contribution from both the simultaneous and successive terms. In particular, there is no need to introduce any enhancement factor for the description of two-neutron transfer, of course very important are the correlations induced by the pairing interaction. This achievement has been possible only because the chosen system is very

well Q-value matched so that the reaction is dominated by the ground-to-ground state transition.

7.2 Comparison with theoretical predictions for ^{40}Ar + ^{208}Pb

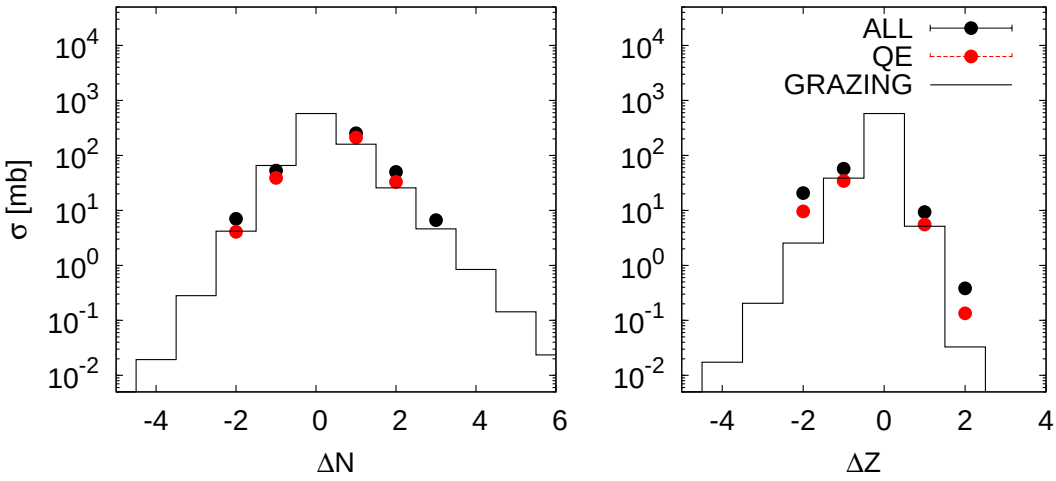

Figure 7.7: Total cross section (black symbols) and cross section of QE component (red symbols) for the pure proton and neutron transfer channels.

Now we will look how these findings apply to the ^{40}Ar+^{208}Pb system. Comparison of the total experimental cross sections for the pure neutron and proton transfer channels with the GRAZING calculations is shown in Fig. 7.7. Angle and TKEL integrated total cross sections are shown with black points, while the cross sections integrated over low TKEL part (QE component) are shown with red points (as explained in Section 5.3).

The behaviour of the neutron pick-up side indicates that neutrons are transferred independently and for each transfer step the cross section drops by a factor ∼6. Theory well reproduces the data, especially the QE cross section. In particular, the $(\pm 1n)$ and $(\pm 1p)$ channels are well reproduced by the GRAZING calculations. However, the pure proton stripping cross sections behave differently from neutron ones, since the population of the $(-2p)$ channel is only 2 times lower than the $(-1p)$ channel. The GRAZING calculations clearly underestimate the corresponding cross sections for $(-2p)$ channel, suggesting that processes involving the transfer of correlated proton pairs in addition to the successive transfer of independent protons may contribute, which is consistent with

previous results. The fact that pure proton stripping and neutron pick-up are well Q-value matched can be seen in figure, since they are stronger than the pure proton pick-up and neutron stripping channels. The $(-2n)$ and $(+2p)$ channels, in comparison with the calculations, behave similarly as $(+2n)$ and $(-2p)$ channels. The trend of both, the total and QE cross sections, is similar, being the QE cross section in better agreement with the GRAZING calculations.

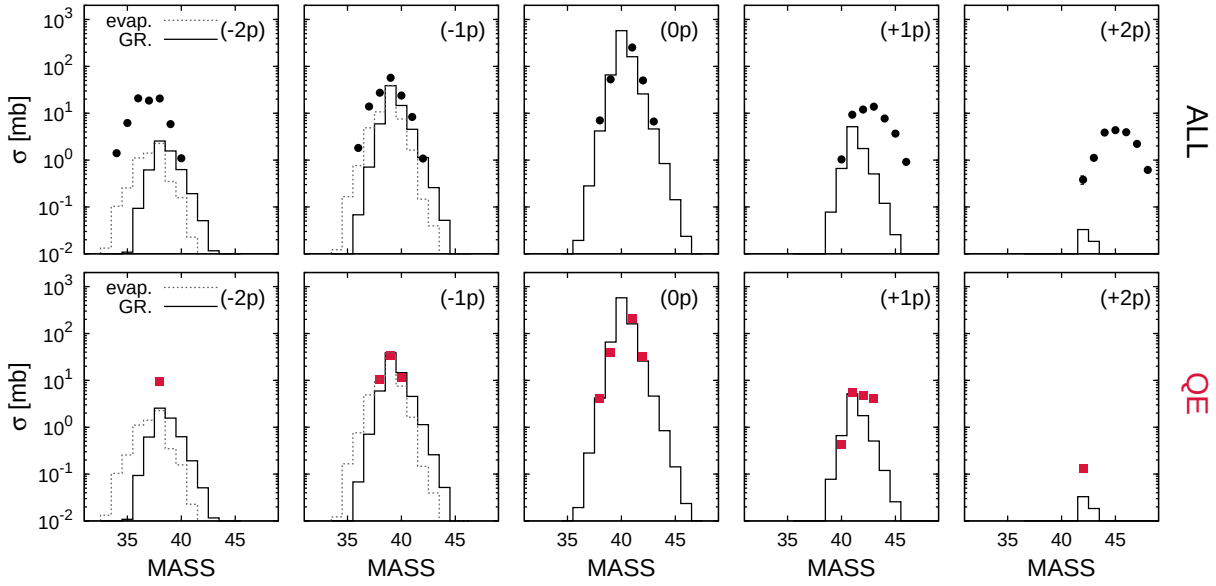

Figure 7.8: Inclusive total cross section (top) and QE cross section (bottom panel). Points are experimental values, the black histograms are GRAZING calculations and the grey dotted histograms are the GRAZING calculations with included evaporation (see Table 5.3).

We will look the (np) channels in more details. The total cross sections, experimental and calculated, for all representative channels are shown in Fig. 7.8. The $(+1p+1n)$ transfer channel leading to ^{42}K is under-predicted by GRAZING calculations (bottom panel) by a factor 2.7. The $(-1p-1n)$ channel is also under-predicted by calculations (top panel). On the other hand, this channel is difficult to interpret because one expects stronger contribution of the neutron evaporation mechanism. In fact, it can be seen from Fig. 7.8 that this channel, especially in the bottom panel, is better reproduced after evaporation was included in GRAZING calculations (dashed lines). Effect of neutron evaporation from the primary fragments affects more more massive transfer channels where one observes a larger drift of the data towards the neutron stripping side. The pure proton stripping channels become less favoured as more protons are transferred, with the centroids of the mass distributions shifting to lower values.

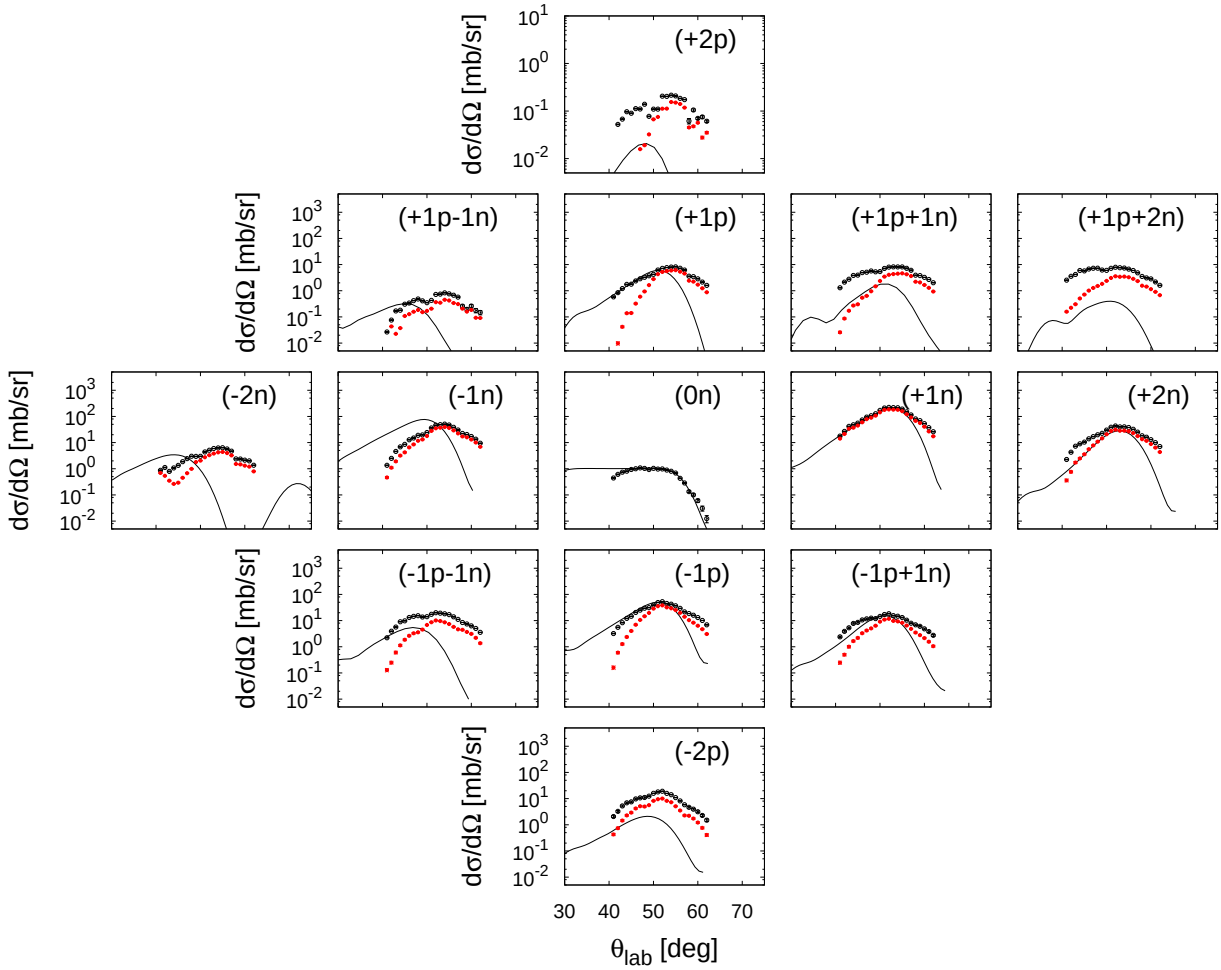

Figure 7.9: Differential cross sections for representative channels. Black points are angular distributions integrated over all TKEL, while red points correspond to integration of the low TKEL part. Black lines are the GRAZING calculations. The elastic cross section is given as ratio to Rutherford cross section.

Differential cross sections provide valuable informations and are shown in Fig. 7.9 for several selected channels. Black points are differential cross sections integrated over entire TKEL range, while red points are integrated over low TKEL part (QE component). Black curves are GRAZING calculations. Single particle transfers are dominated by QE component and corresponding angular distributions are very similar to the ones integrated over entire TKEL range (black symbols). As more nucleons are transferred the difference between the total and QE angular distributions is more apparent, particularly at forward angles. It can be noticed that GRAZING describes all single-particle transfers well, especially when considering only QE component and neutron transfer channels. The $(+2n)$ channel is also very well described both in shape and magnitude. Neutron striping transfer channels are well described in magnitude, however they are shifted in angle with

respect to GRAZING calculations, especially when more neutrons are transferred, which may be attributed to Q-value mismatch for these channels, at variance with the matching for neutron pick-up ones. The experimental selection of a weaker $(-2n)$ channel was difficult, and clear separation of charge states from the strong elastic channel was probably the source of forward angle rising. As expected, and in agreement with previous findings, the GRAZING calculations under-predict the $(\pm 2p)$ channels. In our case, the $(+2p)$ channel is rather weak and strongly influenced by DIC, thus it is difficult to draw a clear conclusion.

Again proton and neutron asymmetric behaviour can be due to the fact that the one-neutron transfer cross section is almost one order of magnitude larger than the one-proton transfer. Thus, the contribution of a pair-transfer mode in the neutron sector may be masked by the successive mechanism.

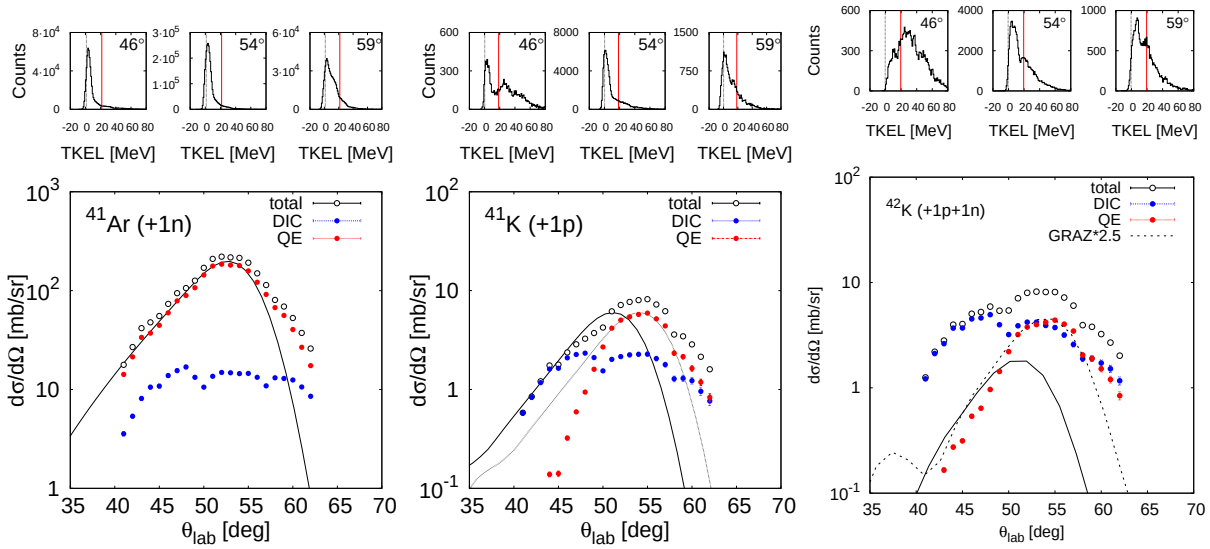

(A) $(+1n)$ channel. (B) $(+1p)$ channel. (C) $(+1p+1n)$ channel.

Figure 7.10: Angular distributions integrated over total energy losses (empty points), integrated over small energy losses (red points) and over large energy losses (blue points). Black lines are GRAZING calculation. Total kinetic energy loss distributions for all three PRISMA angular settings are represented in top panels where red line indicated a TKEL cut used to separate QE and DIC component.

The angular distribution integrated over entire TKEL range of $(+1p+1n)$ is under-predicted (factor $\sim$5) by the GRAZING calculations, which indicates that some additional degrees of freedom have to be considered for that channel. Thus, we displayed in Fig. 7.10 in top panels the integrating regions (red line) in total kinetic energy loss distributions for $(+1n)$, $(+1p)$ and $(+1p+1n)$ for all three PRISMA angular settings used to separate QE

component. Bottom panel displays integrated differential cross sections that have been extracted by integrating the full TKEL range (black points) and by integrating only the low part of the TKEL, corresponding to QE component (red) and DIC component (blue). Black curves are GRAZING calculations.

As mentioned, one particle transfers, both $(+1n)$ and $(+1p)$, are very well reproduced by GRAZING calculation both in shape and magnitude. The better Q-value matched channel $(+1n)$ is better reproduced, while $(+1p)$ channel is reasonably well reproduced in shape, and very well in magnitude.

The angular distribution of the $(+1p+1n)$ channel is broader than the calculated one, especially at forward angles, which indicates a possible influence of deep inelastic scattering in this channel which is why the TKEL distributions were studied in more details. As already concluded, the differential cross section of QE processes has bell shaped angular distribution typical for these processes with maximum around grazing angle. In addition, in this QE case the matching of three different PRISMA settings is much better. These QE angular distributions are shown in Fig. 7.11. It is clear that the QE angular distribution for $(+1p+1n)$ channel is still under-predicted (factor $\sim$2.5) by the GRAZING calculations, even when only QE contribution is considered.

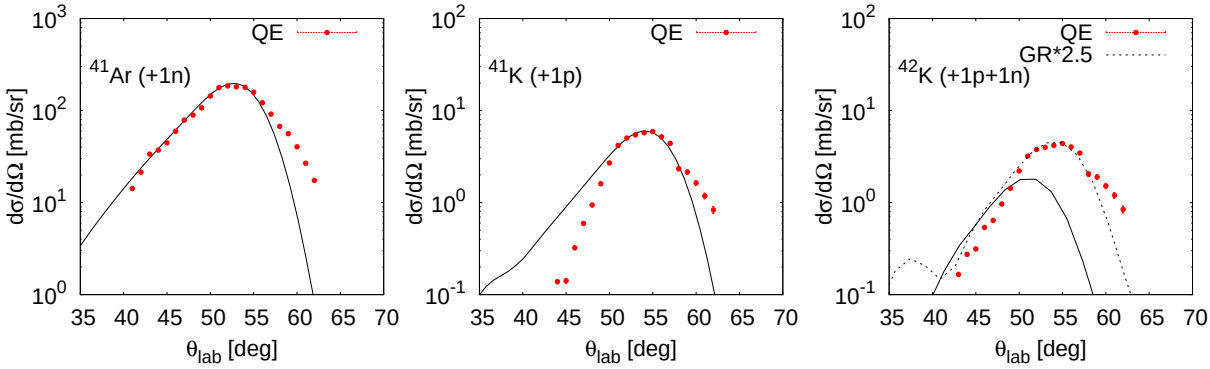

(A) $(+1n)$ channel. (B) $(+1p)$ channel. (C) $(+1p+1n)$ channel.

Figure 7.11: Experimental QE angular distributions (points) and the GRAZING calculated ones (lines). For $(+1p)$ and $(+1p+1n)$ channel the GRAZING calculated angular distribution was shifted by $+3°$.

With the ability to measure individual transitions, one may get a deeper insight into correlations and by looking at the population of individual states and their dominant underlying structure a step further can be made. It is known that the very short-range pairing interaction redistributes the strength around the pure particle-particle and hole-hole configurations, thus the yield distribution over the individual states provides important

complementary informations [84].

Looking at the population of the final states in ^{42}K it was demonstrated in Chapter 6 that beside the population of the low-lying negative parity states, a strong excitation of the 7^+ state has been observed. From an analysis of the strength distribution, the population of this state turns out to account for ∼16% of the total yield. The dominant structure of the low-lying negative parity state can be viewed as a multiplet arising from the coupling of the unpaired proton in the $d_{3/2}$ and the unpaired neutron in the $f_{7/2}$ orbital. Such low-lying states of natural parity are usually strongly excited in the transfer reactions.

On the other hand, a structure of the 7^+ state involves the promotion of a proton to the pf shell. It can be viewed in the simple picture as the coupling of the $f_{7/2}$ neutron to the $f_{7/2}$ proton in the stretched configuration. The Bansal-French-Zamick weak-coupling model supports this simple picture. It is very interesting that this state was by far the strongest populated state in the (very selective) deuteron transfer ^{4}He+^{40}Ar reaction [91].

The comparison of the strength distributions of the populated states in ^{42}K observed in the ^{40}Ca+^{96}Zr and in the ^{40}Ar+^{208}Pb reactions, reveals that in the case of the ^{40}Ca+^{96}Zr reaction, where ^{42}K was reached via stripping of one proton and pick-up of three neutrons, no selective population of specific states was observed. In fact, a similar strength of all populated states was observed.

It is clear that two-nucleon transfer plays a special role in the study of pairing in nuclei, and they can be viewed as the specific probe of nuclear pairing correlations. It is still an open question whether pair correlations can be probed in heavy-ion collisions. The search for their signatures has been attempted via the measurement of two-particle transfer channels. In the first step, the actual cross section is compared to the predictions of models using uncorrelated states. The obtained enhancement factor, in principle, provides a direct measurement of the correlation of the populated states. In our case the measured cross section of the $(+1p+1n)$ channel is enhanced in comparison with the prediction of the GRAZING calculation.

By using heavy-ion reactions, unfortunately one has to deal with the reaction mechanism complicated by the interplay between nuclear and Coulomb trajectories. This is why we studied very carefully the behaviour of the TKEL, and the excited state population. The measured absolute differential cross section of the relevant channels (see Fig. 7.11)

is the main observable which relates experiment and theory. In fact, the strength and presence of the correlation will emerge from a direct comparison of the measured and the microscopically calculated cross sections, where all essential ingredients for accurate description of the nuclear structure and dynamics are employed.

It is important to pursue further studies with different nuclear structure. These studies will be of particular relevance in the near future due to the advent of radioactive beams where these problematics are of top priority to understand some of the basic properties of very weakly bound nuclei. In this context, and especially considering the transfer reactions, it is extremely important to extend the microscopic formalism in such a way to calculate the transfer of pairs with large angular momentum.

7.3 Outlook: the ^{92}Mo+^{54}Fe reaction

In order to study into more detail the (np) correlations, a measurement of the excitation function from above to deep below the Coulomb barrier has been performed. The "proton-rich" ^{92}Mo+^{54}Fe system was studied by exploiting the large acceptance of the PRISMA spectrometer. In order to detect Fe-like target recoils, PRISMA was positioned at $\theta_{lab} = 20°$, corresponding to $\theta_{cm} = 140°$. Proton transfer channels are in general more difficult to obtained far below the barrier since they drop off more rapidly than neutron channels, thus so far experimental data were rare.

Analysis of PRISMA data was already presented in Chapter 3 and will not be repeated here, only main result will be presented. The preliminary results of transfer probability P_{tr} plotted as a function of the distance of closest approach D are presented in Fig. 7.12. Transfer probability represented in this way exhibits exponentiation fall. This is proportional to the square root of binding energy E_B of the transferred particle:

$$\frac{d\sigma}{d\Omega} \sim e^{-2\sqrt{-2\mu_N E_B}D} \tag{7.5}$$

where μ_N is reduced mass of transferred particle. Within a simple phenomenological interpretation of the data, a fit of the transfer probability for the $(+1n)$ and $(+1p)$ channel can be made. If one neutron and one proton are transferred independently (black and blue lines in Fig. 7.12 are fits), the $(+1p+1n)$ channel should have a transfer probability equal to $P_{1n} * P_{1p}$ (dotted line in Fig. 7.12). The enhancement with respect to sequential,

independent transfer is observed (see red and dotted grey lines) which indicates some additional degrees of freedom and possible transfer of a neutron-proton correlated pair. In addition, the slope of expected $P_{1n} * P_{1p}$ transfer differs strongly in comparison with the measured one. These results are still preliminary and more careful analysis is needed, as well as the comparison with theoretical calculations.

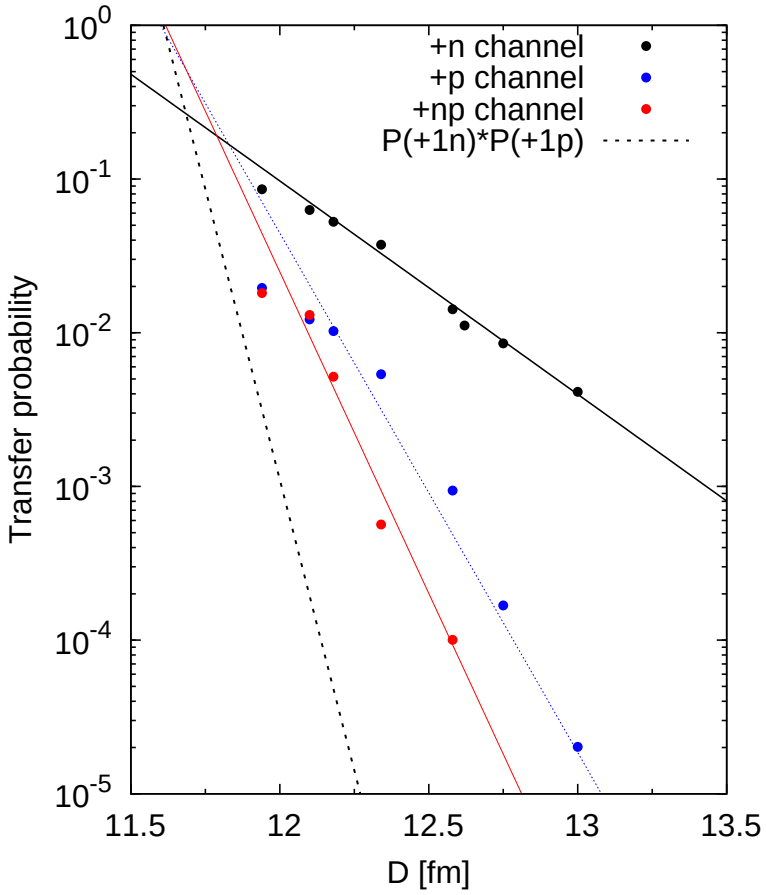

Figure 7.12: Preliminary results of transfer probability as a function of distance of closest approach, for $(+1n)$, $(+1p)$ and $(+1p+1n)$ channels in the ^{92}Mo+^{54}Fe reaction (points). Black, blue and red lines are fits, while the grey dotted line corresponds to probability for sequential transfer $P_{1n} * P_{1p}$.

Conclusion

The ^{40}Ar+^{208}Pb multinucleon transfer reaction was measured near the Coulomb barrier with the large solid angle magnetic spectrometer PRISMA coupled to the CLARA HPGe array. The measurement was performed on three different spectrometer's angular settings covering more than 20°, which allowed to extract total cross section for different reactions channels. Analysis was performed for each of the (A, Z) channels separately. Careful evaluation of the response function of the spectrometer allowed to match different angular distributions for the first time and to obtain absolute cross sections for the transfer channels. The analysis of the elastic scattering enabled the extraction of the absolute normalization values of the data. With the coupling of the two detectors it has been possible to perform coincidences between the ions detected with the magnetic spectrometer and their associated gamma rays, measured with the CLARA array. This thesis provides a complete study of the many channels open in the multinucleon transfer reaction and focuses on the investigation of the reaction properties, in terms of differential and total cross sections and total kinetic energy loss distributions.

The transfer of several nucleons gives the possibility to study the relative role of single nucleon and pair transfer modes. Through the simultaneous study of the absolute cross sections for all channels populated via transfer of nucleon pairs $(\pm nn)$, $(\pm pp)$ and $(\pm np)$, and their comparison with the theoretical predictions that include only the transfer of independent particles, we tried to explore the contribution of nucleon-nucleon correlation. We also explored the contribution of the deep inelastic component to the reaction cross section, which was possible thanks to the very wide energy acceptance of the PRISMA spectrometer.

The employed semi-classical theory, at the basis of the GRAZING model, well reproduces the data, especially the quasi-elastic cross sections, for the $(\pm xn)$ and $(\pm 1p)$ transfer channels. The behaviour of neutron transfer channels suggests that neutrons are

transferred independently. The pure proton stripping channels behave differently. The yield of the $(-2p)$ channel is only two times smaller than that of the $(-1p)$ one and it is clearly underestimated by the calculations. It is important to notice that when only the quasi-elastic part of the cross section was considered, the $(\pm 2p)$ channels were still under-predicted by GRAZING calculations. The same holds for the $(+1p+1n)$ channel. The comparison with the GRAZING model can be taken as a first step in the theoretical interpretation. The fact that one-particle transfer channels, both for neutrons and protons, are well reproduced indicates the correct treatment of the dynamical and structural properties in the model.

In comparison with the same semi-classical model, where correlations are not incorporated, the cross section of $(+1p+1n)$ channel turns out to be enhanced. This result was corroborated with the population strength of the excited states for the same channel, extracted via γ-particle coincidences. In this way important complementary information could be obtained, since it is known that the very short-range pairing interaction redistributes the transfer strength over different final states. We observed, besides the expected population of the low-lying states, a strong excitation of the 7^+ state, emerging from the coupling of a neutron and a proton in the $f_{7/2}$ orbital. The same state was by far the strongest populated state also in the deuteron transfer reaction in the ^{4}He+^{40}Ar system.

It is clear that two-nucleon transfer plays a special role in the study of pairing in nuclei, and they can be viewed as a specific probe of nuclear pairing correlations. The presented findings have to be complemented with other measurements, one of which is the study of the behaviour of transfer channels below the Coulomb barrier, where the excitation energies of the final reaction products are expected to be much smaller. Our findings, the presence of the enhancement in the $(+1p+1n)$ channel in comparison with the model where correlations are not incorporated, and the main strength observed in a state where the proton and neutron of the same orbital are coupled in the stretched configuration, need to be compared with a microscopic theory, where all essential ingredients for accurate description of the nuclear structure and dynamics are employed. It would be important to extend the microscopic formalism in such a way to calculate the transfer of pairs with large angular momentum. This kind of studies are of particular relevance for future studies with radioactive beams, where correlations are expected to be significantly modified.

A Calibration of PRISMA detectors

A.1 MCP position calibration

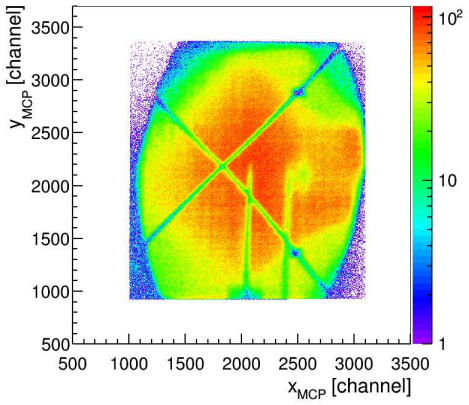

(A) Data in coincidence with the MWPPAC.

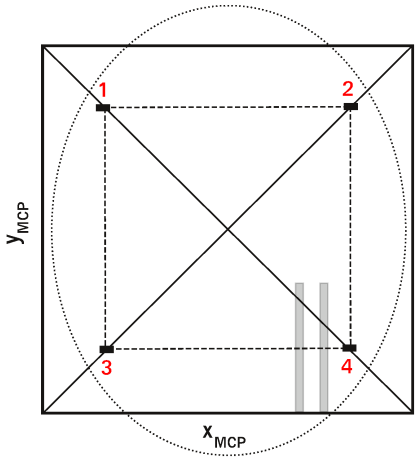

(B) Scheme of the mask used for the calibration of the MCP detector. The centre of the cross and the reference points on its branches have to be placed in the coordinates given in Table A.1.

Figure A.1: x_{MCP} and y_{MCP} entrance positions.

The cross visible in the Fig. A.1A is the projection of a mask placed about 1 cm downstream of the Carbon foil and it is used for calibration of x_{MCP} and y_{MCP} positions. The metallic cross stops the ions and creates a clear shadow when the coincidence with the focal plane is required, while it's faded when there is no coincidence. This mask, shown in Fig. A.1B, has four arms intersecting in a point which is almost coincident with the center of the MCP, namely the point where the central trajectory of PRISMA crosses the Carbon foil. Two lines that are visible on the right side of the MPC matrix are shadows of nails that were put inside the quadrupole. When the mask is mounted

Table A.1: Coordinates in channels of the four reference points used to calibrate the MCP detector.

Point	x_{MCP} [channel]	y_{MCP} [channel]
center	1000	1000
1	570	1530
2	1430	1530
3	1430	470
4	570	470

it is usually rotated 2-3°. This has to be corrected during the analysis and the MCP matrix is rotated until these two lines are again vertical. The position is then calibrated, since distance of four reference points that are visible on the cross arms is fixed at 4 cm from the centre. Table A.1 shows correspondence between pairs of coordinates in units of channels with respect to a known reference system. For a proper calibration the MCP has to be mirrored with respect to the vertical axis and the shadows of the nails will be on the left side of the MCP matrix. Calibration is done with the polynomial function of first degree that is calculated in order to fit all reference points [67, 72].

The elliptic shape of the MCP matrix can be understood considering the geometry of PRISMA: since the detecting surface of the MCP is placed between the target and the quadrupole entrance, the fraction of the reaction products emitted at the target's position, that the spectrometer transmits toward the focal plane, is approximately a cone crossing the MCP and entering the quadrupole. The ellipse raises from the intersection between this cone and the detecting surface of the MCP [67].

A.2 MWPPAC position calibration

Polygonal gate can be put on the matrix *right+left* vs. *cathode*, shown in Fig. A.2A, to select only "good" events and decrease background signals.

For each section position information is obtained from the difference between signals from the left and right side of the delay lines:

$$x_{PPAC} = right - left. \tag{A.1}$$

Since position on the focal plane is obtained with delay line method it may happen that

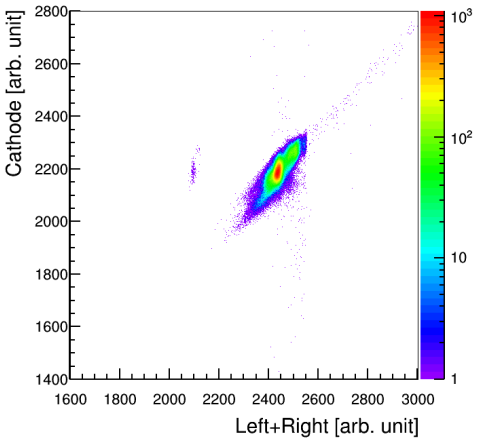

(A) Plot of the *left+right* (x axis) vs. *cathode* (y axis) signals that is used to suppress the background.

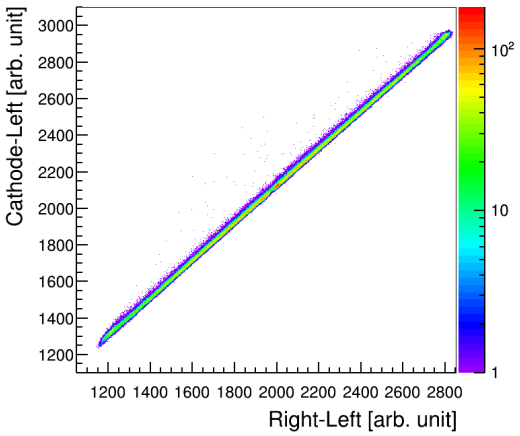

(B) Plot used for correction of incomplete events.

Figure A.2: Plots used to obtained MWPPAC position information.

a signal is detected on one side, while the signal on the opposite side is missing. In order not to loose these events and to recover statistics, they can be reconstructed by using the cathode signal. In this case cathode is substituting the signal that is missing. For example if *right* is missing, expression A.1 becomes $x_{PPAC} = left - cathode$. The procedure requires a calibration between the coordinates x_{PPAC} and cathode signal in order to get the right reconstruction of the position for the incomplete events. Figure A.2B is used to find the slope and the offset of the lines in the histogram describing the relation between x_{PPAC} and $x_{PPAC} = left - cathode$ in case of missing *right* signal. The three signals can be then combined to determine x_{PPAC}. Position on the focal plane, x_{PPAC}, is then calibrated to millimetres.

A.3 TOF calibration and alignment

TOF is measured between MWPPAC cathode signals and entrance detector time signal that is suitably delayed. Figure A.3A shows horizontal position on the focal plane x_{PPAC} versus TOF where ten sections of MWPPAC are visible. First step is to calibrate TOF signals in nanoseconds and for this one applies off-line calibration coefficients. Calibrated spectrum is shown in Fig. A.3B clearly showing different TOF offsets in different sections. All ten sections then have to be aligned with respect to each other.

The crucial step is to define absolute (global) offset. As a first step this can be adjusted

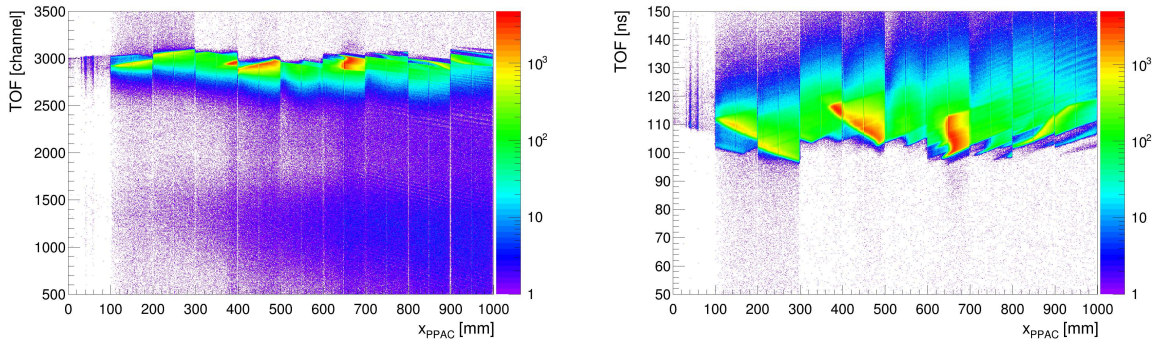

(A) TOF not calibrated and not aligned. (B) TOF calibrated but not aligned.

Figure A.3: Non aligned x_{PPAC} - TOF spectra.

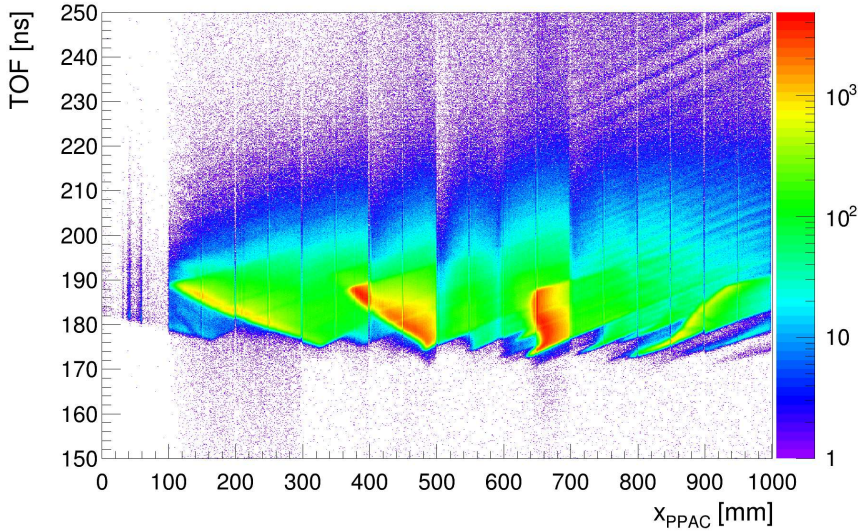

Figure A.4: Position on the focal plane versus calibrated and aligned TOF.

on the basis of TOF estimates. Length of the trajectory of ^{40}Ar is equal to distance between MCP and MWPPAC which is roughly 6 m. Considering the loss of energy in the target, one can estimate the velocity of ^{40}Ar from the beam energy. Velocity can be further checked with the energy of electromagnetic transitions measured with CLARA, which are very sensitive to the Doppler correction. By applying Doppler correction to the γ spectra one can check whether main lines have correct energy and width. This is an iterative procedure that ends when the proper offset of the TOF is found, i.e. when the main peaks have both the correct position in energy and width as small as possible. The structures that are visible on Fig. A.4 are related to different A/q ratios that are reaching the focal plane.

B CLARA configuration table

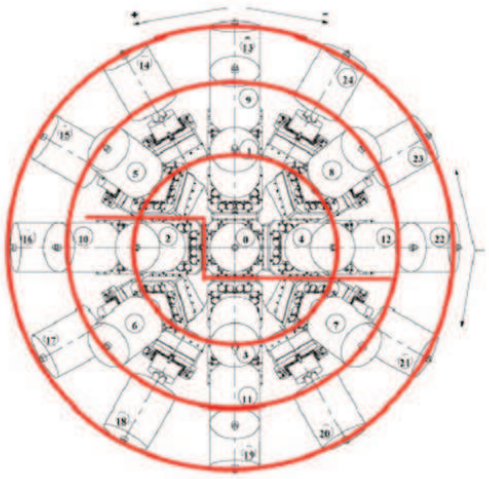

Figure B.1: Schematic view of the three rings of CLARA (red circles), correspondent to three different angular positions (with respect to the θ coordinate) [72].

Table B.1: CLARA detectors angular positions. $\#D$ is clover and $\#c$ Ge crystal number. θ and ϕ are angles of the crystals measured in the PRISMA frame of reference.

$\#D$	$\#c$	θ	ϕ	$\#D$	$\#c$	θ	ϕ	$\#D$	$\#c$	θ	ϕ
00	002	171.1	225.0	09	038	131.4	355.8	18	074	103.8	146.9
	003	171.1	315.0		039	124.5	356.2		075	97.8	146.9
	000	171.1	45.0		036	124.5	4.8		072	97.8	154.1
	001	171.1	135.0		037	131.4	5.2		073	103.8	154.1
01	006	157.9	351.4	10	042	131.4	85.8	19	078	103.8	176.9
	007	150.5	353.3		043	124.5	86.2		079	97.8	176.9
	004	150.5	7.7		040	124.5	94.8		076	97.8	184.1
	005	157.9	9.6		041	131.4	95.2		077	103.8	184.1
02	010	157.9	81.4	11	046	131.4	175.8	20	082	103.8	206.9
	011	150.5	83.3		047	124.5	176.2		083	97.8	206.9
	008	150.5	97.7		044	124.5	184.8		080	97.8	214.1
	009	157.9	99.6		045	131.4	185.2		081	103.8	214.1
03	014	157.9	171.4	12	050	131.4	265.8	21	086	103.8	236.9
	015	150.5	173.3		051	124.5	266.2		087	97.8	236.9
	012	150.5	187.7		048	124.5	274.8		084	97.8	244.1
	013	157.9	189.6		049	131.4	275.2		085	103.8	244.1
04	018	157.9	261.4	13	054	103.8	356.9	22	090	103.8	266.9
	019	150.5	263.3		055	97.8	356.9		091	97.8	266.9
	016	150.5	277.7		052	97.8	4.1		088	97.8	274.1
	017	157.9	279.8		053	103.8	4.1		089	103.8	274.1
05	021	135.1	45.4	14	058	103.8	26.9	23	094	103.8	296.9
	022	137.5	36.7		059	97.8	26.9		095	97.8	296.9
	023	132.7	32.0		056	97.8	34.1		092	97.8	304.1
	020	129.3	40.1		057	103.8	34.1		093	103.8	304.1
06	026	129.3	140.9	15	062	103.8	56.9	24	098	103.8	329.9
	027	132.7	149.1		063	97.8	56.9		099	97.8	329.9
	024	137.5	144.4		060	97.8	64.1		096	97.8	334.1
	025	135.1	135.7		061	103.8	64.1		097	103.8	334.1
07	028	135.1	225.5	16	066	103.8	86.9				
	029	137.5	216.7		067	97.8	86.9				
	030	132.7	212.1		064	97.8	94.1				
	031	129.3	220.2		065	103.8	94.1				
08	034	129.3	321.0	17	070	103.8	116.9				
	035	132.7	329.2		071	97.8	116.9				
	032	137.5	324.4		068	97.8	124.1				
	033	135.1	315.7		069	103.8	124.1				

C Error induced by the response function

Error induced by the response function can be estimated if one builds, for each of the studied channels, several response functions. This can be done by calculating the average value of nearby cells with different smoothing procedures, thus obtaining different response functions starting from the original one. Their comparison is then used to estimate the error.

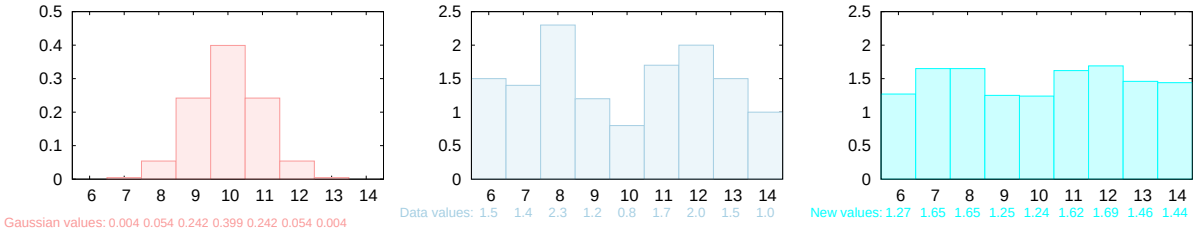

(A) Standard discrete Gaussian.

(B) Set of data made out of random numbers.

(C) The smoothed version of the original data.

Figure C.1: Example of Gaussian smoothing on one dimensional random values. The "kernel" for smoothing defines the shape of the function that is used to take the average of the neighbouring points. In Gaussian smoothing we use a kernel with the shape of a Gaussian (normal distribution) curve. Here on panel (A) is a standard discrete Gaussian, with a mean of 10 and a sigma of 1. Set of data made out of random numbers is shown on panel (B). If we start from point 10, we first multiply the Gaussian values by the values of the data, and sum the results to get the new smoothed value for point 10. Thus, the new value for point 10 is $...+0.054\times2.3+0.242\times1.2+0.399\times0.8+0.242\times1.7+0.054\times2.0+...=1.266$. This new smoothed value is stored for future use, and we move on, to the next point, and repeat the process, with the Gaussian kernel now centred over 11. This process is done for each point, starting from the beginning, to eventually obtain the smoothed version of the original data shown on panel (C).

The average value depends on the technique and the size of the average bin. Two techniques are used:

1. **Gaussian smoothing**, which is a smoothing procedure that is using a Gaussian function to calculate the average value of the neighbouring cells in the matrix. In

two-dimensional case it is simply the product of two Gaussian distributions, one in each dimension, and smoothing can be performed in two directions separately [108]. The procedure goes through the matrix point by point. For each point a new value that is a Gaussian function of the original value at that point and the surrounding data points is generated. In practice, the procedure starts by moving Gaussian shape with some standard deviation to the center of the first point (cell). In order not to do an overall scaling of the values after the smoothing, the values in the Gaussian curve are divided by the total area under the curve, so that the values add to 1. Finally a discrete Gaussian is obtained. Then the Gaussian values are multiplied by the values of the data. The results are summed to get the new smoothed value for that point. The new value is stored and procedure continues on the next point. Each cell's new value is set to a weighted average of that cell's neighbourhood, with the average weighted more towards the value of the central cell (having the highest Gaussian value).

2. **Moving average**, is a calculation to analyse data points by creating a series of averages of the value itself and the neighbouring points. When calculating successive values, a new value comes into the sum and an old value drops out, so a central moving average is computed. Data equally spaced on either side of the value are used, which requires using an odd number of points in the sample window [109].

Bibliography

[1] L. Corradi, G. Pollarolo, and S. Szilner. Multinucleon transfer processes in heavy-ion reactions. *Journal of Physics G: Nuclear and Particle Physics*, 36(11):113101, 2009.

[2] S. Szilner et al. Interplay between single-particle and collective excitations in argon isotopes populated by transfer reactions. *Physical Review C*, 84:014325, July 2011.

[3] S. Szilner et al. Structure of chlorine isotopes populated by heavy ion transfer reactions. *Physical Review C*, 87:054322, May 2013.

[4] A. Winther. Grazing reactions in collisions between heavy nuclei. *Nuclear Physics A*, 572:191–235, May 1994.

[5] A. Winther. Dissipation, polarization and fluctuation in grazing heavy-ion collisions and the boundary to the chaotic regime. *Nuclear Physics A*, 594:203–245, November 1995.

[6] URL `http://personalpages.to.infn.it/~nanni/grazing/`.

[7] G. R. Satchler. *Introduction to nuclear reactions.* Oxford University Press, New York, USA, 1990.

[8] R. A. Broglia. *Heavy ion reactions.* Westview Press, USA, 2004.

[9] R. Bass. *Nuclear reactions with heavy ions.* Springer-Verlag, Berlin, Heidelberg, Germany, 1980.

[10] K. E. Rehm. Quasi-elastic heavy-ion collisions. *Annual Review of Nuclear and Particle Science*, 41:429–468, December 1991.

[11] P. R. John et al. Shape evolution in the neutron-rich osmium isotopes: Prompt γ-ray spectroscopy of ^{196}Os. *Physical Review C*, 90:021301, August 2014.

[12] C. H. Dasso, G. Pollarolo, and A. Winther. Systematics of isotope production with radioactive beams. *Physical Review Letters*, 73:1907, October 1994.

[13] S. Szilner et al. Neutron-rich heavy nuclei explored via multinucleon transfers. *Letter of Intent for the SPES radioactive ion beam project at the Legnaro National Laboratories*, 2014.

[14] P.J.A. Buttle and L.J.B. Goldfarb. Neutron transfer in heavy ion reactions. *Nuclear Physics A*, 78:409, July 1966.

[15] C. L. Jiang et al. Multineutron transfer in ^{58}Ni+^{124}Sn collisions at sub-barrier energies. *Physical Review C*, 57:2393, May 1998.

[16] H. Esbensen, C. L. Jiang, and K. E. Rehm. Coupled-channels analysis of ^{58}Ni+^{124}Sn reactions. *Physical Review C*, 57:2401, May 1998.

[17] V.I. Zagrebaev, A.V. Karpov, and W. Greiner. Synthesis of superheavy nuclei: Obstacles and opportunities. *EPJ Web of Conferences*, 86:00066, Janury 2015.

[18] V. I. Zagrebaev and W. Greiner. Production of new heavy isotopes in low-energy multinucleon transfer reactions. *Physical Review Letters*, 101:122701, September 2008.

[19] C. Simenel. Particle transfer reactions with the time-dependent Hartree-Fock theory using a particle number projection technique. *Physical Review Letters*, 105:192701, November 2010.

[20] G. Scamps and D. Lacroix. Effect of pairing on one- and two-nucleon transfer below the Coulomb barrier: A time-dependent microscopic description. *Physical Review C*, 87:014605, January 2013.

[21] K. Sekizawa and K. Yabana. Time-dependent Hartree-Fock calculations for multinucleon transfer processes in ^{40,48}Ca+^{124}Sn, ^{40}Ca+^{208}Pb, and ^{58}Ni+^{208}Pb reactions. *Physical Review C*, 88:014614, July 2013.

[22] A. Bohr, B. R. Mottelson, and D. Pines. Possible analogy between the excitation spectra of nuclei and those of the superconducting metallic state. *Physical Review*, 110:936, May 1958.

[23] W. von Oertzen and A. Vitturi. Pairing correlations of nucleons and multi-nucleon transfer between heavy nuclei. *Reports on Progress in Physics*, 64:1247, September 2001.

[24] D.M. Brink and R.A. Broglia. *Nuclear Superfluidity: Pairing in Finite Systems*. Cambridge University Press, UK, 2005.

[25] G. Potel, A. Idini, F. Barranco, E. Vigezzi, and R. A. Broglia. Cooper pair transfer in nuclei. *Reports on Progress in Physics*, 76:106301, October 2013.

[26] M. Igarashi, K. Kubo, and K. Yagi. Two-nucleon transfer reaction mechanisms. *Physics Reports*, 199:1–72, January 1991.

[27] J. B. Ball, R. L. Auble, and P. G. Roos. Study of the zirconium isotopes with the (p,t) reaction. *Physical Review C*, 4:196, July 1971.

[28] W. Mayer et al. Strong population of excited 0^+ states in even Zr isotopes observed with the (^{14}C, ^{16}O) reaction. *Physical Review C*, 26:500, August 1982.

[29] C. Wu, W. von Oertzen, D. Cline, and M.W. Guidry. Pairing correlations and two-nucleon transfer between heavy nuclei. *Annual Review of Nuclear and Particle Science*, 40:285–326, December 1990.

[30] S. Szilner et al. Multinucleon transfer processes in ^{40}Ca+^{208}Pb. *Physical Review C*, 71:044610, April 2005.

[31] L. Corradi et al. Light and heavy transfer products in ^{58}Ni+^{208}Pb at the Coulomb barrier. *Physical Review C*, 66:024606, August 2002.

[32] L. Corradi et al. Multi-neutron transfer in ^{62}Ni+^{206}Pb: A search for neutron pair transfer modes. *Physical Review C*, 63:021601(R), January 2001.

[33] L. Corradi et al. Single and pair neutron transfers at sub-barrier energies. *Physical Review C*, 84:034603, September 2011.

[34] D. Montanari et al. Neutron pair transfer in ^{60}Ni+^{116}Sn far below the Coulomb barrier. *Physical Review Letters*, 113:052501, July 2014.

[35] P. Fröbrich. Enhancement of deuteron transfer reactions by neutron-proton pairing correlations. *Physical Letters B*, 37:338–340, December 1971.

[36] *The Scientific Objectives of the SPIRAL 2 Project*. GANIL, France, 2006.

[37] A. O. Macchiavelli et al. Is there *np* pairing in N=Z nuclei? *Physical Review C*, 61: 041303(R), March 2000.

[38] B. Cederwall et al. Evidence for a spin-aligned neutron–proton paired phase from the level structure of ^{92}Pd. *Nature*, 469:68–71, January 2011.

[39] E.C. Simpson and J.A. Tostevin. Two-nucleon correlation effects in knockout reactions from ^{12}C. *Physical Review C*, 83:014605, January 2011.

[40] A. M. Stefanini et al. Fusion of ^{48}Ca + ^{90,96}Zr above and below the Coulomb barrier. *Physical Review C*, 73:034606, March 2006.

[41] A. M. Stefanini et al. Sub-barrier fusion of ^{40}Ca + ^{94}Zr: Interplay of phonon and transfer couplings. *Physical Review C*, 76:014610, July 2007.

[42] G. Montagnoli et al. Effects of transfer channels on near- and sub-barrier fusion of ^{32}S + ^{48}Ca. *Physical Review C*, 87:014611, January 2013.

[43] A. M. Stefanini et al. Fusion of ^{40}Ca + ^{96}Zr revisited: Transfer couplings and hindrance far below the barrier. *Physical Letters B*, 728:639, January 2014.

[44] C. L. Jiang et al. Fusion hindrance for a positive Q-value system ^{24}Mg + ^{30}Si. *Physical Review Letters*, 113:022701, July 2014.

[45] A. M. Stefanini et al. The heavy-ion magnetic spectrometer PRISMA. *Nuclear Physics A*, 701:217–221, April 2002.

[46] A. Gadea et al. Coupling a CLOVER detector array with the PRISMA magnetic spectrometer. *The European Physical Journal A*, 20:193–197, March 2004.

[47] A. Gadea et al. Conceptual design and infrastructure for the installation of the first AGATA sub-array at LNL. *Nuclear Instruments and Methods in Physics Research A*, 654:88–96, October 2011.

[48] F. Recchia et al. Spectroscopy of odd-mass cobalt isotopes toward the $N = 40$ subshell closure and shell-model description of spherical and deformed states. *Physical Review C*, 85:064305, June 2012.

[49] S. Lunardi et al. Spectroscopy of neutron-rich Fe isotopes populated in the ^{64}Ni+^{238}U reaction. *Physical Review C*, 76:034303, September 2007.

[50] N. Marginean et al. Shape transitions far from stability: The nucleus ^{58}Cr. *Physical Letters B*, 633:696, February 2006.

[51] C. Louchart et al. Collective nature of low-lying excitations in ^{70,72,74}Zn from lifetime measurements using the AGATA spectrometer demonstrator. *Physical Review C*, 87:054302, May 2013.

[52] L. Corradi et al. Multinucleon transfer reactions: Present status and perspectives. *Nuclear Instruments and Methods in Physics Research Section B*, 317:743–751, December 2013.

[53] C.A. Ur. Perspectives for the gamma-ray spectroscopy at LNL: the GALILEO project. *Journal of Physics: Conference Series*, 366:012044, 2012.

[54] D. Montanari et al. Probing the nature of particle–core couplings in ^{49}Ca with gamma spectroscopy and heavy-ion transfer reactions. *Physical Letters B*, 697: 288–293, March 2011.

[55] D. Montanari et al. Gamma spectroscopy of calcium nuclei around doubly magic ^{48}Ca using heavy-ion transfer reactions. *Physical Review C*, 85:044301, April 2012.

[56] J. J. Valiente Dobon et al. Lifetime measurements of the neutron-rich N=30 isotones ^{50}Ca and ^{51}Sc: Orbital dependence of effective charges in the fp shell. *Physical Review Letters*, 102:242502, June 2009.

[57] C. Michelagnoli et al. Lifetime measurement of the 6.79 MeV state in ^{15}O with the AGATA demonstrator. *AIP Conf. Proc.*, 1484:281, 2012.

[58] D. Mengoni et al. Lifetime measurements of excited states in neutron-rich ^{44,46}Ar populated via a multinucleon transfer reaction. *Physical Review C*, 82:024308, August 2010.

[59] V. Modamio et al. Lifetime measurements in neutron-rich ^{63,65}Co isotopes using the AGATA demonstrator. *Physical Review C*, 88:044326, October 2013.

[60] L. Corradi et al. Studies of pair transfer processes with the SPES beams. *Letter of Intent for SPES - LNL*, 2014.

[61] Mark Huyse. *The Euroschool Lectures on Physics with Exotic Beams, Vol. I.* Springer Berlin Heidelberg, 2004.

[62] V. I. Zagrebaev, B. Fornal, S. Leoni, and W. Greiner. Formation of light exotic nuclei in low-energy multinucleon transfer reactions. *Physical Review C*, 89:054608, May 2014.

[63] Y. Blumenfeld, T. Nilsson, and P. Van Duppen. Facilities and methods for radioactive ion beam production. *Physica Scripta*, 2013:014023, January 2013.

[64] F. W. Aston. A positive ray spectrograph. *Philosophical Magazine*, 38:707–714, 1919.

[65] H. Savajols et al. VAMOS: a VAriable MOde high acceptance spectrometer. *Nuclear Physics A*, 654:1027c–1032c, July 1999.

[66] A. Cunsolo et al. Technique for 1st order design of a large-acceptance magnetic spectrometer. *Nuclear Instruments and Methods in Physics Research Section A*, 481:48–56, April 2002.

[67] Andrea Latina. *Study of Heavy-Ion Reactions with the Magnetic Spectrometer PRISMA: On-line and Off-line Data Analysis.* PhD thesis, University of Turin, 2004.

[68] Sugathan Pullanhiotan. *Characterization of a large acceptance spectrometer and its application to spectroscopy of exotic nuclei.* PhD thesis, Inter University Accelerator Centre (IUAC), New Delhi and Andhra University, Visakhapatnam, 2008.

[69] G. Montagnoli et al. The large-area micro-channel plate entrance detector of the heavy-ion magnetic spectrometer PRISMA. *Nuclear Instruments and Methods in Physics Research A*, 547:455–463, August 2005.

[70] S. Beghini et al. The focal plane detector of the magnetic spectrometer PRISMA. *Nuclear Instruments and Methods in Physics Research A*, 551:364–374, October 2005.

[71] URL `http://clara.lnl.infn.it/`.

[72] Daniele Montanari. *Reaction dynamics of neutron rich nuclei in Ca isotopes with heavy ions and gamma spectroscopy*. PhD thesis, University of Milan, 2011.

[73] S. Szilner et al. Multinucleon transfer reactions in closed-shell nuclei. *Physical Review C*, 76:024604, August 2007.

[74] G. Duchêne et al. The Clover: a new generation of composite Ge detectors. *Nuclear Instruments and Methods in Physics Research Section A*, 432:90–110, August 1999.

[75] K. Shima et al. Empirical formula for the average equilibrium charge-state of heavy ions behind various foils. *Nuclear Instruments and Methods in Physics Research*, 200:605–608, September 1982.

[76] G. F. Knoll. *Radiation Detection and Measurement*. John Wiley and Sons Inc., New York, USA, 2000.

[77] G. Cowan. *Statistical Data Analysis*. Clarendon Press, Oxford, 1998.

[78] D. Montanari et al. Response function of the magnetic spectrometer PRISMA. *The European Physical Journal A*, 47:4, January 2011.

[79] K.E. Rehm et al. Transition from quasi-elastic to deep-inelastic reactions in the ^{48}Ti+^{208}Pb system. *Physical Review C*, 37:2629, June 1988.

[80] K.E. Rehm et al. Systematic behavior of one- and two-nucleon transfer reactions induced by medium-weight projectiles. *Physical Review C*, 42:2497, December 1990.

[81] L. Corradi. *Electrostatic Accelerators, Fundamentals and Applications, Part III, Nuclear Reactions*. Springer Berlin Heidelberg, Germany, 2005.

[82] R.A. Broglia, G. Pollarolo, and A. Winther. On the absorptive potential in heavy ion scattering. *Nuclear Physics A*, 361:307–325, May 1981.

[83] D. Montanari et al. Elastic, inelastic, and one-nucleon transfer processes in ^{48}Ca+^{64}Ni. *Physical Review C*, 84:054613, November 2011.

[84] S. Szilner. Probing nucleon-nucleon correlations via heavy ion transfer reactions. *EPJ Web of Conferences*, 86:00059, January 2015.

[85] F. Nowacki and A. Poves. New effective interaction for $0\hbar\omega$ shell-model calculations in the $sd-pf$ valence space. *Physical Review C*, 79:014310, January 2009.

[86] E. Caurier, G. Martínez-Pinedo, F. Nowacki, A. Poves, and A. P. Zuker. The shell model as a unified view of nuclear structure. *Reviews of Modern Physics*, 77:427, June 2005.

[87] R.R. Whitehead. *Theory and Applications of Moment Methods in Many-Fermion Systems*. Plenum, New York, USA.

[88] *National Nuclear Data Center, Brookehaven National Laboratory and Nuclear Data Sheets therein*. URL `http://www.nndc.bnl.gov`.

[89] L. P. Ekstrom, H. H. Eggenhuisen, G. A. P. Engelbertink, J. A. J. Hermans, and H. J. M. Aarts. Spin-parity assignments to yrast states of ^{42}K. *Nuclear Physics A*, 283:157–175, June 1977.

[90] H.H. Eggenhuisen, L.P. Ekström, G.A.P. Engelbertink, J. Mondria, M.A. Van Driel, and J.A.J. Hermans. Recoil-distance lifetime measurements of low-lying states of ^{21}Ne, ^{24}Na, ^{25}Mg and ^{42}K with the B+^{16}O and ^{26}Mg+^{18}O reactions. *Nuclear Physics A*, 246:231–245, April 1975.

[91] R. M. Del Vecchio, R. T. Kouzes, and R. Sherr. Experimental study of $(f^2_{7/2})7^+$ states in s-d shell nuclei. *Nuclear Physics A*, 265:220–252, March 1976.

[92] Maja Varga Pajtler. *Nucleon transfer reactions in the ^{90}Zr+^{208}Pb system*. PhD thesis, University of Zagreb, 2014.

[93] L. Corradi et al. Multinucleon transfer reactions in ^{40}Ca + ^{124}Sn. *Physical Review C*, 54:201, July 1996.

[94] L. Corradi et al. Evidence of complex degrees of freedom in multinucleon transfer reactions of ^{48}Ca + ^{124}Sn. *Physical Review C*, 56:938, August 1997.

[95] L. Corradi et al. Multinucleon transfer processes in ^{64}Ni + ^{238}U. *Physical Review C*, 59:261, January 1999.

[96] B. F. Bayman and J. Chen. One-step and two-step contributions to two-nucleon transfer reactions. *Physical Review C*, 26:1509, October 1982.

[97] G. Potel, A. Idini, F. Barranco, E. Vigezzi, and R. A. Broglia. Nuclear field theory predictions for ^{11}Li and ^{12}Be: Shedding light on the origin of pairing in nuclei. *Physics of Atomic Nuclei*, 77:941–968, August 2014.

[98] G. Potel, A. Idini, F. Barranco, E. Vigezzi, and R. A. Broglia. Quantitative study of coherent pairing modes with two-neutron transfer: Sn isotopes. *Physical Review C*, 87:054321, May 2013.

[99] G. Potel, F. Barranco, F. Marini, A. Idini, E. Vigezzi, and R. A. Broglia. Calculation of the transition from pairing vibrational to pairing rotational regimes between magic nuclei ^{100}Sn and ^{132}Sn via two-nucleon transfer reactions. *Physical Review Letters*, 107:092501, August 2011.

[100] G. Potel, F. Barranco, E. Vigezzi, and R. A. Broglia. Evidence for phonon mediated pairing interaction in the halo of the nucleus ^{11}Li. *Physical Review Letters*, 105: 172502, October 2010.

[101] C.H. Dasso and G. Pollarolo. Macroscopic formfactors for pair transfer in heavy ion reactions. *Physical Lettters B*, 155:223, May 1985.

[102] S. Szilner et al. Search for pairing-vibration states of even Ca isotopes in ^{40}Ca+^{208}Pb transfer reactions. *The European Physical Journal A*, 21:87–91, July 2004.

[103] M. Evers et al. Cluster transfer in the reaction ^{16}O+^{208}Pb at energies well below the fusion barrier: A possible doorway to energy dissipation. *Physical Review C*, 84:054614, November 2011.

[104] D. Montanari et al. Heavy-ion transfer reactions studied at large internuclear distances with the PRISMA magnetic spectrometer. *Journal of Physics: Conference Series*, 420:012161, 2013.

[105] G. Scamps and D. Lacroix. Effect of pairing on transfer and fusion reactions. *EPJ Web of Conferences*, 86:00042, January 2015.

[106] G. Pollarolo, R.A. Broglia, and A. Winther. Calculation of the imaginary part of the heavy ion potential. *Nuclear Physics A*, 406:369, March 1983.

[107] J. H. Sorensen and A. Winther. Energy dependence of two-particle transfer in heavy-ion collisions. *Nuclear Physics A*, 550:306, May 1992.

[108] URL `http://en.wikipedia.org/wiki/Gaussian_blur`.

[109] URL `http://en.wikipedia.org/wiki/Moving_average`.

List of Figures

List of Tables

Biography

Tea Mijatović was born in 1983, in Požega, Croatia, where she attended the elementary and secondary school. She graduated in Physics in 2009 at the Faculty of Science, University of Zagreb, Croatia with thesis: "Use of multiple scatterings and reactions in nuclear spectroscopy", under supervision of prof. Matko Milin. In 2010 Tea joined fellowship program for young researchers at Laboratori Nazionali di Legnaro on the study of the use of scintillator detectors as ancillary detectors for the PRISMA spectrometer. Since 2010 she is employed as an assistant at Ruđer Bošković Institute, Division of experimental physics in the Laboratory for nuclear physics. In February 2011 Tea started her Ph.D. study in the field of Nuclear Physics at the Faculty of Science, University of Zagreb. Within her doctoral study, she spent 6 months at the University of Padova within the ERASMUS student exchange program.

During her doctoral study Tea actively participated in numerous nuclear physics experiments, most of which utilized magnetic spectrometers. She participated in the experimental campaigns at LNL related to the PRISMA magnetic spectrometers coupled to the CLARA/AGATA gamma array, and to measurement performed with the VAMOS spectrometer coupled to the EXOGAM array at Ganil, France. In addition to those activities, she participated in numerous measurements important for the studies of the reaction mechanisms (electrostatic deflector at LNL), nuclear structure (gamma array of HH National Institute for Physics and Nuclear Engineering, Bucharest, Romania) and reactions important for nucleosynthesis (Zagreb Si array at LNL, and IPNO, Orsay, France).

Tea's main field of research is the study of heavy-ion collisions, in particular multinucleon transfer reactions, deep inelastic collisions, processes of fusion and fission as well as nuclear structure studies of moderately neutron rich nuclei.

Bibliography of published work:

1. Sahin, E.; Doncel, M.; Sieja, K.; de Angelis, G.; Gadea, A.; Quintana, B.; Gorgen, A.; Modamio, V.; Mengoni, D.; Valiente-Dobon, J. J.; John, P. R.; Albers, M.; Bazzacco, D.; Benzoni, G.; Birkenbach, B.; Cederwall, B.; Clement, E.; Curien, D.; Corradi, L.; Desesquelles, P.; Dewald, A.; Didierjean, F.; Duchene, G.; Eberth, J.; Erduran, M. N.; Farnea, E.; Fioretto, E.; de France, G.; Fransen, C.; Gernhauser, R.; Gottardo, A.; Hackstein, M.; Hagen, T.; Hernandez-Prieto, A.; Hess, H.; Huyuk, T.; Jungclaus, A.; Klupp, S.; Korten, W.; Kusoglu, A.; Lenzi, S. M.; Ljungvall, J.; Louchart, C.; Lunardi, S.; Menegazzo, R.; Michelagnoli, C.; Mijatović, Tea; Million, B.; Molini, P.; Montagnoli, G.; Montanari, D.; Moller, O.; Napoli, D. R.; Obertelli, A.; Orlandi, R.; Pollarolo, G.; Pullia, A.; Recchia, F.; Reiter, P.; Rosso, D.; Rother, W.; Salsac, M.-D.; Scarlassara, F.; Schlarb, M.; Siem, S.; Singh, Pushpendra P.; Soderstrom, P.-A.; Stefanini, A. M.; Stezowski, O.; Sulignano, B.; Szilner, S.; Theisen, Ch.; Ur, C. A.; Yalcinkaya, M.
   Shell evolution beyond N=40:69, ^{71,73}*Cu.* Physical Review C 91 (2015) 034302
2. Mijatović, Tea; Szilner, S.; Corradi, L.; Montanari, D.; Courtin, S.; Fioretto, E.; Gadea, A.; Goasduff, A.; Haas, F.; Jelavić Malenica, D.; Montagnoli, G.; Pollarolo, G.; Prepolec, L.; Scarlassara, F.; Soić, N.; Stefanini, A. M.; Tokić, V.; Ur, C. A.; Valiente-Dobon, J. J.
   Pairing correlation study in the ^{40}*Ar+*^{208}*Pb multinucleon transfer reaction* Acta Physica Polonica B 46 (2015)
3. Bourgin, D.; Courtin, S.; Haas, F.; Stefanini, A.M.; Montagnoli, G.; Goasduff, A.; Montanari, D.; Corradi, L.; Fioretto, E.; Huiming, J.; Scarlassara, F.; Rowley, N.; Szilner, S.; Mijatović, Tea.
   Barrier distributions and signatures of transfer channels in the ^{40}*Ca+* ^{58,64}*Ni fusion reactions at energies around and below the Coulomb barrier* Physical Review C 90 (2014) 044610
4. Montagnoli, G.; Stefanini, A.M.; Esbensen, H.; Jiang, C. L.: Corradi, L.; Courtin, S.; Fioretto, E.; Grebosz, J.; Haas, F.; Jia, H. M.; Mazzocco, M.; Michelagnoli, C.; Mijatović, Tea; Montanari, D.; Parascandolo, C.; Scarlassara, F.; Strano, E.; Szilner, S.; Torresi, D.
   Fusion of ^{28}*Si +* ^{28,30}*Si: Different trends at sub-barrier energies* Physical Review C 90 (2014) 044608

5. Grassi, Laura; Forneris, Jacopo; Torresi, D; Acosta, Luis; Di Pietro, Alessia; Figuera, Pierpaolo; Fisichella, Maria; Grilj, Veljko; Jakšić, Milko; Lattuada, Marcello; Mijatović, Tea; Milin, M.; Prepolec, L.; Skukan, N.; Soić, N.; Tokić, V.; Uroić, Milivoj. *Study of the inter-strip gap effects on the response of Double Sided Silicon Strip Detectors using proton micro-beams* NIM A 767 (2014) 99

6. John, P.R.; Modamio, V.; Valiente-Dobon, J.J.; Mengoni, D.; Lunardi, S.; Rodriguez, T.R.; Bazzacco, D.; Gadea, A.; Wheldon, C.; Alexander, T.; de Angelis, G.; Ashwood, N.; Barr, M.; Benzoni, G.; Birkenbach, B.; Bizzeti, P.G.; Bizzeti-Sona, A.M.; Bottoni, S.; Bowry, M.; Bracco, A.; Browne, F.; Bunce, M.; Camera, F.; Cederwall, B.; Corradi, L.; Crespi, F.C.L.; Desesquelles, P.; Eberth, J.; Farnea, E.; Fioretto, E.; Gorgen, A.; Gottardo, A.; Grebosz, J.; Grente, L.; Hess, H.; Jungclaus, A.; Kokalova, Tz.; Korichi, A.; Korten, W.; Kusoglu, A.; Lenzi, S.; Leoni, S.; Ljungvall, J.; Maron, G.; Meczynski, W.; Menegazzo, R.; Michelagnoli, C.; Mijatović, Tea; Million, B.; Molini, P.; Montagnoli, G.; Montanari, D.; Napoli, D.R.; Nolan, P.; Oziol, Ch.; Podolyak, Zs.; Pollarolo, G.; Pullia, A.; Quintana, B.; Recchia, F.; Reiter, P.; Roberts, O.J.; Rosso, D.; Sahin, E.; Salsac, M.-D.; Scarlassara, F.; Sferrazza, M.; Simpson, J.; Soderstrom, P.-A.; Stefanini, A.M.; Stezowski, O.; Szilner, S.; Theisen, Ch.; Ur, C.A.; Walshe, J.

   Shape evolution in the neutron-rich Osmium isotopes: prompt gamma-ray spectroscopy of ^{196}Os Physical Review C 90 (2014) 021301(R)

7. Montanari, D.; Corradi, L.; Szilner, S.; Pollarolo, G.; Fioretto, E.; Montagnoli, G.; Scarlassara, F.; Stefanini, A.M.; Courtin, S.; Goasduff, A.; Haas, F.; Jelavic Malenica, D.; Michelagnoli, C.; Mijatović, Tea; Soić, N.; Ur, C. A.; Varga Pajtler, M.

   Neutron pair transfer in $^{60}Ni+^{116}Sn$ far below the Coulomb barrier Physical Review Letters 113 (2014) 052501

8. Jiang, C. L.; Stefanini, A.M.; Esbensen, H.; Rehm, K.E.; Almaraz-Calderon, S.; Back, B. B.; Corradi, L.; Fioretto, E.; Montagnoli, G.; Scarlassara, F.; Montanari, D.; Courtin, S.; Bourgin, D.; Haas, F.; Goasduff, A.; Szilner, S.; Mijatović, Tea.

   Fusion hindrance for a positive-Q-value system ^{24}Mg + ^{30}Si, Physical Review Letters 113 (2014) 022701

9. Stefanini, A.M.; Montagnoli, G.; Esbensen, H.; Corradi, L.; Courtin, S.; Fioretto,

E.; Goasduff, A.; Grebosz, J.; Haas, F.; Mazzocco, M.; Michelagnoli, C.; Mijatović, Tea; Montanari, D.; Pasqualato, G.; Parascandolo, C.; Scarlassara, F.; Strano, E.; Szilner, S.; Torresi, D.

Fusion of ^{40}Ca + ^{96}Zr revisited: Transfer couplings and hindrance far below the barrier, Physics Letters B, 728 (2014) 639-644

10. Corradi, L.; Szilner, S.; Pollarolo, G.; Montanari, D.; Fioretto, E.; Stefanini, A.M.; Valiente-Dobon, J.J.; Farnea, E.; Michelagnoli, C.; Montagnoli, G.; Scarlassara, F.; Ur, C.A.; Mijatović, Tea; Jelavić Malenica, D.; Soić, N.; Haas, F.

Multinucleon transfer reactions: Present status and perspectives, Nuclear Instruments and Methods in Physics Research, Section B: Beam Interactions with Materials and Atoms 317 (2013) 743-751

11. Modamio, V.; Valiente-Dobon, J.J., Lunardi, S.; Lenzi, S.M.; Gadea, A.; Mengoni, D.; Bazzacco, D.; Algora, A.; Bednarczyk, P.; Benzoni, G.; Birkenbach, B.; Bracco, A.; Bruyneel, B.; Burger, A.; Chavas, J.; Corradi, L.; Crespi, F.C.L.; de Angelis, G.; Desesquelles, P.; de France, G.; Depalo, R.; Dewald, A.; Doncel, M.; Erduran, M.N.; Farnea, E.; Fioretto, E.; Fransen, Ch.; Geibel, K.; Gottardo, A.; Gorgen, A.; Habermann, T.; Hackstein, M.; Hess, H.; Huyuk, T.; John, P.R.; Jolie, J.; Judson, D.; Jungclaus, A.; Karkour, N.; Kempley, R.; Leoni, S.; Melon, B.; Menegazzo, R.; Michelagnoli, C.; Mijatović, Tea; Million, B.; Moller, O.; Montagnoli, G.; Montanari, D.; Nannini, A.; Napoli, D.R.; Podolyak, Zs.; Pollarolo, G.; Pullia, A.; Quintana, B.; Recchia, F.; Reiter, P.; Rosso, D.; Rother, W.; Sahin, E.; Salsac, M.-D.; Scarlassara, F.; Sieja, K.; Soderstrom, P.A.; Stefanini, A.M.; Stezowski, O.; Szilner, S.; Theisen, Ch.; Travers, B.; Ur, C.A.

Lifetime measurements in neutron-rich $^{63,65}Co$ isotopes using the AGATA demonstrator, Physical Review C 88 (2013) 044326

12. Szilner, S.; Corradi, L.; Haas, F.; Pollarolo, G.; Angus, L.; Beghini, S.; Bouhelal, M.; Chapman, R.; Caurier, E.; Courtin, S.; Farnea, E.; Fioretto, E.; Gadea, A.; Goasduff, A.; Jelavić-Malenica, D.; Kumar, V.; Lunardi, S.; Marginean, N.M.; D. Mengoni, D.; Mijatović, Tea; Montagnoli, G.; Recchia, F.; Sahin, E.; Salsac, M.-D.; Scarlassara, F.; Smith, J.F.; Soić, N.; Stefanini, A.M.; Ur, C.A.; Valiente-Dobon, J.J

Structure of chlorine isotopes populated by heavy ion transfer reactions, Physical

Review C 87 (2013) 054322

13. Szilner, S.; Corradi, L.; Pollarolo, G.; Fioretto, E.; Stefanini, A.M.; de Angelis, G.; Valiente-Dobón, J.J.; Farnea, E.; Lunardi, S.; Mengoni, D.; Montagnoli, G.; Montanari, D.; Recchia, F.; Scarlassara, F.; Ur, C.A.; Mijatović, Tea; Jelavić Malenica, D.; Soić, N.; Courtin, S.; Haas, F.; Goasduff, A.; Gadea, A.; Marginean, N.M.; Salsac, M.-D.

    Transfer reaction studies with spectrometers, Acta Physica Polonica B 44 (2013) 417-426.

14. Doncel, M.; Sahin, E.; Gadea, A.; de Angelis, G.; Quintana, B.; Valiente-Dobon, J.J.; Modamio, V.; Albers, M.; Bazzacco, D.; Clement, E.; Corradi, L.; Dewald, A.; Duchene, G.; Erduran, M.N.; Farnea, E.; Fioretto, E.; Fransen, C.; Gernhauser, R.; Gorgen, A.; Gottardo, A.; Hackstein, M.; Hernandez-Prieto, A.; Huyuk, T.; Klupp, S.; Korten, W.; Kusoglu, A.; Lenzi, S.; Louchart, C.; Lunardi, S.; Menegazzo, R.; Mengoni, D.; Michelagnoli, C.; Mijatović, Tea; Montagnoli, G.; Montanari, D.; Möller, O.; Napoli, D.R.; Obertelli, A.; Orlandi, R.; Pollarolo, G.; Recchia, F.; Rother, W.; Salsac, M.-D.; Scarlassara, F.; Schlarb, M.; Stefanini, A.; Sulignano, B.; Szilner, S.; Ur, C.A.

    Lifetime measurements in neutron-rich Cu isotopes, Acta Physica Polonica B 44 (2013) 505-510.

15. Montagnoli, G.; Stefanini, A.M.; Esbensen, H.; Jiang, C.L.; Corradi, L.; Courtin, S.; Fioretto, E.; Goasduff, A.; Grebosz, J.; Haas, F.; Mazzocco, M.; Michelagnoli, C.; Mijatović, Tea; Montanari, D.; Parascandolo, C.; Rehm, K.E.; Scarlassara, F.; Szilner, S.; Tang, X.D.; Ur, C.A.

    Effects of transfer channels on near- and sub-barrier fusion of ^{32}S + ^{48}Ca, Physical Review C 87 (2013) 014611.

16. Montagnoli, G.; Stefanini, A.M.; Jiang, C.L.; Esbensen, H.; Corradi, L.; Courtin, S.; Fioretto, E.; Goasdu, A.; Haas, F.; Ki, A.F.; Michelagnoli, C.; Montanari, D.; Mijatović, Tea; Rehm, K.E.; Silvestri, R.; Singh, Pushpendra P.; Scarlassara, F.; Szilner, S.; Tang, X.D.; Ur, C.A.

    Fusion of ^{40}Ca+^{40}Ca and other Ca+Ca systems near and below the barrier, Physical Review C 85 (2012) 024607.

17. Freer, M.; Ashwood, N.I.; Curtis, N.; Di Pietro, A.; Figuera, P.; Fisichella, M.;

Grassi, L.; Jelavić Malenica, D.; Kokalova, Tz.; Koncul, M.; Mijatović, Tea; Milin, M.; Prepolec, L.; Scuderi, V.; Skukan, N.; Soić, N.; Szilner, S.; Tokić, V.; Torresi, D.; Wheldon, C.

Analysis of states in ^{13}C populated in ^{9}Be + ^{4}He resonant scattering, Physical Review C 84 (2011) 034317.

18. Kempley, R.S.; Podolyák, Zs.; Bazzacco, D.; Gadea, A.; Farnea, E.; Valiente-Dobón, J.J.; Mengoni, D.; Recchia, F.; Sahin, E.; Gottardo, A.; Corradi, L.; Fioretto, E.; Szilner, S.; Anagnostatou, V.; Al-Dahan, N.; De Angelis, G.; Bellato, M.; Berti, B.; Bortolato, D.; Bowry, M.; Bunce, M.; Cocconi, P.; Colombo, A.; Dombrádi, Zs.; Fanin, C.; Gelletly, W.; Isocrate, R.; Ketenci, S.; Kondratyev, N.; Kuti, I.; Mason, P.J.R.; Michelagnoli, C.; Mijatović, Tea; Molini, P.; Montagnioli, G.; Montanari, D.; Nakhostin, M.; Napoli, D.R.; Pellegrini, D.; Regan, P.H.; Rampazzo, G.; Reiter, P.; Rosso, D.; Scarlassara, F.; Stefanini, A.; Singh, P.; Toniolo, N.; Ur, C.A.

Cross-coincidences in the ^{136}Xe+^{208}Pb deep-inelastic reaction, Acta Physica Polonica B 42 (2011) 717-720.